Title	Electron Tunneling Spectroscopic Analysis of Narrow-Gap Semiconductor Antimony Telluride and Semimetal Antimony
Author(s)	Hatta, Eiji; 八田, 英嗣
Degree Grantor	北海道大学
Degree Name	博士(工学)
Dissertation Number	乙第5228号
Issue Date	1997-09-30
DOI	https://doi.org/10.11501/3130622
Doc URL	https://hdl.handle.net/2115/51454
Type	doctoral thesis
File Information	000000315812.pdf

ELECTRON TUNNELING SPECTROSCOPIC ANALYSIS OF NARROW-GAP SEMICONDUCTOR ANTIMONY TELLURIDE AND SEMIMETAL ANTIMONY

Eiji Hatta

①

ELECTRON TUNNELING SPECTROSCOPIC ANALYSIS OF NARROW-GAP SEMICONDUCTOR ANTIMONY TELLURIDE AND SEMIMETAL ANTIMONY

by

Eiji Hatta

A dissertation submitted in partial fulfillment
of the requirements for the degree of Doctor
(Engineering)

Hokkaido University

1997

To my wife
and
To my parents

Dasjenige, wogegen ich mich wehre, ist der Begriff einer idealen Exaktheit, der uns sozusagen a priori gegeben wäre. Zu verschiedenen Zeiten sind unsere Ideale der Exaktheit verschiedenen; und *keines ist das höchste.*

L. W. Wittegenstein

ABSTRACT

In this work tunneling studies on an antimony telluride, V-VI narrow-gap semiconductor (NGS), and an antimony, an element of the compound semiconductor, are described and discussed.

Tunnel junctions of the types Au-Sb_2Te_3-Al and Al-Al oxide-Sb were prepared. A clean surface, an important condition for tunneling experiments, was produced by the layer-by-layer deposition in a high vacuum ($< 5\times10^{-7}$ Torr) without breaking the vacuum. Sb_2Te_3 films were prepared by the flash evaporation of antimony telluride pellets.

A rejection-selection filter network suitable for the detailed study of the first and second derivatives of the current-voltage characteristics of tunnel junctions was constructed. The uniqueness of the network lies in its low noise and in its applicability for wide range of resistance of the tunnel junctions (1 Ω – 10 kΩ). The filter network tunneling spectrometer is described in detail .

A narrow width conductance peak at zero bias voltage with a symmetric undershoot structure is found in Au-Sb_2Te_3-Al tunnel junctions. Except for the voltage symmetric undershoot structure, this behavior is found to be well described by a tunnel equation where a nonparabolic $E-k$ dispersion relation of Kane's type is involved. In this model, analytic continuation of the $E-k$ relation from the conduction- and valence bands at the middle of the energy gap is successfully carried out if the both band edge effective masses are the same. From this analysis, it is shown that the Fermi level locates just above the valence band edge in this material. The origin for undershoot structure is discussed. It is particularly emphasized that this analysis is essential for tunneling through a narrow-gap semiconductor whose Fermi level locates near the valence band edge. It is also noted that the two-band analysis must be necessarily carried out for tunneling through *a solid barrier with conduction- and valence bands.*

Electron tunneling experiments have been carried out to investigate the confirmed anisotropy of Fermi surfaces and phonons in a semimetal antimony. Depending upon the texturization of antimony films, the definite change in shape of tunneling conductance is observed. In addition to the intervalley acoustic and optical phonon peaks, the intravalley acoustic phonon peak becomes observed in the second derivative curve dependent upon the exposed crystal faces. This intravalley acoustic phonon peak has never been observed in Raman spectra and neutron scattering experiments. As for the intervalley acoustic and optical phonon peaks, the half-width of these peaks becomes decreased as the change of the exposed crystal faces. This is the first observation of the anisotropy of Fermi

surfaces and phonons in tunneling spectroscopy. Moreover this is the first observation of the intravalley acoustic phonon peak in tunneling spectroscopy. The overtone phonon peak exhibits an asymmetric structure in contrast to that of the Raman spectrum. This might be due to the difference of coupling functions.

Electron tunneling measurements have been performed to study the one-particle density of states in inhomogeneous Sb films. A conductance minimum is observed at zero bias and the result can be well described in terms of the theory of electron-electron interaction in weakly disordered metals. On the other hand, at higher voltages the background conductance curve exhibits roughly an asymmetric parabola, as is typical in a metal-insulator-metal (and not semimetal) tunnel junction. The feature of band structure in the semimetal disappears completely. This result indicates that an inhomogeneous Sb film constitutes a metallic, degenerate electron gas system at the interface of the junction. A metastable metallic phase of Sb may be stabilized due to a higher disorder. This is the first evidence of the disorder induced semimetal-metal transition.

ZUSAMMENFASSUNG

In dieser Arbeit werden Tunnelexperimente an dem schmallückigen Halbleiter (SLH) Sb_2Te_3, einem V-VI-Verbindungshalbleiter mit rhomboedrischer Struktur und an dem Halbmetall Antimon beschrieben und diskutiert.

Es wurden Tunneldioden, mit dem Aufbau Au-Sb_2Te_3-Al und Al-Al Oxid-Sb hergestellt. Die Energielücke von Sb_2Te_3 und Al Oxid bilden dabei die Tunnelbarriere. Die für Tunnelexperimente wichtige saubere Oberfläche wurde mit einer beweglichen Maske und durch sukzessive Aufdampfung unter Hochvakuum erreicht.

Zur Messung der ersten und der zweiten Ableitung der Strom-Spannungscharakteristiken der Tunneldioden wurde ein Filternetzwerk entwickelt, das besonders geringes Rauschen aufweist und für einen großen Widerstandsbereich der Tunneldioden geeignet ist. Dieses Netzwerk wird eingehend beschrieben.

Für den Fall, daß die Energielücke des Halbleiters die Barrier bildet, zeigt die dI/dV-Charakteristik bei Spannungsnullpunkt ein schmales positives Maximum und scharfe negative Minima zu beiden Seiten des Maximums. Die Struktur ist völlig symmetrisch um den Spannungsnullpunkt. Unter Ausnahme der Leitfähigkeitsminima, konnte der Verlauf durch eine Tunnelgleichung, in der eine nichtparabolische $E-k$-Dispersionsbeziehung berücksichtigt ist, gut erklärt werden. Es wird gezeigt, daß die Berücksichtung der $E-k$-Dispersionsbeziehung für die Analyse des Tunnels durch den SLH, wo die Fermi-Energie in der Nähe von der Valenzband-Kante liegt, wesentlich ist. Dies scheint typisch für das Tunneln durch einen Festkörper. Auch die Ursache für die symmetrischen Leitfähigkeitsminima wird diskutiert.

Tunnelexperimente an dem Halbmetall Sb bei Tunneldioden vom Typ Al-Al Oxid-Sb wurden zur Untersuchung der Anisotropie der Elektronen und Phononenstruktur durchgeführt. In dieser Arbeit wurden erstmals akustische Phononen in Intrabandprozessen durch Tunnelspektroskopie beobachtet. Sowohl die akustischen Phononen in Intrabandprozessen als auch die akustischen und optischen Phononen in Interbandprozessen werden abhängig von der Kristallorientierung beobachtet. Eine systematische Änderung der Tunnelleitfähigkeit wird beobachtet. Eine Anisotropie der Elektronen- und Phononenstruktur ist in dieser Arbeit erstmals durch Tunnelspektroskopie beobachtet worden.

Es wurden Tunnelexperimente zur Bestimmung der elektronischen Zustandsdichte ungeordneter Sb Filme durchgeführt. Die Tunnelleitfähigkeit hat ein Minimum bei 0 meV und die Meßkurve läst sich gut mit der Altshuler-Aronov Theorie erklären. Unter höheren Diodenspannungen zeigt die gemessene Tunnelcharakteristik einen für Metall-Isolator-Metall Tunneldioden typischen Verlauf. Die gefundene Bandstruktur stimmt nicht ganz mit der eines Halbmetalles überein. Das Ergebnis zeigt, daß sich an der Grenzfläche Al-Oxid/Sb Film ein entartetes Elektronengas bildet. Eine metastabile Modifikation des Sb mag durch höhere kristallographische Unordnung stabilisiert werden. Ein durch kristallographische Unordnung verursachter Halbmetall-Metall Übergang wurde in dieser Arbeit zum erstenmal beobachtet.

Contents

1 Introduction

> Wie schwer fällt mir zu sehen, *was vor meinen Augen liegt!*
>
> L. W. Wittegenstein.

Historically, the concept of tunneling is almost as old as quantum mechanics but the *first* conclusive experimental evidence of tunneling through a junction was seen in Ge. This important event occurred in 1957 when Esaki invented the tunnel diode. He established the reproducibility of tunnel structures, and demonstrated that tunneling could be used for extraction of spectroscopic information, such as electronic structures and elementary excitations of solids. In 1960, Giaever discovered tunneling into superconductors and *directly* observed superconducting energy gap and quasiparticle density of states. He demonstrated the simplicity and elegance of tunneling spectroscopy and gave conclusive experimental evidence of tunneling mechanism in tunnel structures. Giaever's discovery led to the prediction and the subsequent observation of the Josephson effect. Josephson's discovery established the physical significance of the concept of gauge invariance.

As for the tunneling effect in condensed matter physics, its study covers a very wide range. They are typically: identifications of conduction and valence band edges, band gap and impurity levels (or bands), negative resistance effect, surface quantization, Landau levels, self-energy (polaron) effects in semiconductors[1, 2], spin polarization in magnetic materials[3], energy gaps and Eliashberg functions $\alpha^2F(\omega)$[4]-[16] in superconductors, molecular vibration peaks[17]-[23], resonant tunneling[24], spin-flip (Zeeman) transitions of paramagnetic ions[25, 26], Kondo scattering[27], elementary excitations such as phonons, magnons, plasmons[28, 29, 30] and excitons[31]-[34], quantum size effect[35, 36, 37], charging effects (single electron tunneling)[38]-[43], electron-electron interactions and localization[44, 46], electronic density of states for quasi-one-dimensional conductors (CDW and SDW gaps)[47]-[50], quasiparticle gap in Kondo semiconductors[52, 54], energy gaps in intermediate-valence materials[55, 56], 2D-2D tunneling[57], fluctuation kinetics of single electron trap states in the barrier material[58, 59], etc..

In principle, a tunneling experiment is extremely simple. It involves making the tunnel junction, which consists of two conducting electrodes separated by a thin insulating layer, and measuring the electrical current I through the junction as a function of the voltage V applied to the electrodes. Such $I-V$ characteristics contain information about the electronic properties of the electrodes as well as the barrier at energies eV above and below the Fermi energy of the electrodes. In other words, tunneling is a special form of ultra-low energy electron spectroscopy in solids; the $I-V$, $\mathrm{d}I/\mathrm{d}V$-V, or $\mathrm{d}^2I/\mathrm{d}V^2$-$V$ characteristics are the electron spectra plotted as a function of the injection energy eV of the electron. Tunneling spectroscopy has proved to be a sensitive and powerful technique for the extraction of spectroscopic information (i.e., electronic structures and elementary excitation spectra in solids) in condensed matter physics. In fact, for example, for the superconductor research, it played a decisive role in the past for the establishment of the BCS electron-phonon coupling theory.

This study* discusses two fundamental aspects of elastic and inelastic electron tunneling and electron density of states anomalies in random solid mixtures studied by tunneling experiments.

First, tunneling experiments on Au-Sb_2Te_3-Al tunnel junctions are carried out to investigate the significance of the dispersion relation in the tunneling barrier in analyzing the tunneling characteristics and further to obtain information about the dispersion relation of the Sb_2Te_3, which has not been clear at present. This consideration would be of quite significance because the energy gap between the conduction- and valence bands constitutes the tunneling barrier in tunneling through *a solid.* This material has been known to be always p-type regardless of various attempts to produce n-type materials; however, the location of the Fermi level remains unclear. This investigation would be therefore also significant to identify the *singular* position at which the Fermi level of this material locates.

Second, an electron tunneling study on thin films of semimetal antimony is performed to investigate an anisotropy of Fermi surfaces and phonons in tunneling spectroscopy. Such anisotropy has been expected to be observed in tunneling spectroscopy, however, surprisingly, it has never been observed before. If such anisotropy can be observed in tunneling spectroscopy, it will be used more widely in the future. Antimony is a good material for this study since the crystal structure is rhombohedral and the Brillouin zone is distorted. Therefore there exists anisotropic band and phonon structure in this material. Moreover, this material has both covalent and metallic characters and the different crystal faces are expected to be exposed on a junction interface, dependent upon the preparation conditions.

Last, electron tunneling experiments in inhomogeneous Sb films (i.e., semimetal-semiconductor two-phase systems) are described. There has been few studied on the correlation between the electron-electron interaction in disordered semimetals (minor and two carrier, multi-valley systems) and the band structures. The density of states anoma-

---

*This thesis is based upon the following papers.

E. Hatta, J. Nagao, and K. Mukasa, Z. Phys. B **98**, 33(1995).

E. Hatta, T. Gohda, K. Mukasa, and T. Ishii, Vacuum. **46**, 1377(1995).

E. Hatta, J. Nagao, and K. Mukasa, J. Appl. Phys. **79**, 1511(1996).

E. Hatta and K. Mukasa, Solid State Commun. **98**, 293(1996).

E. Hatta and K. Mukasa, Solid State Commun. **103**, 235 (1997).

lies at the Fermi energy have been widely studied in amorphous and disordered metals; however, there has been few studied on those in disordered semimetals, especially, the correlation between the electron-electron interactions and the band structure. This investigation is of quite interest from the point of view of the electron correlation in small carrier system.

2 Basic Concepts

Ich glaube, es ist eine wichtige und merkwürtige Tatsache, daß ein musikalisches Thema, wenn es in (sehr) verschiedenen Tempi gespielt wird, seinen *Charakter* ändert. *Übergang von der Quantität zur Qualität.*

L. W. Wittegenstein.

2.1 Basic Concepts of Electron Tunneling Spectroscopy

2.1.1 Attenuation Constant $\kappa(E)$ and Electron Dispersion Relation $E(k)$ in Electron Tunneling

We take the stationary state approach to elastic electron tunneling[1, 28]. We assume a planar junction and let the one-dimensional tunnel barrier extend in the x direction, as illustrated in Fig. 1 (a). The transverse electron wave vectors, k_y and k_z are constants of motion. For elastic tunneling, the energy E as well as k_y and k_z of the tunneling electron is conserved. We focus our attention on electrode 1, which is negatively biased with a voltage V relative to electrode 2. The electron tunneling current per area A flowing from 1 to 2 at temperature $T = 0$ is given by

$$J = \frac{I}{A} = \frac{2e}{(2\pi)^3} \int v_x D d^3k, \tag{1}$$

where the integration is over all the allowed states in electrode 1. D is the tunneling probability, which depends in general on k_y, k_z, and E of the tunneling electron, and on V (which distorts the tunneling barrier); v_x is the electron velocity in the tunneling direction, which specifies how frequency it approaches the barrier. By using

$$v_x = \frac{1}{\hbar}\frac{\partial E}{\partial k_x} \tag{2}$$

we can rewrite

$$J = \frac{2e}{(2\pi)^3 \hbar} \int_{\mu_1 - eV}^{\mu_1} dE \int D dk_y dk_z, \tag{3}$$

where μ_1 is the Fermi energy in electrode 1. Equation (3) can be generalized to finite T by including the Fermi function, $f(E) = [1 + \exp\{(E-\mu)/kT)\}]^{-1}$ to describe the

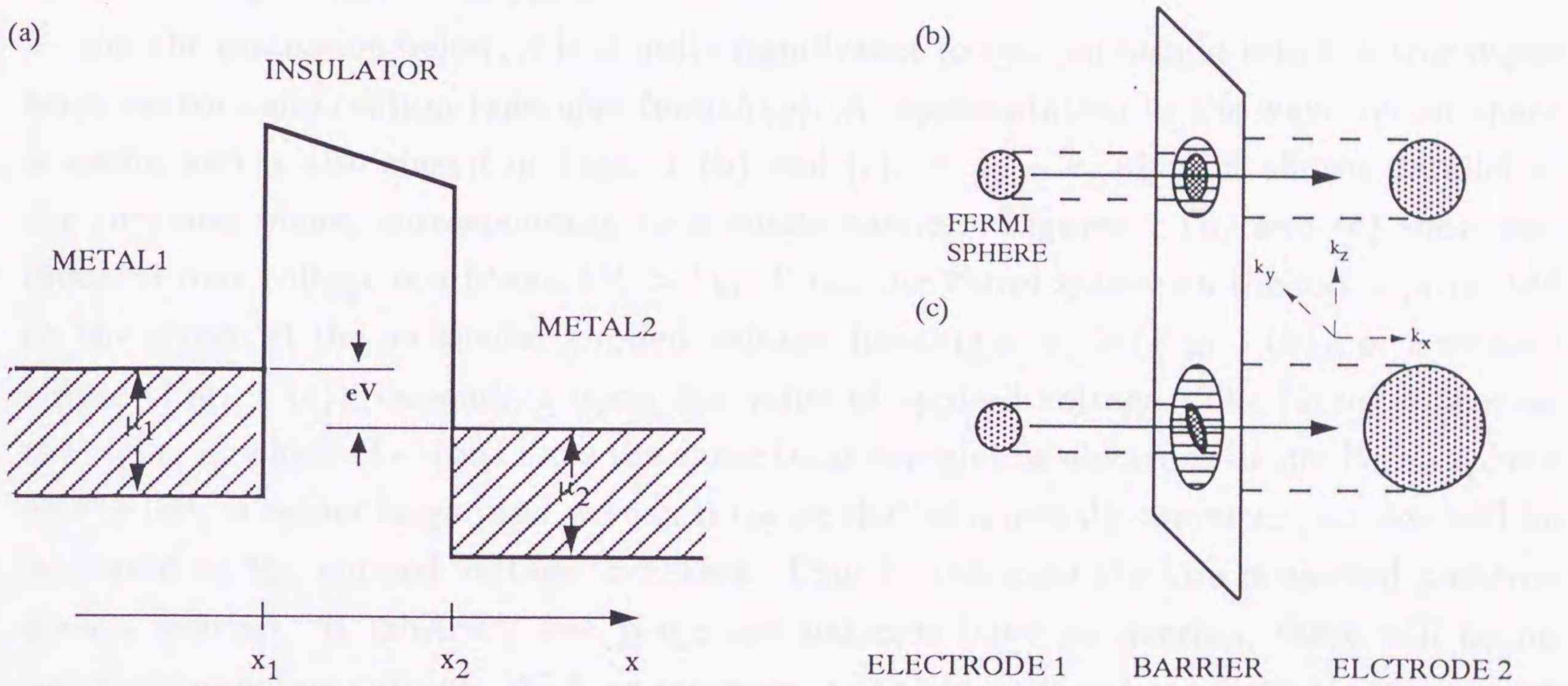

Figure 1: (a) A model tunnel junction and (b), (c) construction of shadows of energy surfaces on a $k_y - k_z$ plane corresponding to a single barrier ($V_b < V_c$).

occupation of states in electrode 1 and the vacancy of states in electrode 2. The resulting expression is

$$J = \frac{e}{2\pi^2 h}\int_{-\infty}^{\infty} dE\,[f(E) - f(E + eV)] \int D dk_y dk_z, \tag{4}$$

i.e., the current between constant-energy shells on the two sides of the barrier is proportional to the difference in the probability of occupation of the states in the two shells and to a surface integral over the overlap of their shadows where we define the "shadow" of a constant-energy surface to be its projection in wave-number space on a plane parallel to the barrier. In practice, however, tunneling experiments are usually carried out at liquid helium temperatures ($T \leq 4.2$ K) to eliminate thermionic emission over the barrier, so the $T = 0$ expression is adequate.

For the discussion below, it is of quite significance to gain an insight into this transverse wave-vector conservation (*specular tunneling*). A representation in the wave vector space is useful and is also shown in Figs. 1 (b) and (c). A $k_y - k_z$ plane is shown parallel to the junction plane, corresponding to a single barrier. Figures 1 (b) and (c) show two different bias voltage conditions ($V_c > V_b$). First, the Fermi sphere on the left is projected on the screen at the particular applied voltage, forming a circle (Fig. 1 (b)), or a smaller ellipse (Fig. 1 (c)), depending upon the value of applied voltage. The Fermi sphere on the right, in which electrons have the same total energies as electrons in the Fermi sphere on the left, is rather large (and we can imagine that of a metal); moreover, its size will be increased as the applied voltage increases. Thus in this case the two projected patterns always overlap. If arbitrary two projected patterns have no overlap, there will be no specular tunneling current. With an increase in applied voltage from V_b to V_c, the current will decrease because of disappearance of overlapping regions, thereby causing a negative resistance.

We notice that *J does not depend explicitly on the electron density of states ($\rho = (L/\pi)(\partial E/\partial k_x)^{-1} = L\hbar v_x/\pi$) in the x direction by v_x, and that it depends only on the density of states associated with k_y and k_z.* This is a direct consequence of an independent particle model and the resultant reciprocal relation between the particle velocity and the density of states. The tunneling conductance, defined $G \equiv \mathrm{d}I/\mathrm{d}V$, is

$$G = \frac{e^2 A}{2\pi^2 h}\left[\int D dk_y dk_z + \int dE \int \frac{\partial D}{\partial (eV)} dk_y dk_z\right]. \tag{5}$$

Here, the first term, which may be regarded as a density of states term (, which is the subject in Sec. 4.3), arises from the change in the number of states available for tunneling due to the incremental change of V. The second term arises from the change in D (, which is the subject in Sec. 4.1). Usually, the second term dominates and the $G - V$ curve reflects qualitatively the tunneling barrier and its dependence on V.

The tunneling probability D is the ratio of the transmitted current to the incident current. It is obtained by solving the time independent Schrödinger equation in the allowed and the forbidden regions of the tunnel junction. The solution $\Psi(x)$ is composed of an incident wave and a reflected wave on one side of the barrier and of a transmitted wave on the other side. These waves are matched to the exponentially decaying solution inside the barrier by using the boundary condition that $\Psi(x)$ and $(1/m^*)\mathrm{d}\Psi(x)/\mathrm{d}x$ are continuous at the classical turning points (x_1 and x_2 in Fig. 1 (a)). For a square barrier, the exact solution gives

$$D = \frac{16 k_1 k_2 K}{(k_1^2 + K^2)(k_2^2 + K^2)} e^{-2Kt}, \tag{6}$$

where k_1 and k_2 are the electron wave vectors on opposite sides of the tunneling barrier of thickness t, and K is the decay constant in the barrier. For a more general barrier, $V(x)$, application of the semiclassical WKB approximation gives

$$D = \exp\left(-2\int K dx\right), \tag{7}$$

where the integration is between the two classical turning points. The WKB approximation is valid for slowly varying potentials. If it is applied outside the range of its validity, e.g., to the square barrier, it still gives the correct component but not the prefactor, as seen by comparing (7) to (6). In typical problems of interest, the exponential term, approximately 10^{-5} to 10^{-12} (e.g. $\sim 10^{-9}$ for a barrier of 1 eV height and 20 Å thickness), dominates. The relatively weak energy dependence in the prefactor in (6), for example, becomes important only in the limit of small E, corresponding to the tunneling of electrons close to a band edge in the electrode. It has been seen from the above discussion that *tunneling does not measure directly the normal state electron density of states of the electrodes.* However, the tunneling current depends on the number of states available and on their tunneling probability through its barrier. The band structure of the semiconductor can, therefore, in various ways be reflected in the tunneling characteristics, $I - V$, $\mathrm{d}I/\mathrm{d}V - V$ or $\mathrm{d}^2I/\mathrm{d}V^2 - V$ of the junction.

In *real solids*, the tunneling barrier is the forbidden energy gap, E_g, separating the conduction band from the valence band of the insulator (or semiconductor) through which the electron tunnels. The energy dependence of the decay constant K in (6) and (7) is described by the electron dispersion relation of the material as is illustrated in Fig. 2, where E is plotted as a function of k^2. *This suggests that the tunneling equation governing elastic tunneling can be used as a basis to subtract the information about the electron energy (E) - momentum (k) dispersion relation in the forbidden energy region of insulating and semiconducting barriers from elastic tunneling data.*

For energies in the conduction band ($E > E_c$), or valence band ($E < E_v$), k^2 is positive, k is real, and the wave functions describe propagating states. However, for $E_v < E < E_c$,

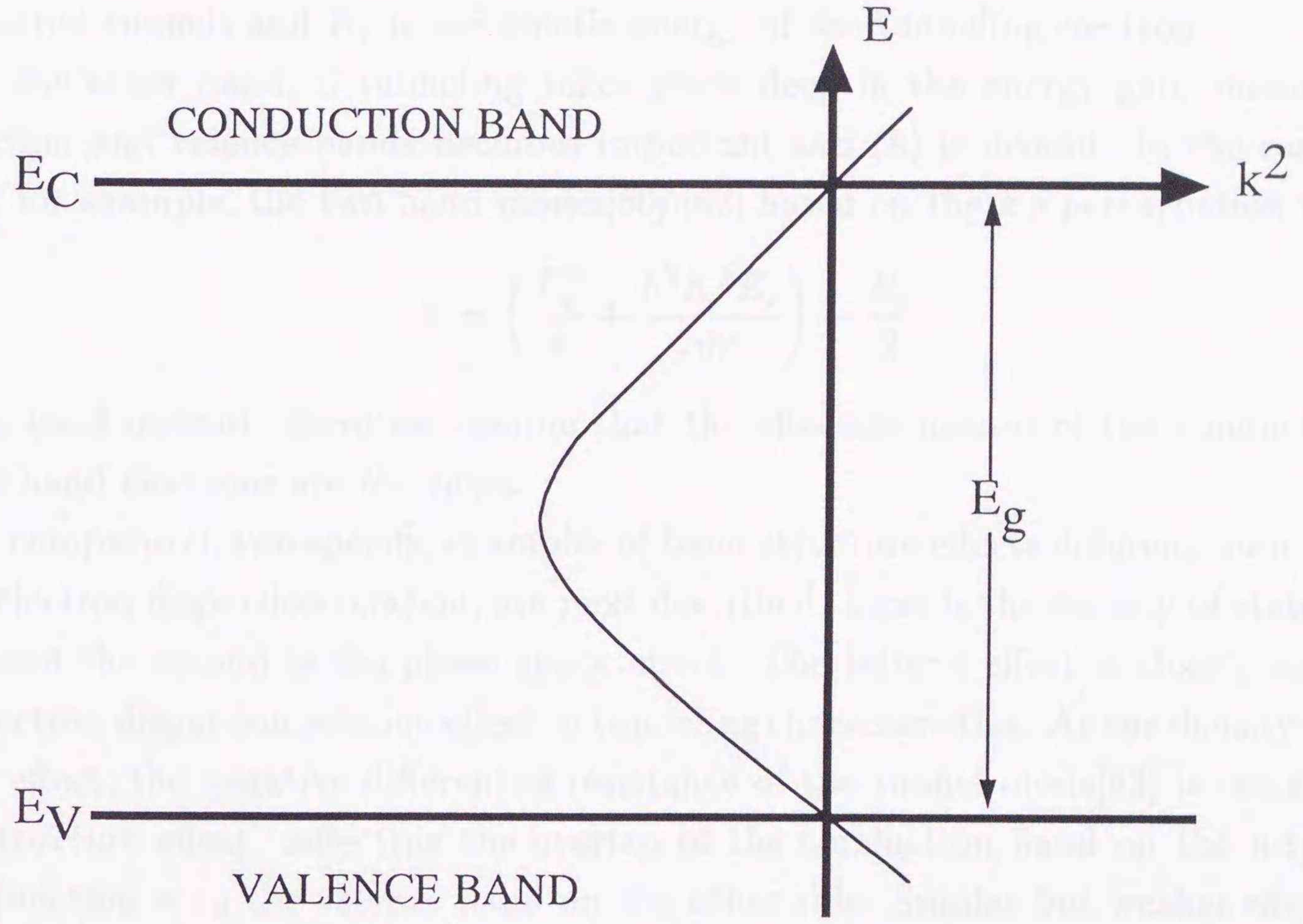

Figure 2: E versus k^2 in an insulator or a semiconductor.

k^2 is negative, k is imaginary, and the wave function decays exponentially with the decay constant given by $k = iK$. Close to the band edges, E_c and E_v, the band is approximately parabolic: $= \hbar^2 k^2 / 2m^*$, where m^* is the effective mass of the electron or the hole. Thus, if tunneling takes place close to the conduction or valence band edges, K in (6) and (7) can be approximated by

$$K = \left\{ \left(2m^* / \hbar^2 \right) \left[V(x) - E_x \right] \right\}^{1/2}, \tag{8}$$

where the barrier $V(x)$ is the conduction or valence band of the material through which the electron tunnels and E_x is the kinetic energy of the tunneling electron.

On the other hand, if tunneling takes place deep in the energy gap, *mixing* of the conduction and valence bands becomes important and (8) is invalid. In the case of p-n diodes, for example, the two band model[60]-[62] based on the $k{\cdot}p$ perturbation theory

$$E = \left(\frac{E_g^2}{4} + \frac{\hbar^2 K^2 E_g}{2m^*} \right) - \frac{E_g}{2} \tag{9}$$

is often used instead. Here we assume that the effective masses of the conduction and valence band electrons are *the same*.

For comparison, two specific examples of band structure effects different from that due to the electron dispersion relation, are next described. First is the density of states factor effect, and the second is the phase space effect. The latter's effect is closely associated with electron dispersion relation effect in tunneling characteristics. As the density of states factors effect, the negative differential resistance of the tunnel diode[63] is the strongest band structure effect, reflecting the overlap of the conduction band on the n-type side of the junction with the valence band on the other side. Similar but weaker effects have been observed in *oxide junctions* made of highly degenerate p-type ($\sim 10^{20}$ cm^{-3}) SnTe and GeTe films on Al-Al_2O_3 base electrode[64]. As in the tunnel diode, the initial current increase with increasing negative bias is due to the increase in the number of states in the semiconductor, into which electrons in the metal electrode can tunnel. However, unlike the tunnel diode, this number remains constant for $\mu_p + E_g \geq eV \geq \mu_p$, while their tunneling probability decreases with increasing V, because of the increase in the height of their tunnel barrier. Thus a negative differential resistance results in the $I - V$ characteristic. The observation of this effect depends much on the details of the potential at the oxide-semiconductor interface. For example, if a depletion region exists in the semiconductor, as is the usual case, its width will decrease continuously with increasing V, even for $V \geq \mu_p / e$, and it will make the observation of these effect difficult.

As the phase space effect, the onset of tunneling into a new band can give rise to a threshold effect. Such an effect was first observed in MS contacts on n-type Ge[65, 66]. In Ge, the conduction band minimum Γ'_2 at the center of the Brillouin zone is 145 meV above the L_1 minima. Since the resistance peak in this case measures the Fermi energy in the L_1 minima the difference in the bias of the peak and the bias of the threshold gives a direct measure of the energy: $\Gamma_2' - L_1$. The observation of this effect in Ge is facilitated by the fact that the effective mass $m_\Gamma^* < m_L^*$ and, consequently, tunneling is easier for the Γ_2' band. This point is more clearly demonstrated by the pressure dependence of the zero-bias resistance $R(0)$ of a MS contact on n-type GaSb[67] with $n = 3.5 \times 10^{18}$ cm^{-3}. In GaSb, the conduction band minima at Γ lies below (by $\sim$ 85 meV) the L minima and only a small fraction of the electrons occupies L. Tunneling at zero-bias is dominated by the Γ band which also has a smaller effective mass. The application of a hydrostatic pressure P reduces the energy separation between the minima and transfers electrons from Γ to L. Since the tunneling probability is smaller for electrons in L than in Γ, $R(0)$ increases. It shows a sudden increase at $P \sim 12$ kbar and then saturates when all the electrons are transferred into the L minima.

2.1.2 Electron Density of States Anomalies in Disordered Materials Studied by Electron Tunneling

Most of our understanding in solid state physics has been based on the periodicity of lattice. Although there are many materials which do not have such a symmetry, little has been understood because of difficulties to handle them theoretically. The phenomenon of localization of electron wave functions in random potential was first treated by Anderson[68] in 1958. He showed that the three dimensional diffusion of electrons in macroscopic distance is impossible when the randomness is large enough, even though the energy spectrum is continuous across the Fermi level. The localization is a consequence of the interference of electron waves which are scattered by the random potential. As for the interaction effects, the electrons in random potential are less effective for the shielding of the Coulomb interaction than those in pure metal because their motion is diffusive and cannot follow the change in the electric field immediately. Therefore the Coulomb interaction between electrons are enhanced. This enhanced interaction causes an additional anomaly in the density of states at the Fermi level. Through the Einstein relation $\sigma = e^2 D N(E_F)$ where D is the diffusion constant, and N is the density of states, there appears an anomaly in the conductivity.

Before starting the discussion about the electron correlation in solids, we first mention *classes of insulators*, which are significant for understanding the underlying physics in disordered materials. The restriction to zero temperature and small external fields allows us to identify two basic categories of insulators, namely,

- insulators due to the electron-ion interaction
- insulators due to the electron-electron interaction

To understand the insulating behavior of a material at zero temperature we may consider only static ion configurations. Then, the first category subsumes all insulators, which can be understood in terms of a *single-electron* theory. The following three classes of insulators are prominent representatives:

1. *Bloch-Wilson or band insulators* due to the electrons' interaction with the periodic potential of the ions;
2. *Peierls insulators* due to the electrons' interaction with static lattice deformations;
3. *Anderson insulators* due to the presence of disorder, e. g., the electrons' interaction with impurities and other lattice imperfections.
4. *Mott insulators* due to the electron-electron interaction

Mott insulators are conceptually different. Here, we always have to solve a *many-electron* problem. In real materials, the interactions used in the above classification scheme are always simultaneously present such that the classification of experimentally observed insulators is not always that straightforward. In fact, an observed metal-insulator transition need not be dominated by one interaction alone to the exclusion of the others. Although a single interaction may drive the transition, its nature may be (and often is) strongly affected by the others. An example for this effect is modifications of the disorder-induced metal-Anderson insulator transition by the Coulomb interaction between electrons. Hence, this metal-insulator transition is called *Anderson-Mott* transitions.

On the other hand, electronic properties of weakly disordered metals at low temperatures are governed by the effects of electron-electron interaction[69, 70, 71, 72] and weak localization[73]. In particular, the electron-electron interaction leads to a correction of the one-particle density of states (DOS) at the Fermi energy which was first predicted by Altshuler and Aronov[69, 70]. The form of $N(E)$ is illustrated in Fig. 3 (a). This correction was confirmed experimentally by tunneling experiments[74]-[83]. The physics of *strongly disordered systems* near the metal-insulator transition is not understood fully and is still a new world. However, tunneling experiments show that the DOS vanishes at the metal-insulator transition[44, 84, 85, 86]. This is in agreement with theories of the metal-insulator transition which take into the electron-electron interaction[87, 88, 89].

First, we consider Bergmann's treatment as for weak localization. It was first pointed out by Bergmann[90, 91] that multiple scattering could produce a drop in the conductivity. The argument is illustrated in Fig. 3 (b), which shows the Fermi surface of a metal in

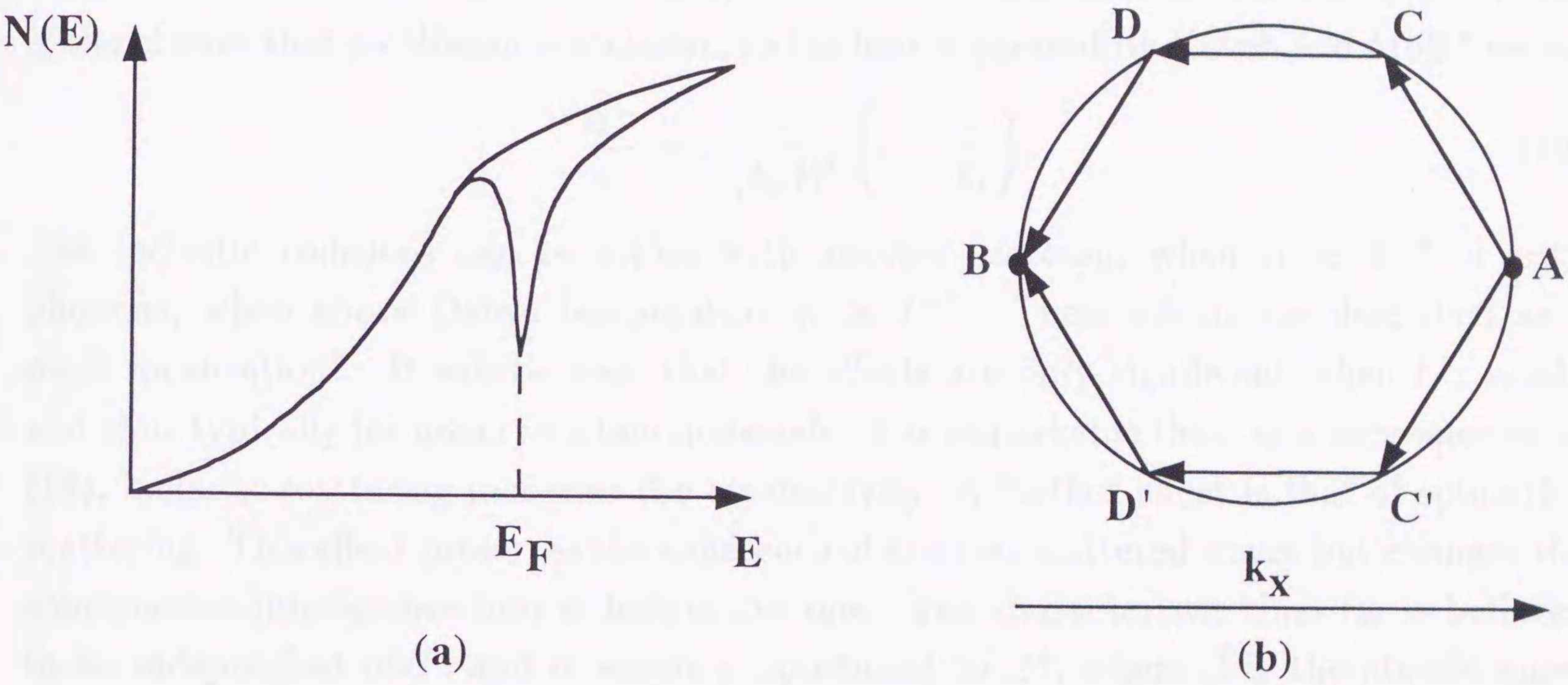

Figure 3: (a) Density of states in a disordered material, showing the change near the Fermi energy E_F predicted by Altshuler and Aronov. (b) Fermi surface in k-space, showing multiple scattering paths leading to quantum interference.

k-space, with an electric field along the k_x axis. An electron in a state represented by A, moving in the direction of the field, can be scattered through 180° to the point B, moving opposite direction, either directly or by multiple scattering events such as ACDB. In the latter case two paths, ACDB and AC'D'B' are possible, and, if all scattering processes are elastic, these paths can interfere. Bergmann shows that this process reduces the conductivity by

$$\frac{\Delta\sigma}{\sigma} = -\frac{1}{(k_F l)^2}. \tag{10}$$

If some collisions are inelastic, this interference does not take place. We therefore introduce the inelastic diffusion length

$$L_i = (D\tau_i)^2, \tag{11}$$

where D is the diffusion constant and τ_i the time between inelastic collisions. Then l/L_i is the chance that a collision is inelastic, so (as first suggested by Kaveh and Mott) we set

$$\frac{\Delta\sigma}{\sigma} = -\frac{1}{(k_F l)^2}\left(1 - \frac{l}{L_i}\right). \tag{12}$$

The inelastic collisions can be either with another electron, when $\tau_i \propto T^{-2}$ or with phonons, when above Debye temperature $\tau_i \propto T^{-1}$. These effects are described as " weak localization". It will be seen that the effects are only significant when l is small, and thus typically for noncrystalline materials. It is remarkable that, as a consequence of (12), inelastic scattering increases the conductivity. A further effect is that of spin-orbit scattering. This effect preserves the coherence of the two scattered waves but changes the constructive interference into a destructive one. The characteristic time τ_{so} is believed to be independent of T, and inversely proportional to Z^4, where Z is the atomic number. The concept of the inelastic diffusion length is of major importance in discussions of quantum interference.

Altshuler and Aronov investigated the influence of disorder on the long-range electron-electron interaction in weakly disordered metals. The surprising result was that a correction of the density of states $\delta N(E)$ occurs around the Fermi energy[69]-[72]. This correction for three dimensional metals with respect to the electron-electron interaction is given by the following equation (T=0 K) [69]

$$\frac{\delta N(E)}{N_{03}} = \frac{\lambda_3}{4\sqrt{2}\pi^2(\hbar D)^{3/2}N_{03}}\sqrt{|E|}, \tag{13}$$

where λ_3 is the electron-electron interaction constant ($\lambda_3 \simeq 1$), D is the diffusion constant, and N_{03} is the DOS at the Fermi energy. The theory is valid for $\delta N(E)/N_{03} < 1$.

The correction for two-dimensional metals[70, 71] has the following form ($T = 0$ K)

$$\frac{\delta N(E)}{N_{02}} = \frac{\lambda_2}{4\pi^2\hbar D N_{03} t}\ln\frac{|E|\tau_0}{\hbar}, \tag{14}$$

where λ_2 is the electron-electron interaction constant, τ_0 is the momentum relaxation time, and t is the thickness of the disordered film. The constant λ_2 is given[71] by $\lambda_2 = \ln(2\Delta\kappa_2)$, where Δ is the thickness of the tunneling barrier and κ_2 is the two-dimensional inverse screening length $\kappa_2 = \kappa_3^2 t/2$ $\left(\kappa_3 = \sqrt{e^2 N_{03}/\epsilon_0}\right)$. The expression for λ_2 was derived taken into account that the DOS of the film is measured by tunneling experiments. Because of the reference electrode the interaction between the electrons is of dipole nature[71]. For film thickness $t < \Delta$ the constant λ_2 is proportional to the logarithm of energy. In this case the correction $\delta N(E)$ has a double logarithmic form.

The critical length $L_E = \sqrt{\hbar D/E}$ determines the dimension of a film according to the electron-electron interaction. Thus, for a given thickness t of the film a dimensional crossover occurs as a function of the energy of the electrons. For low energies the $N(E)$ behavior is logarithmic ($L_E > t$), and for higher voltages the $N(E)$ behavior is square-root ($L_E < t$). The critical energy[80] which separates the logarithmic and square-root conductance behavior of the DOS is given by $E_c = 4\pi^2\hbar D/t^2$.

The tunneling conductance is an useful tool to investigate the density of states in the vicinity of the Fermi energy. Assuming a constant DOS of the reference electrode and a constant tunneling probability, the tunneling conductance $\sigma(V)$ is directly related to the density of states $N(E)$ of the disordered electrode: $\sigma(V)/\sigma_0 = N(E)/N_0$, where σ_0 is the tunneling conductance at $V = 0$ and N_0 is the DOS at the Fermi energy[93].

2.1.3 Electron Tunneling and Electron-Phonon Coupling Function $\alpha^2 F(\omega)$

Tunneling offers a unique spectroscopic probe of interactions between electrons and elementary excitations[94] such as phonons, plasmons, and magnons, etc., in solids. This section discusses tunneling technique to probe electron-phonon interactions in solids[28, 95].

In an inelastic process, a tunneling electron with energy $eV \geq \hbar\omega_0$ [where ω_0 is the frequency of any intermediate boson (excitation)], can excite, for example, a phonon. Because such a phonon excitation provides an additional tunneling channel, it gives rise to a linear increase in current flow for $V \geq \hbar\omega_0/e$ and thus a step increase in conductance at the threshold voltage. In $\mathrm{d}^2I/\mathrm{d}V^2 - V$, a peak results in one bias polarity and a dip in the other polarity.

This effect is sufficiently large in tunnel diodes made of indirect semiconductors, such as Si, Ge, interband tunneling is possible at $T = 0$ by phonon emission to conserve momenta, so that it can be easily observed in the $I - V$ characteristic. In direct diodes, MS contacts, and MOS junctions, the phonon effects are orders of magnitude weaker, appearing only as fine structures superimposed on a smoothly varying background in $\mathrm{d}I/\mathrm{d}V - V$ so that they can readily be observed by measurement of $\mathrm{d}^2I/\mathrm{d}V^2$.

The previous section discussed the stationary state approach to elastic electron tunneling. Generally, *the transfer Hamiltonian approach*, which was developed originally to explain the energy gap and the quasiparticle density of states in metal-insulator-superconductor tunneling[96], has been most widely employed to study inelastic electron tunneling, i.e., many-body interactions. However, this section discusses an inelastic electron tunneling on the basis of a stationary state theory of two-channel (elastic and inelastic) processes due to inelastic excitation of bulk phonons at the junction interfaces by Adler *et al.*[97], similar to a standard theory of inelastic atomic collision, as described by Brailsford and Davis[98]. The theory can readily be generalized to take into account other inelastic excitations such as metal plasmons at the interfaces, or oxide vibrations in the insulating barrier. The model is illustrated schematically in Fig. 4.

It is of interest because it gives an indication, within *a one-electron picture*, of the effects on the observed inelastic phonon spectra which depend specifically on the location x of the electron-phonon interaction, described mathematically by a position-dependent matrix element $M(x)$,

$$M(x) = \int \phi_1^*(\xi) H_{ev}(x,\xi) \phi_0(\xi)\, d\xi. \tag{15}$$

In this fashion, a uniform treatment of phonon generation at the edge of the electrode or in the barrier itself becomes possible. The Hamiltonian for the system is taken as

$$H(x,\xi) = H_e(x) + H_v(\xi) + H_{ev}(x,\xi), \tag{16}$$

where the free-particle term $H_e(x)$ contains the barrier $V(x)$, and $H_v(\xi)$, with vibrational wave function $\phi(\xi)$, represents the lattice vibration. The total wave function $\Psi(x,\xi)$ is approximated as

$$\Psi(x,\xi) = \psi_0(x)\phi_0(\xi) + \psi_1(x)\phi_1(\xi), \tag{17}$$

where $\phi_0(\xi)$ and $\phi_1(\xi)$ are the ground and the first excited-state wave functions of the vibration corresponding to energies E_{v0}, E_{v1}, respectively, such that $E_{v1} - E_{v0} = \hbar\omega$. The two stationary electron waves ψ_0 and ψ_1 are determined by substituting (17) into (16), which yields, setting $E_{v0} = 0$,

$$\begin{aligned} H_e(x)\psi_0(x) + M(x)\psi_1(x) &= E\psi_0(x) && (18) \\ H_e(x)\psi_1(x) + M(x)\psi_0(\xi) &= (E - \hbar\omega)\psi_1(x) && (19) \end{aligned}$$

with $M(x)$ given by (15). These equations were solved by Brailsford and Davis.

Taking the interaction $M(x)$ to be nonzero in only a narrow region of the electrode at the edge of the barrier. Adler et al. find a transmission probability

$$|T|^2 = |T_0|^2 + \left(1 - \frac{\hbar\omega}{E}\right)^{1/2} |T_1|^2\, \theta\,(E - \hbar\omega). \tag{20}$$

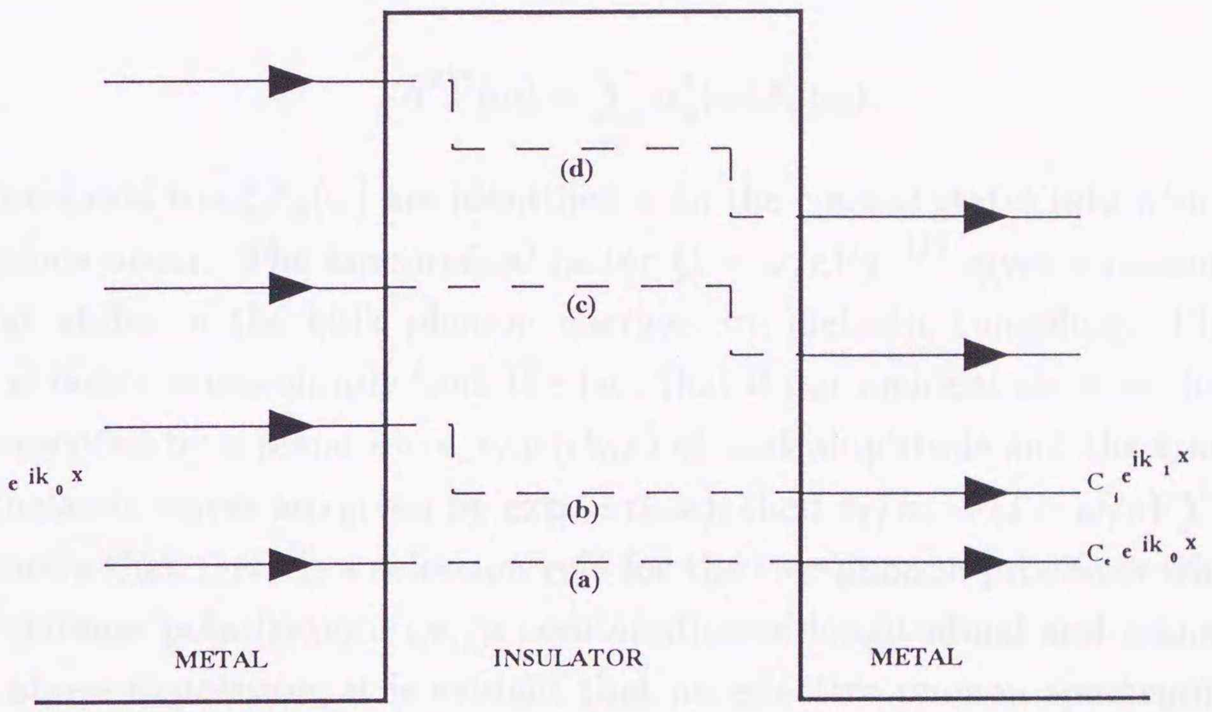

Figure 4: Schematic diagram of model showing (a) the elastic channel, (b) and (c) inelastic phonon generation at each interface, and (d) two-phonon generation at both interfaces.

The second term, when integrated over $F(\omega)\,d\omega$ up to $\omega = E/\hbar$, with $F(\omega)$ the (bare) phonon density of states, gives the inelastic assisted conductance. From (20), we obtain the following expression

$$\frac{1}{\sigma_0}\frac{d\sigma}{dV} \propto \frac{1}{2V^2}\int_0^{eV} \frac{|M(\omega)|^2\,\omega F(\omega)\,d\omega}{(1-\omega/eV)^{1/2}}, \tag{21}$$

in which $\sigma = \mathrm{d}I/\mathrm{d}V$; σ_0 is the elastic conductance evaluated at $V = 0$, with V the bias voltage; and the matrix element $|M(\omega)|^2$ is identified with the electron-phonon coupling function $\alpha^2(\omega)$. Therefore, we obtain

$$\frac{1}{\sigma_0}\frac{d\sigma}{dV} \propto \frac{1}{2V^2}\int_0^{eV} \frac{\alpha^2(\omega)\,\omega F(\omega)\,d\omega}{(1-\omega/eV)^{1/2}}, \tag{22}$$

where

$$\alpha^2 F(\omega) = \sum_{\mathbf{q}} \alpha^2_{\mathbf{q}}(\omega) F_{\mathbf{q}}(\omega). \tag{23}$$

The $\mathbf{q}$ subscripted to $\alpha^2_{\mathbf{q}} F_{\mathbf{q}}(\omega)$ are identified with the cone of states into which the tunneling transitions occur. The kinematical factor $(1-\omega/eV)^{-1/2}$ gives a reasonable account of the peak shifts in the bulk phonon energies by inelastic tunneling. Physically, this kinematical factor arises simply from the fact that if our incident electron flux on the barrier is represented by a plane wave, $\exp(\imath k_0 x)$ of unit amplitude and the transmitted and reflected inelastic waves are given by $\exp(\pm\imath k_1 x)$, then $k_1/k_0 = (1-\omega/eV)^{1/2}$. The analysis also shows that there is a selection rule for the two-phonon processes which precludes mixing of phonon polarization, i.e., a combination of longitudinal and transverse modes. From the above expression, it is evident that an effective phonon spectrum $\alpha^2(\omega)F(\omega)$ is involved in the $\mathrm{d}^2I/\mathrm{d}V^2$ characteristics. As one approximation of (22), we can write the second derivative as follows :

$$\frac{d\sigma}{dV} \propto \sigma_0 \sum_{\mathbf{q}} \alpha^2_{\mathbf{q}}(\omega) F_{\mathbf{q}}(\omega) \propto \sum_{\mathbf{q}} \alpha^2_{\mathbf{q}}(\omega) F_{\mathbf{q}}(\omega). \tag{24}$$

The approximation means that we ignore the smoothing background effect and the effect of peak shifts by the kinematical factor. From (24), it follows that $\mathrm{d}\sigma/\mathrm{d}V$ is proportional to the spectral density of states for the excitation with energy $\omega = eV$, averaged over the momenta $\mathbf{q}$ with a weight determined by the coupling function (and more specifically, the "form factor", $\alpha^2_{\mathbf{q}}(\omega)\epsilon^2_{\mathbf{q}}$, where $\epsilon_{\mathbf{q}}$ is the polarization of the excitation) of the creation of the excitation with momentum $\mathbf{q}$.

In a case, where the electrodes are dissimilar and only one has strong electron-phonon coupling, inversion of (22) yields the formula[99]

$$\alpha^2(\omega)F(\omega) \propto \frac{2}{\pi}\frac{d}{d\omega}\int_0^{\omega} \frac{V^{3/2} d\sigma/dV\, dV}{(\omega - eV)^{1/2}}, \tag{25}$$

through which an effective phonon spectrum, $\alpha^2(\omega)F(\omega)$, can properly be extracted from normal state $\mathrm{d}^2I/\mathrm{d}V^2$ data.

It is well known that van Hove singularities arise from points in $\mathbf{q}$ space where $\nabla_{\mathbf{q}}(\omega)$ vanishes, since $F(\omega)$ is directly proportional to the $\mathbf{q}$ space volume, $\int \mathrm{d}\mathbf{q}$ in a shell between constant energy surfaces S_ω at ω and $\omega + \mathrm{d}\omega$[100, 101]. Since the normal thickness $\mathrm{d}k_n$ of the shell is given by the relation $|\nabla_{\mathbf{q}}(\omega)|\ \mathrm{d}k_n = \mathrm{d}\omega$, one has, with $\mathrm{d}^2k_t = \mathrm{d}S$,

$$F(\omega) = \frac{V}{(2\pi)^3}\int_{S_\omega}\frac{dS}{|\nabla_{\mathbf{q}}(\omega)|}, \tag{26}$$

which has van Hove singularities at critical points of $\omega(\mathbf{q})$, points where all the derivatives in the gradient vanish. These considerations have been carefully discussed in connection with tunneling $\alpha^2F(\omega)$ measurements by Scalapino and Anderson[102]. From the above discussion, the density of states, $F(\omega)$ is high in regions at $\nabla_{\mathbf{q}}\omega=0$. The second derivative $\mathrm{d}^2I/\mathrm{d}V^2$ peaks thus correspond to the singular points at $\nabla_{\mathbf{q}}\omega=0$ in the dispersion curves which are usually located at Brillouin zone centers or edges (in some cases, intermediate $\mathbf{q}$ values[103, 104]).

The interpretation of the experimental results depends essentially on the *selection rules*. In the inelastic tunneling process it is necessary to satisfy the energy conservation law[105]

$$E(\mathbf{k}_1) = E(\mathbf{k}_2) + \hbar\omega_{\mathbf{q}}. \tag{27}$$

In addition, if the excitation of the quasiparticles is *coherent*, then the momentum component tangential to the barrier should also be conserved[105]:

$$\mathbf{k}_1^{\|} = \mathbf{k}_2^{\|} + \mathbf{q}^{\|}. \tag{28}$$

The above inelastic process represents phonon emission process only. It should be noted that in the inelastic tunneling process both phonon emission and absorption process are possible at room temperatures. However, only phonon emission process is possible at low temperatures which tunneling experiments are usually carried out. This fact can be easily considered as follows. The average number n of phonons with a wave number q at thermal equilibrium is given by Planck distribution:

$$n(q) = \frac{1}{\exp(\hbar\omega_{\mathbf{q}}/k_BT) - 1}. \tag{29}$$

Usually, the value of $\hbar\omega_{\mathbf{q}}/k_B$ is at least about 100 K (, which corresponds to the energy value of 10 meV.) When we assume the tunneling experiment at 4.2 K, $\hbar\omega_{\mathbf{q}}/k_BT \approx 25$. Therefore the average number n substantially becomes zero.

The conservation law for the parallel component of the quasimomentum is satisfied only if the system is homogeneous in directions tangent to the barrier, i.e., the barrier does not contain random scattering centers, and the reflection of the electrons from the boundaries between the electrode and the oxide is specular. Let us consider the excitation produced either in the barrier layer itself or in the immediate vicinity of this layer. The effective interaction with phonons will be observed only for electrons traveling at small angles about the barrier normal direction, since the only electrons penetrating deep into the barrier are those moving almost perpendicular to the surface of the junction. Consequently, phonons with small $\mathbf{q}^{\|}$ will be mainly produced. The polarization of such phonons should be *transverse* for maximum interaction with the tunneling electrons. If the barrier contains a large number of scattering centers then the law of conservation of the parallel component of the quasimomentum will not hold. There should be observed in the spectrum an intense line corresponding to *longitudinal* phonons. For the phonons produced in the metallic films, in order to be able to consider the tunneling process and the phonon emission process as simultaneous, it must be assumed that the phonons are produced in a narrow layer of metal near the boundary with the barrier, the width of which is of the order of $\lambda = [4\pi e^2 N(E_F)]^{-1/2}$. The existence of selection rule for the wave vector can be closely associated with the probing of the anisotropy of the electronic structures and phonons in the next section.

Aside from the inversion of inelastic tunneling conductance above described, starting from the paper of Svistunov et al.[106], fresh attention has been paid to the problem of elastic tunneling between the electrodes of normal metals, as it became possible to derive the frequency dependence of the electron-phonon coupling function from *elastic* electron tunneling conductance data. The dependence of the odd part of the conductance, $\sigma_-(\omega) = [\sigma(\omega) - \sigma(-\omega)]/2$, on the real part of the phonon-induced electron-self energy, $\Sigma(\omega) = \Sigma_1(\omega) + i\Sigma_2(\omega)$, was postulated by Hermann and Shmid[107][†]. The presence of the self-energy-induced structure in the tunneling conductance has been corroborated experimentally by Rowell et al.[108] and Burrafato et al.[109], and more recently by Svistunov et al.[106] and Chernyak et al.[110]. Appelbaum and Brinkmann[111] suggested that the structure observable in the odd part of the tunneling conductance is caused by a weak momentum dependence of the self-energy or the pre-exponential factors of the tunneling matrix element. Leavens, assuming the weak momentum dependence of the electron self-energy, has derived a formula[112]:

$$\sigma_-(eV) = \sigma_0 \left[(\gamma_a/\mu_a)\Sigma_1^a(eV) - (\gamma_b/\mu_b)\Sigma_1^b(-eV) - \delta eV \right]. \tag{30}$$

Here σ_0 is the tunneling conductance in the absence of self-energy effects, $\mu_{a,b}$ is the chemical potential, and $\gamma_{a,b}$ is a constant of order unity, and δ depends on the properties of both electrodes. One may choose the two different metal electrodes of the tunnel

---

[†] The $\mathrm{d}^2I/\mathrm{d}V^2$ peaks are not inverted at ±V for the self-energy effect.

junction in such a way that $\alpha^2 F_a(\omega) \gg \alpha^2 F_b(\omega)$ in the frequency range characteristic to $\alpha^2 F_a(\omega)$. Assuming further that γ_a/μ_a is comparable to or greater than (γ_b/μ_b), the self-energy effects of metal b in the odd part of the tunneling conductance described by equation (30) may be neglected. Let us define the experimental conductance, $\sigma_-^{ex}(eV)$, as

$$\sigma_-^{ex} = \sigma_-(eV) + aeV, \tag{31}$$

where

$$\sigma_-(eV) = -\sigma_0(\gamma/\mu)\Sigma_1(eV), \tag{32}$$

and the constant a contains all the contributions linear with voltage. (Notice that some of the indices are skipped as they are no longer necessary.) Thus, having measured the conductance of the normal metal tunnel junction consisting of appropriately chosen metals, one can derive the real part of the electron self-energy in one of the electrodes, providing one finds a way to eliminate the linear part of $\sigma_-^{ex}(eV)$.

The dispersion relation:

$$\Sigma_2(\omega) - \Sigma_2(\infty) = \frac{2}{\pi}\int_0^\infty d\Omega\, \frac{\Omega\Sigma_1(\Omega)}{\omega^2 - \Omega^2}, \tag{33}$$

where

$$\Sigma_2(\infty) = -\pi A^2, \qquad A^2 = \int_0^\infty d\omega\, \alpha^2 F(\omega), \tag{34}$$

from which Svistunov et al.[106] derived the final equation of the inversion method, may be immediately obtained from another dispersion relation,

$$\frac{d\Sigma_2(\omega)}{d\omega} = \frac{2\omega}{\pi}\int_0^\infty d\Omega\, \frac{d\Sigma_1(\Omega)}{d\Omega}\frac{1}{\omega^2 - \Omega^2}, \tag{35}$$

since the derivative of an analytic function is also an analytic function. We obtain the dispersion relation from integration by parts of (35):

$$\frac{d\Sigma_2(\omega)}{d\omega} = -4\frac{\omega}{\pi}\int_0^\infty d\Omega\, \frac{\Omega\Sigma_1(\Omega)}{(\omega^2 - \Omega^2)^2}. \tag{36}$$

Using the well known result for the phonon contribution to the electron self-energy,

$$\Sigma(\omega) = \int_0^{\omega_0} d\nu\, \alpha^2 F(\nu) \ln\left|\frac{\nu - \omega}{\nu + \omega}\right| - \imath\pi \int_0^{|\omega|} d\nu\, \alpha^2 F(\nu) \tag{37}$$

obtained from the Eliashberg equations at zero temperature[113], and (32), (36) Wnuk derived a formula connecting the Eliashberg function directly with the odd part of the tunneling conductance[114, 115]:

$$\alpha^2 F(\omega) = -\frac{\mu}{\sigma_0 \gamma}\frac{4\omega}{\pi^2}\int_0^\infty d\nu \frac{\nu\sigma_-(\nu)}{(\omega^2 - \nu^2)^2}. \tag{38}$$

The inversion methods allow the extraction of the frequency dependence of the electron-phonon interaction function, $\alpha^2F(\omega)$, derived not only from the superconductive but also normal metal tunneling conductance data, taking into account either elastic or inelastic tunneling channel. The account of other effects may be estimated by comparison of the functions $\alpha^2F(\omega)$ obtained from superconductive and normal metal tunneling experiments performed on the same tunnel junction. Then, the comparison between the Eliashberg functions derived from the even part and the odd part of the normal tunneling conductance leads us to resolve the problem of different tunneling channels in a normal metal junction[116].

One may question the role of the "interference" term, which should appear in the tunneling conductance together with the elastic and inelastic contributions. Ivanchenko and Medevedev[117] together with Belogolovskii[118, 119] suggested that the tunneling current flowing between two normal electrodes should consist of at least three terms (if we consider only the interactions between the tunneling electrons and phonons),

$$I(eV) \;=\; I_{el}(eV) + I_{ie}(eV) + I_i(eV).$$

Two of them are known and come from *elastic* (I_{el}) and *inelastic* (I_{ie}) tunneling channels. The *interference* (I_i) contribution has the same symmetry and is of the same order as the elastic one, but has opposite sign. The net effect on the odd part of the tunneling conductance is that it would be weakened at higher frequencies:

$$\alpha^2F(\omega) \;\rightarrow\; [1-\varphi(\omega)]\,\alpha^2F(\omega).$$

Here, $\varphi(\omega)$ is a smooth function, normalized to unity, that increases with frequency. Belogolovskii et al.[118, 119] explain the frequency-dependent dumping of the odd conductance curve of and Al-I-Sn junction[109] by the existence of this additional term. One could interpret the *elastic* and *interference* terms together as the partial "undressing" of the tunneling electron from many-body interaction[120] characteristic of the bulk electrode, which is quite convincing knowing that in the case of normal metal junctions tunneling electrons probe only a few atomic layers of the electrodes. However, it is not clear why the same should not be true for the inelastic tunneling process. An experiment with an Al-I-Pb junction has shown that the *low*-frequency part of $\alpha^2F(\omega)$ is dumped (transverse peak of $\alpha^2F(\omega)$ spectrum of Pb). This was again explained as due to the metal-insulator interface and short depth to which tunneling electrons probe the normal metal[97]. This line of reasoning could lead to a hypothesis that at the surface of a normal metal the probability weights of taking part in inelastic and elastic tunneling processes are different for transverse and longitudinal phonons. It is probably accidental, but the ratios between the magnitude of the transverse to longitudinal peaks in $\alpha^2F(\omega)$ deduced from inelastic tunneling experiment[97] and elastic one[108] are exactly reversed. However, there may be still another explanation for the rounding and change of the relative magnitude of the electron-phonon interaction function of Pb obtained from the normal metal tunneling-simply disorder present at the metal-insulator interface[121].

2.1.4 Probing Anisotropy of Fermi Surfaces and Phonons by Electron Tunneling

The elementary theory of tunneling through a potential barrier strongly favors transitions with $\mathbf{k}$ perpendicular to the surface, into a cone of opening angle 5° – 10°[28, 122, 123]. Thus, to the extent that barrier tunneling is regarded as a direction, with most electrons injected in the above cone of angle about the barrier normal direction, the confirmed anisotropy of Fermi surfaces and phonons in real materials would be expected to produce anisotropic energy band and phonon structures including in the tunneling characteristics. Surprisingly, there seems at present to be no good example of this expected effect from barrier tunneling, *although* such effects have been observed in a related experiment, that of point-contact spectroscopy for Zn observed in two mutually perpendicular directions[124]. To consider anisotropic effects in tunneling spectroscopy, this section discusses an example from superconductive tunneling, which has been most in detail investigated[125]. We could obtain valuable information about the observation of anisotropic band and phonon structures in tunneling spectroscopy from this consideration. Before the following discussion, there is one thing to be noted. We notice that the energy gap is not tied to the lattice - it is not, as in a semiconductor, fixed to the zone boundaries in repeated space - , but simply occurs at the Fermi level.

The understanding of anisotropic $\Delta_{\mathbf{k}}$, or $\alpha^2_{\mathbf{k}}(\omega)\, F_{\mathbf{k}}(\omega)$ is basically based upon the following equations[28]

$$\Delta_{\mathbf{k}} = \sum_{\mathbf{k}'} V_{\mathbf{k},\mathbf{k}'} \frac{\Delta'_{\mathbf{k}}}{2E_{\mathbf{k}'}} \left[1 - 2f\left(E_{\mathbf{k}'}\right)\right], \tag{39}$$

$$\alpha^2_{\mathbf{k}}(\omega)\, F_{\mathbf{k}}(\omega) = \frac{1}{(2\pi)^3} \int \frac{dS'_{\mathbf{k}}}{\hbar \left|\mathbf{v}'_{\mathbf{k}}\right|} \sum_{\lambda} \left|g_{\mathbf{k}',\mathbf{k},\lambda}\right|^2 \delta\left[\omega - \omega_{\lambda,\mathbf{k}'-\mathbf{k}}\right], \tag{40}$$

where $E_{\mathbf{k}} \equiv (\epsilon^2_{\mathbf{k}} + \Delta^2_{\mathbf{k}})^{1/2}$, $\Delta_{\mathbf{k}}$ is the $\mathbf{k}$-dependent gap function, $V_{\mathbf{k},\mathbf{k}'}$ is the $\mathbf{k}$-dependent attractive interaction, f is the Fermi function, $\mathbf{v}'_{\mathbf{k}}$ is the group velocity, $\mathrm{d}S_{\mathbf{k}}$ is an element of Fermi surface area, and $g_{\mathbf{k}',\mathbf{k},\lambda}$ is the electron-phonon coupling matrix element, which describes electron scattering from $\mathbf{k}$ to $\mathbf{k}'$ on the Fermi surface with creation of a phonon of energy $\hbar\omega_{\lambda,\mathbf{k}'-\mathbf{k}}$ and polarization λ. The quantity, $\alpha^2_{\mathbf{k}}(\omega)\, F_{\mathbf{k}}(\omega)$ is dimensionless. Here the $\mathbf{k}$ subscripted to $\Delta_{\mathbf{k}}$ or $\alpha^2_{\mathbf{k}}(\omega)F_{\mathbf{k}}(\omega)$ are identified with the cone of states into which the tunneling transitions occur. It is evident that the possibility of $\Delta_{\mathbf{k}}$ being, in fact, dependent upon the direction of $\mathbf{k}$, is implicit in the above BCS gap equation if the interaction $V_{\mathbf{k},\mathbf{k}'}$ is $\mathbf{k}$-dependent or if the Fermi surface (sum over $\mathbf{k}'$) is anisotropic. There are two main sources of anisotropy in $V_{\mathbf{k},\mathbf{k}'}$: the electron-phonon matrix element, $g_{\mathbf{k}',\mathbf{k},\lambda}$ and the phonon spectrum, $F(\omega)$. In this meaning, the first equation is closely linked with the second equation. Also there are several sources of $\mathbf{k}$ dependence in (40). These are the phonon frequencies $\omega_{\lambda,\mathbf{k}'-\mathbf{k}}$, the Fermi surface geometry, the electronic wave functions, the group velocities $\mathbf{v_k}$; and the electron-phonon interaction $g_{\mathbf{k}',\mathbf{k},\lambda}$.

In the clean limit, if the angular variation of $\Delta_{\mathbf{k}}$ is large enough, and if the barrier growth is well behaved, measurement of $\Delta_{\mathbf{k}}$ should be possible, with angular resolution on the order of this cone angle, by a sequence of junctions formed on different faces of the superconductor. In fact, several experimental results are reported[125, 126], and it is found that preference is given to cases in which a free crystal serves as a substrate, with an evaporated film, preferably of the same metal, as counterelectrode. This configuration minimizes the opportunity for strains to occur in cooling from the fabrication temperature to the measurement temperature of typically 1 K, which can produce comparable gap energy shifts unrelated to anisotropy. Thin films of the superconductor are believed to be undesirable because microcrystals of many different orientations may be present and also because scattering at the film boundaries and at internal grain boundaries can lead to the dirty superconductor situation, with an averaged isotropic gap. Thick, epitaxial, single-crystal films, in which strain is minimized by reasonable matching of thermal expansion coefficients[126], have been used in the case of Pb and give results in good agreement with those obtained from freestanding single crystals. This demonstrates a clear trend of variation well above the local fluctuation. However, tunneling measurements of anisotropy are generally difficult and subject to reduction and distortion by several extraneous factors. Reduced anisotropy is a result of scattering rapid enough to produce an isotropic average gap. Since tunneling is an inherently surface-sensitive measurement, the condition $l/\xi_0 \gg 1$ (l: electron mean free path, ξ_0: coherence length) may not be satisfied in the sampled region of thickness $\sim \xi$, even though measurement of the residual resistance ratio of the bulk specimen may imply clean conditions in the bulk. This effect may account for the lack of tunneling evidence for anisotropy in Nb and other transition metals. Distortion of measurement by strain, either uniform or random and obscuring features, is also a severe problem in an experiment where a sandwich of dissimilar materials is required.

For the confirmed anisotropy of Fermi surfaces, which results from contributions from different sheets of Fermi surfaces and phonons in normal, real and clean materials, the anisotropic $\alpha^2(\omega)F(\omega)$ function would be expected to be produced, deduced from tunneling into different crystalline faces. One may ask why similar effects have not yet been seen in barrier tunneling spectroscopy. There appears to be no consensus on this point. The requirement of little scattering, i.e., that the single-crystal electrode be in the clean limit, is often attained in the usual bulk sense, although it is probably more pertinent and at the same time more difficult to establish clean conditions specifically in the surface region of the electrode actually being sampled. The detailed nature of the oxide-metal interface is also possibly relevant as a source of local strains or dissolved gases which may produce locally dirty conditions.

An additional event arises when one consider semiconductors and semimetals with multi-valley bands such as Ge, Si, Bi, and Sb, etc., as compared with metals. It is *an anisotropy of the intravalley scattering*[†][127]. For the intravalley scattering, it is known that the transition probability or scattering by transverse as well as the longitudinal modes are functions of the angle between the phonon wave vector $\mathbf{q}$ and the vector $\mathbf{k_0}$ from the origin of the $\mathbf{k}$ space to the center of the nonspherical volume. The above fact may help us to probe the anisotropy of Fermi surfaces and phonons in a manner different than in the case of normal metals. That is, it is likely that the change in either the intensity of the intravalley acoustic phonon peak or the shape of the tunneling conductance occurs dependent on the exposed crystal faces because of the different scattering cross section and the final density of states tunneling electrons see. Probing Fermi surfaces and phonons in multivalley semiconductors and semimetals is on the basis of the fact that the electronic structures and the excitations of phonons are closely correlated.

In relation to the above matter, in the usual version of the electron-phonon N process, it is assumed that electrons can be scattered by phonons with all wave vectors $|\mathbf{q}| \leq q_D$, where q_D corresponds to the cut-off frequency of the Debye spectrum (the Debye sphere radius)[95]. This fact is well known in the theory of semiconductors, and has also been taken into account in Frölich's theory of superconductivity[128]; however, its consequence for the theory of normal metals and semimetals do not particularly seem to have been noticed. In metals and semimetals, it is only necessary to consider electrons with wave vectors $|\mathbf{k}| = k_0$ corresponding to the surface of the Fermi distribution. It follows that, if $2k_F$, the diameter of the Fermi sphere, is smaller than q_D, the upper limit of integration in the collision operator is $2k_F$, and not q_D. In any scattering involving an electron with wave vector $\mathbf{k}$ and a phonon with wave vector $\mathbf{q}$, the laws of conservation of energy and momentum require that $|\mathbf{k}| = |\mathbf{k} \pm \mathbf{q}|$. It should be noted that an electron in the state $\mathbf{k}$ can only interact with phonons with wave vectors for which $|\mathbf{q}| \leq 2|\mathbf{k}|$[129]. When this, the effective Debye temperature Θ_e^*, associated with the intravalley scattering is given by

$$\Theta_e^* = (2k_e/q_D)\,\Theta \qquad \textit{or} \qquad k_B\Theta_e^* = \hbar v_s(2k_e), \tag{41}$$

where k_B is the Boltzmann constant and v_s is the sound velocity average. The same

---

[†] Within each pocket electrons are scattered from acoustic phonons. Small wave vector phonons are involved in this *intravalley* scattering. On the other hand, short wave length phonons with wave vectors near the boundary of the Brillouin zone contribute to the *intervalley* scattering.

expression is valid for Θ_h^*.

2.2 Narrow Gap Semiconductor Antimony Telluride and Semimetal Antimony

2.2.1 V-VI Narrow Gap Semiconductor Antimony telluride

This section describes a general property of antimony telluride used in this study. Antimony telluride (Sb_2Te_3), like other V_2VI_3 compounds, is an anisotropic, rhombohedral layer-type narrow-gap semiconductor with the symmetry $R\bar{3}m$ (D_{3d}^5). The structure is composed of alternate layers of antimony and tellurium atoms normal to the threefold axis. It has a perfect cleavage perpendicular to the c axis. It shows therefore strong anisotropic behavior. There are five atoms per unit cell and consequently Sb_2Te_3 exhibits 15 phonon modes for each wave vector $\mathbf{q}$[130]. The conductivity is always found to be p-type despite numerous attempts to produce n-type material by impurity doping or by deviation from stoichiometry. The free carriers concentration lies in the range $10^{19} - 10^{20}$ cm^{-3}[131, 132, 133]. It has been suggested that a wrong atom defect[134], being a natural consequence of the parameters characterizing the crystal bonds, is responsible for this characteristic conductivity. It is considered that the hole conductivity of p-type antimony telluride is connected with the existence of $Sb_{Te}^{'}$ defects whose charge is compensated by holes. The sequence of layers is as follows:

$$\text{-Te}^1\text{]-[Te}^1\text{-Sb-Te}^2\text{-Sb-Te}^1\text{]-[Te}^1\text{-Sb-Te}^2\text{-Sb-Te}^1\text{]-[Te}^1\text{-}$$

The binding energy between Sb and Te layer is generally considered to be predominantly covalent. The easy cleavage of the material is believed to be due to weak forces (Van der Waals forces and possibly some Coulomb interaction) between the Te^1 layers. In other words, the structure of these compounds consists of packages or sandwiches of five layers [Te^1-Sb-Te^2-Sb-Te^1] with covalent bonds within the sandwiches and weak bonds between them. The arrangement of the crystal section is shown in Fig. 5. For clarity, only three atomic layers are depicted: the layer Te^1, Sb, Te^2. The next Sb layer has the same arrangement as the Te^1 layer and the following Te^2 layer is of the same type as the Sb layer shown. The atomic planes forming one five layer stack are thus arranged in an ABCAB pattern. The bonds shown in the figure are drawn with respect to Sb.

According to Drabble and Goodman[135], the V–VI^1 bonds show more ionicity whereas the V-VI^2 bonds have a covalent character. Horák, Starý, and Klikorka[136] have carried out a quantum chemical calculation of bonding parameters in antimony telluride. Their results are in agreement with the qualitative ideas on the bonding by Drabble and Goodman. Their calculations show that higher bond polarity corresponds to shorter interatomic distances and also shorter distance between the atomic planes. Sb atoms carry

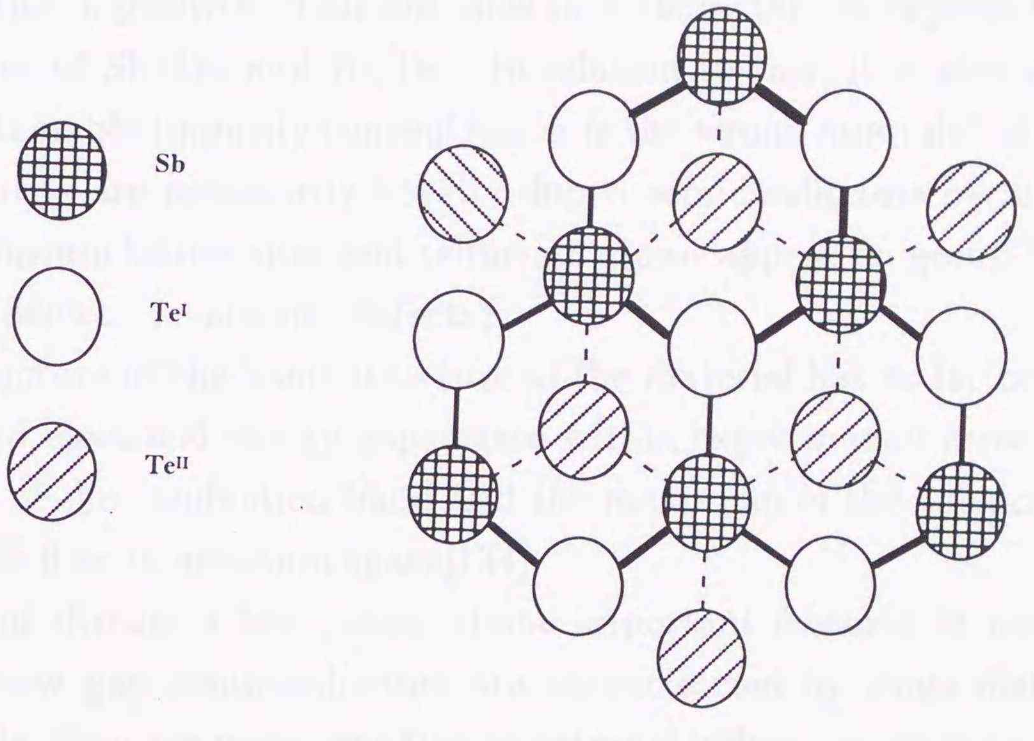

Figure 5: Illustration of the first three atomic networks in layer compound semiconductor Sb_2Te_3. The bonds shown in the figure are drawn with respect to Sb atoms.

a smaller positive charge than Bi atoms; in antimony telluride crystals there is a weaker shift of the electron density towards Te^1 and Te^2 than in bismuth telluride. Furthermore, electrostatic repulsion between the layers takes place in antimony telluride to a smaller degree. Hence one can expect a smaller width of the van der Waals gap in antimony telluride. It was shown[137] that in more ionic crystals, i.e., in crystals with a higher bond polarity, the probability of formation of antisite defects tends to be low. A comparison of the concentration of AS defects in Sb_2Te_3 and Bi_2Te_3 confirms the correctness of this view; the crystals prepared from stoichiometric melts show the following concentrations of antisite defects $[Sb'_{Te}]$ (p-Sb_2Te_3) $= 8 \times 10^{19}$ cm^{-3}, $[Bi'_{Te}]$ (p-Bi_2Te_3) $= 1 \times 10^{19}$ cm^{-3}. The markedly higher concentration of AS defects in Sb_2Te_3 compared to Bi_2Te_3, is intimately connected with the bond polarity. Contrary to the situation in Bi_2Te_3, the charge of Te^2 in Sb_2Te_3 lattice is positive. This circumstance characterizes expressively the differences in the behavior of Sb_2Te_3 and Bi_2Te_3. In relation to this, it is also suggested[134] that the lowest obtainable impurity concentration is the wrong atom defect level, and that the V–VI compounds are necessarily heavily doped semiconductors because group V atoms appear on tellurium lattice sites and tellurium atoms appear on group V atom lattice sites (wrong atom defects, or antisite defects).

No clear picture of the band structure of the material has so far been reported. Since the optical and electrical energy gaps agree within experimental error, one would expect the minimum of the conduction band and the maximum of the valence band or bands to occur near $k = 0$ in momentum space[134].

Next, let us discuss a few points about important features in narrow gap semiconductors. Narrow gap semiconductors are characterized by some distinct features[138]. Experimentally, they are more sensitive to external influences, such as temperature, magnetic field, electric field, and deformation, than the standard semiconductor materials. Theoretically, they require a description, which is closely analogous to the relativistic quantum mechanics. The electrons in a narrow gap semiconductor combine features of free particles (continuous spectrum) and those of atomic state (energy gap, spin-orbit interaction). This combination results in a variety of new physical phenomena. The *small effective masses* inherent in narrow gap semiconductors make them the obvious candidates to observe quantum confinement effects at larger dimensions than in materials of larger effective mass and wider gap[139, 140]. Perhaps, the most unusual features of narrow gap semiconductors are found in *their surface and interface properties.* For wider energy gap materials, many of the relevant energy positions for interfaces are in the gap. For example, the position of the metal Fermi energy at metal-semiconductor interfaces is typically located well inside the energy gap of the semiconductor, leading to the typical Schottky barrier behavior. With small energy gaps, the possible locations of these energies within the gap are more restricted because of the narrow gap, leading to some rather unusual positions for the interface energies.

Three-level band model describes quite well the general properties in isotropic narrow-gap semiconductors such as the conduction band in InSb-type semiconductors which are cubic materials with band extrema at the Γ point. It should be particularly noted that we do not have any model which can describe anisotropic V-VI materials such as Sb_2Te_3 in this study. There are *three* important features resulting from this model: 1) electron and hole $E(\mathbf{k})$ dispersion relations are *nonparabolic*, 2) the wave functions are *mixtures of s-like and p-like periodic components*, 3) the wave functions are *mixtures of spin-up and spin-down states.*

In absence of a magnetic field $\mathbf{H}$ and a static scalar potential $U(\mathbf{r})$, the resulting $E(\mathbf{k})$ dependence can be obtained from the famous Kane equation[138, 141]

$$E^{'}\left(E^{'}+E_{g}^{'}\right)\left(E^{'}+E_{g}^{'}+\Delta\right)-\kappa^{2}k^{2}\left(E^{'}+E_{g}^{'}+\frac{2}{3}\Delta\right)=0, \tag{42}$$

where Δ is the spin-orbit splitting of valence bands. From (42), it is possible to define the dispersion relation of interacting bands. Here $E^{'}=E-E_0=E-\hbar^2k^2/2m_0$. The conduction band is strongly nonparabolic, and the band of heavy holes is flat in this approximation.

In the particular case where $m_e \ll m_0$ (m_e: the effective mass at the conduction band edge) and $\Delta \gg E_g$, i.e., in the two-band approximation, a simple relation between k and E is obtained from (42). It has the following equation

$$E\left(1+\frac{E}{E_g}\right)=\frac{\hbar^2k^2}{2m_e}. \tag{43}$$

One solution of this quadratic equation yields the conduction band, and the other the light hole band. For $E_g \gg E$, (43) is reduced to the dispersion law of the standard, i.e., parabolic conduction band.

2.2.2 Group V Semimetal Antimony

Most of the properties that distinguish the group V semimetals including antimony used in this study from the less exotic metals or semiconductors are due to their particular crystallographic structure. This structure, which exhibits a rhombohedral A7 crystal structure, with $a = 4.5067$ Å and $\alpha = 57.1075°$ of $R\bar{3}m$ point group, may be considered as a slightly distorted cubic one, and this distortion is responsible for the small overlap between the conduction and valence bands (Fig. 6). The A7 structure, which it shares with bismuth and arsenic, may be regarded as derived from the sodium chloride structure (in which both the "sodium" and the "chlorine" sublattices are occupied by antimony) by

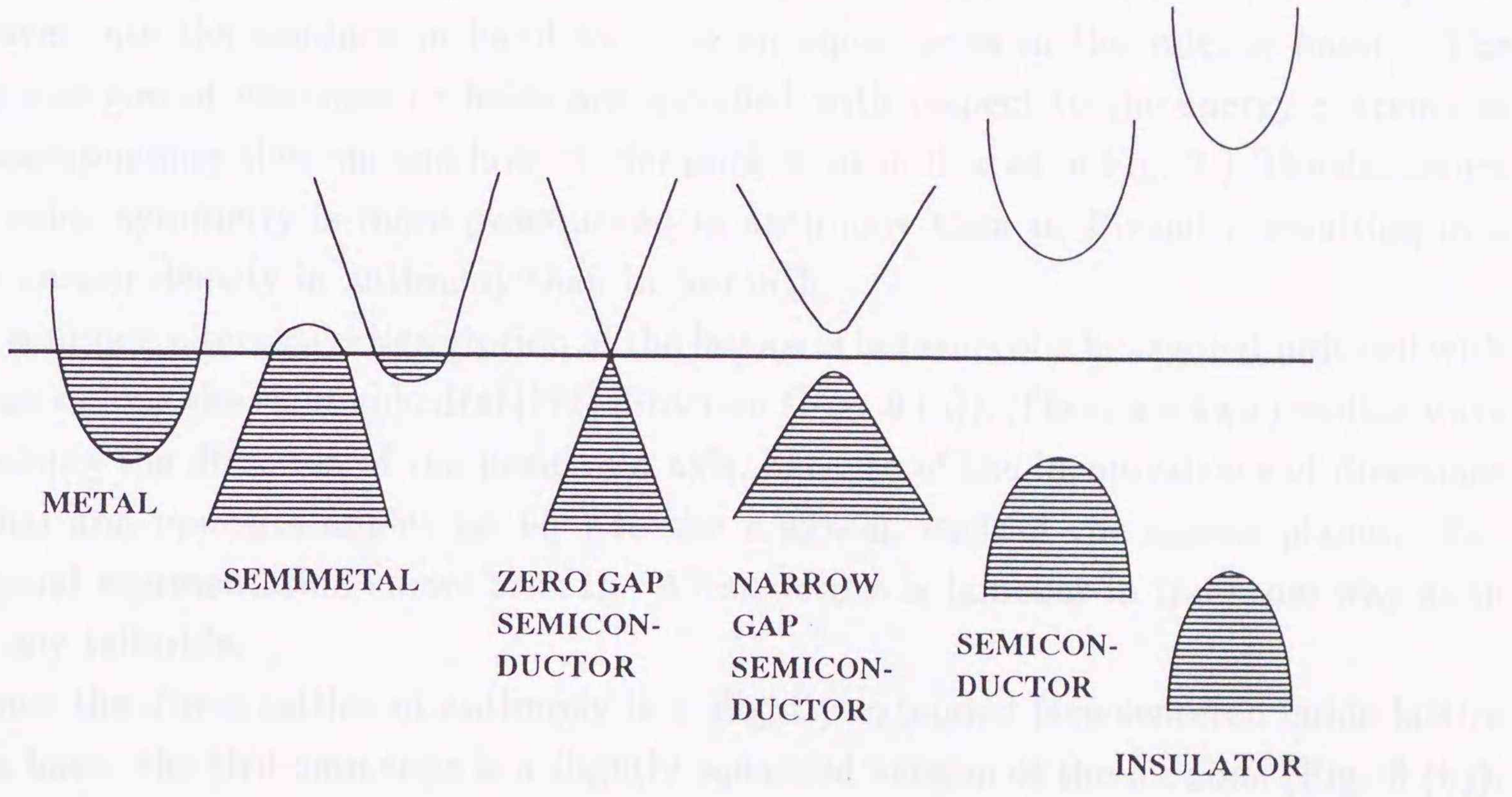

Figure 6: Comparison of the band structure of semimetals with that of other solids at low temperatures.

two consecutive distortions. The first, a small extension along a body diagonal, reduces the rhombohedral angle α to below the value of 60° which it has in the cubic case. The second distortion involves moving one sublattice relative to the other along the same body diagonal. The rhombohedral unit cell contains two atoms, one from each sublattices, and although neither of these atoms remains on a center midway between them, and this is conventionally taken as the origin of the unit cell. The two atoms in the cell then lie at $\pm\,(ua, ua, ua)$, in rhombohedral coordinates, where the distortion parameter $u = 0.23349$ for antimony, instead of 0.25 in the original cubic lattice. Of the cubic symmetry, the lattice retains only one trigonal symmetry axis (the axis of extension), perpendicular to which lie three equi-spaced binary axes, each of them perpendicular to a mirror plane.

For antimony, the fifth Brillouin zone overlaps the sixth: about 10^{-3} electrons/atom spill over into the conduction band to leave an equal holes in the valence band. (The Fermi energies of electrons or holes are specified with respect to the energy extrema in the corresponding electron and hole carrier pockets as indicated in Fig. 7.) The departure from cubic symmetry is more pronounced in antimony than in Bismuth, resulting in a larger carrier density in antimony than in bismuth.

A common alternative description of the lattice is in terms of a hexagonal unit cell with the c axis along the rhombohedral [111] direction (Fig. 8 (a)). There are two possible ways of choosing the direction of the positive a axis, because of the inequivalence of directions at equal and opposite angles ($\neq 90°$) to the c axis in each of the mirror planes. The hexagonal representation shows that the A7 structure is lamellar in the same way as in antimony telluride.

Since the direct lattice of antimony is a slightly extended face-centered cubic lattice with a basis, the Brillouin zone is a slightly squashed version of the fcc zone (Fig. 8 (b)). ΓT is the trigonal axis, and only the faces in which points T lie are regular hexagons, while the faces containing points L and X are compressed hexagons and rectangles, respectively. To make a choice of axes consistent with the direct lattice system, the x axis coincides with one of the binary axes, and the y axis lie in one of the mirror planes, such that the directions ΓX fall in the second and fourth quadrants of the YZ mirror plane. The pockets of electrons are located at the L points of the Brillouin zone whereas holes are located at the six equivalent H points. The Fermi surface of the group V semimetals is known with great accuracy at low temperatures and have been reviewed extensively[142, 143, 144]. In antimony it was found to consist of two (electrons and holes) sets of closed, somewhat, warped, prolate ellipsoids that encloses only a small part of the total Brillouin zone volume. Their sizes, locations, and tilt angles in momentum space have been correctly determined (Table 1.)[145, 146, 147].

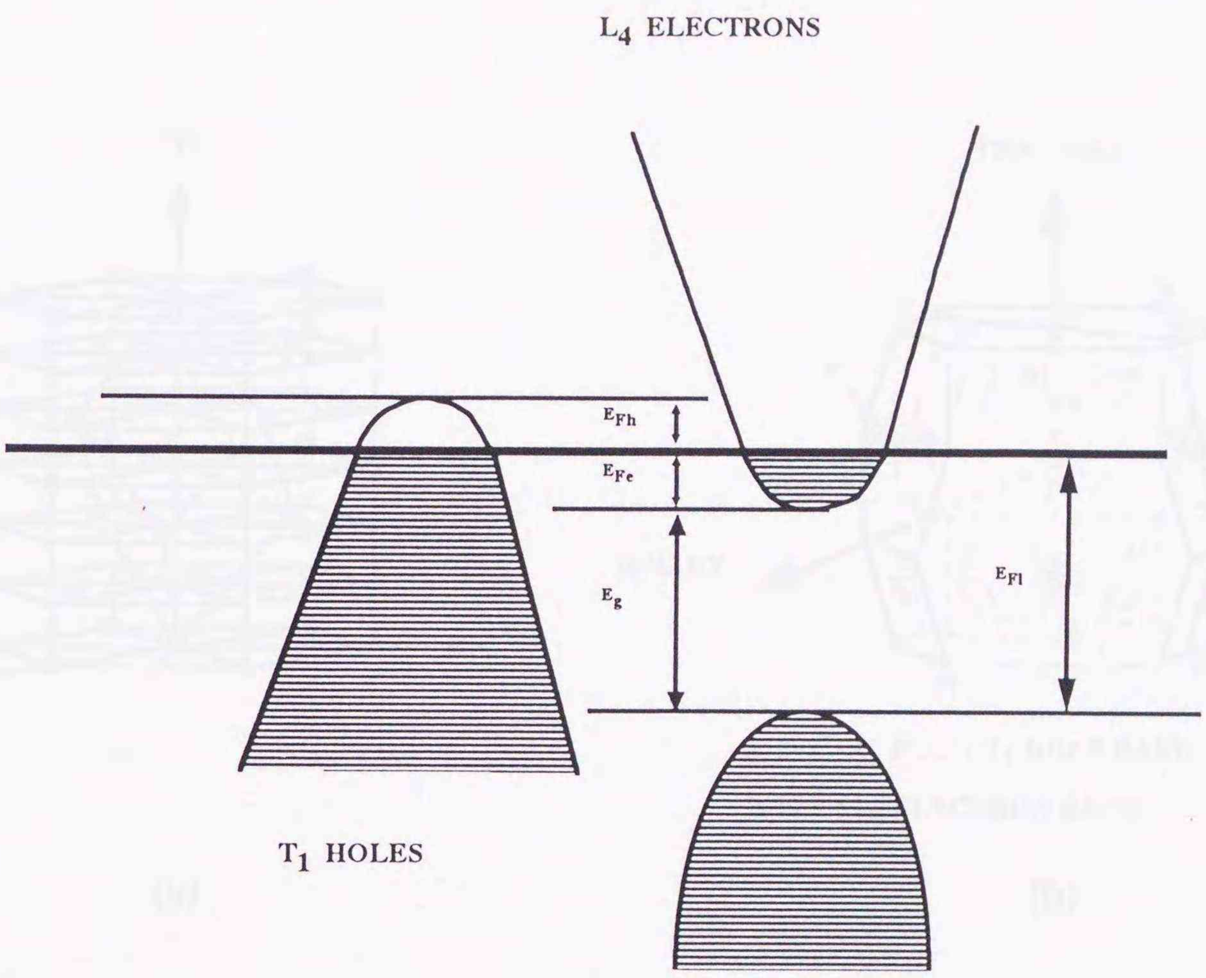

Figure 7: The band structure of antimony at 0 K. Here, E_{Fe}, E_{Fh}, and E_{Fl} are the Fermi energies of electrons, heavy holes, and light holes, respectively, while, E_g is the direct energy gap.

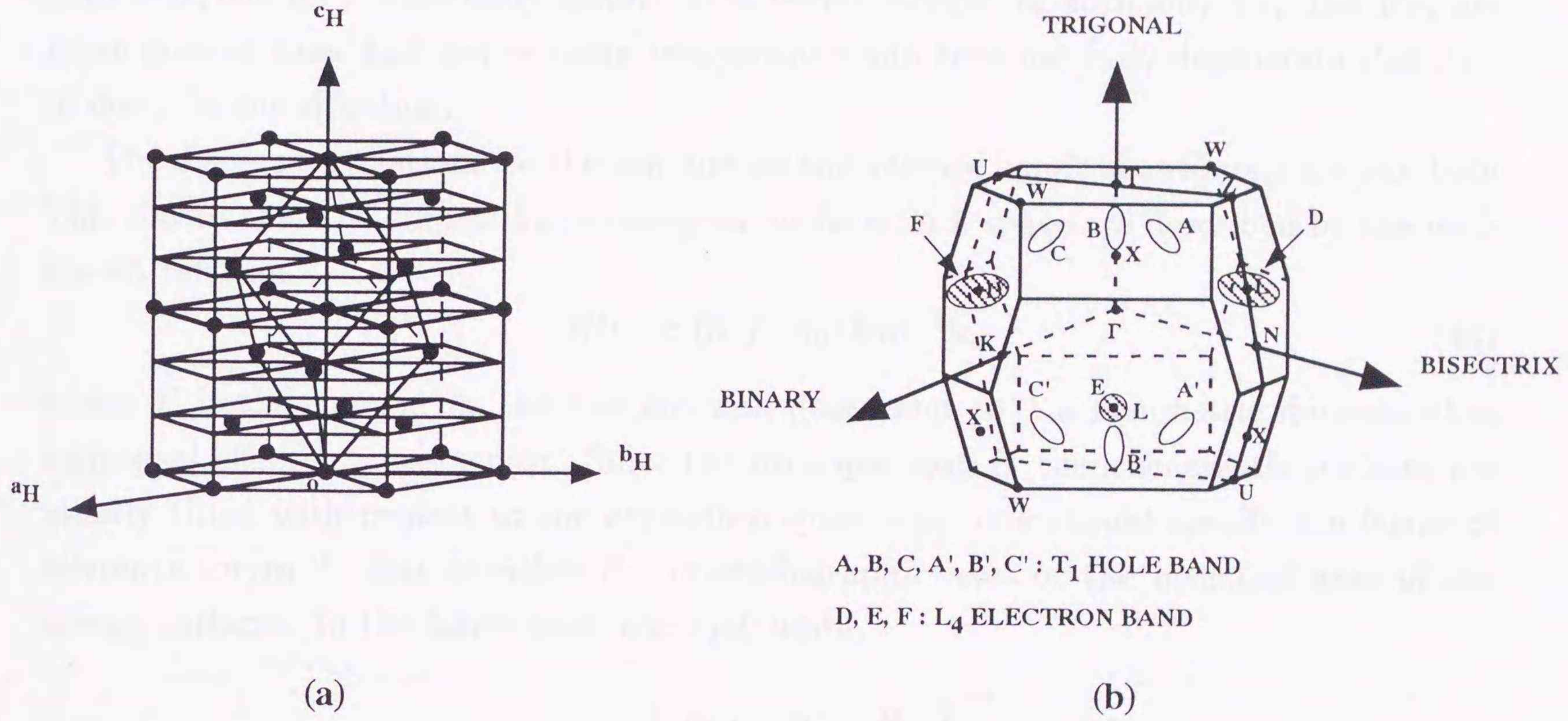

Figure 8: (a) Hexagonal representation of the A_7 structure. The basal planes aare perpendicular to the trigonal axis c_H. (b) The first Brillouin zone of antimony showing symmetry points.

Table 1. Band parameters for carriers in antimony at liquid helium temperatures. Of the parameters listed, ϕ_e and ϕ_h are the tilt angles of the electron and hole ellipsoids respectively, N_v is the number of valleys in the Fermi surface. $m_{1'}, m_{2'}, m_{3'}$ are expressed in units of m_0.

carrier type	$m_{1'}$	$m_{2'}$	$m_{3'}$	$\phi_e(2 \to 2')$ (deg)	$\phi_h(3 \to 2')$ (deg)	E_F (meV)	$n = p$ ($\times 10^{19}\text{cm}^{-3}$)	N_v
electrons	0.093	1.14	0.088	- 4	-	93.1	5.45	3
holes	0.068	0.92	0.050	-	53	84.4	5.45	6

One important thing to take into account in the study of semimetals is the relative magnitude of $k_B T$ with respect to E_{Fe} and E_{Fh}, the Fermi energies for electrons and holes, respectively. This will determinate the degree of degeneracy of the carrier statistics. For antimony, one may reasonably assume that Fermi energies of antimony E_{Fe} and E_{Fh} are much greater than $k_B T$ below room temperature and thus use fully degenerate statistics to describe the situation.

The dispersion relations for the conduction and valence bands of antimony are parabolic. This means that the ellipsoidal isoenergetic surfaces in k space are described by the well-known relation

$$E(k) = (\hbar^2/2m_0)\, \mathrm{k}\mathrm{m}^{-1}\mathrm{k}, \tag{44}$$

where E is the energy, m_0 the free electron mass, and m^{-1} a symmetric dimensionless reciprocal effective mass tensor. Since the principal axes of the isoenergetic surfaces are usually tilted with respect to the crystallographic axes, one should specify the frame of reference for m^{-1}, that is either the crystallographic axes or the principal axes of the energy surfaces. In the latter case, one may write

$$\mathrm{m}^{-1} = \begin{bmatrix} m_{1'} & 0 & 0 \\ 0 & m_{2'} & 0 \\ 0 & 0 & m_{3'} \end{bmatrix}^{-1}, \tag{45}$$

where $m_{1'}, m_{2'}, m_{3'}$ are the components of the effective mass tensor expressed in units of m_0. In Table 1., the effective masses of antimony are given at 0 K.

As described in the previous section, it was realized by Sondheimer[129] that intravalley electron-phonon interactions in semimetals should be different from those in ordinary metals. Energy and momentum conservation requires that electrons interact with phonons of wave vectors $\mathrm{q} \leq 2\mathrm{k}_F$, where k_F is the Fermi wave vector. Since in momentum space the Debye sphere is much larger than the Fermi surface at high temperatures ($T > \theta_D$, where θ_D is the Debye temperature, 211 K for antimony), the electrons will interact with low energy phonons, as opposed to the thermal phonons of energy $k_B\theta_D$ which dominate the scene above θ_D. In fact, the important parameter here is not the Debye sphere, or the corresponding temperature θ_D, but instead an effective temperature for carrier-phonon interaction θ^*, which is given in (41). Because the Fermi surfaces are highly anisotropic in the degenerate region, so will be θ^*, and the interacting phonons will be entirely confined in an ellipsoid in momentum space, with semi-axes of twice the length of the semi-axes of the Fermi ellipsoid of the charge carriers with which they interact.

For the electron-phonon scattering in Sb, the scattering by the charge carriers is of the form[148] $\tau_c^{-1} = 6\tau_h^{-1} + 3\tau_e^{-1}$; τ_h^{-1} is the scattering relaxation frequency due to the hole carriers contained in one of the hole Fermi pockets and τ_e^{-1} corresponds to the electron carriers of an electron pocket. There are six hole pockets and three electron pockets in antimony which contribute independently to the scattering as long as the q's are small enough not to scatter carriers from one pocket to another (*intravalley scattering*). Under isotropic and quadratic energy distribution, the Fermi pockets of holes and electrons are spheres of radius k_e and k_h given by $k_e = (3\pi^2\frac{1}{3}n)^{1/3}$ and $k_h = (3\pi^2\frac{1}{6}n)^{1/3}$. With these values and with $v_x = 2.5\times10^5$ cm/sec[148], the different electronic parameters are $k_h = 6.4\times10^6$ cm^{-1}, $k_e = 8.1\times10^6$ cm^{-1}; $\Theta_h^* \simeq 24.4$ K, $\Theta_e^* \simeq 30.8$ K. Blewer *et al.* have measured the lattice thermal conductivity in antimony. They observed that the dramatic increase in the lattice thermal conductivity above 1.5 K was due to the predominant contribution of "peripheral" phonons ($q > 2k_F$). An effective scattering Debye temperature of $\Theta^* \simeq 25$ K they obtained, was close to the value calculated for Θ_h. The fact that the experimental points seem to span a spectrum of values of Θ ranging from about 20 to 30 K is in agreement with the qualitative considerations for the anisotropy of the pockets and the existence of two bands of charge carriers.

3 Experimental Techniques

> Jeder Satz, den ich schreibe, meint immer schon das Ganze, also immer wieder dasselbe und es sind gleichsam nur Ansichten eines Gegenstandes unter verschiedenen Winkeln betrachtet.
>
> L. W. Wittegenstein

3.1 Fabrication of Au-Sb_2Te_3-Al and Al-Al Oxide-Sb Tunnel junctions

The substrate used in this study is the micro cover glass (dimensions about 18 mm×32 mm×0.15 mm, MATSUNAMI GLASS IND., LTD). An adopted cleaning procedure involves washing the slides in a neutralizing solution of concentrated sodium hydroxide. After which the substrate is rinsed in a continuous flow of distilled water. The substrates are then cleaned by ethanol using an ultrasonic bath. The slides are then rinsing with ethanol and storing under ethanol ensuring that at all times the slides are immersed. Any handling of the slides is done with tweezers. Before use the slide is dried quickly using lint-free wiper (BEMCOTLABO, ASAHI KASEI), and then the slide is mounted in a substrate holder in the bell jar.

Prerequisite requirements for the vacuum evaporator are to prepare very clean surfaces and to keep them clean during their exposure to the vacuum system. First, ULVAC EBH-6 evaporator was used to fabricate junctions; however it was found[149] that the quality of inelastic electron tunneling spectra obtained was severe, which is due to oil contamination from the constituent pumps. A good choice is the British Edwards evaporator model AUTO 306, to which some modifications can be made to enable the fabrication of the tunnel junctions to proceed without exposing the junction to room atmosphere. Figure 9 illustrates the evaporator bell jar used in this study. These modifications are:

1. The installation of four position turret source which allows four different sources to be sequentially selected. Each source is selected by rotating an externally mounted control knob which drives via a rotary shaft seal and chain drive, the base plate mounted turret. The use of this accessory allows the build of tunnel junctions used in this study.

2. The introduction of the substrate holder which retains cove glass slides in a fixed position, i.e., about 15 cm directly above the filaments.

3. The introduction of a suitable masking system made from a thin aluminum sheet to allow the movement of evaporation masks while under vacuum.

4. The introduction of a radiation heater to heat the substrates up to 250 °C. As is described later, this heater allows to anneal as grown Sb_2Te_3 thin films at desired temperatures.

The vacuum system under this study consists of an *oil* diffusion pump (Model EO4/160K) which is backed by a standard 163 ℓ/min single stage rotary pump with an oil mist filter through a forline (activated alumina) trap. The vacuum system incorporates liquid nitrogen trap before the diffusion pump, together with Santovac 5 fluid in the diffusion pump. *The majority of organic contaminants to the films result from the diffusion pump oil.* For this reason Santovac 5 oil is used as it has a very high boiling point and hence a correspondingly low vapor pressure (10^{-9} Torr), and will produce a vacuum which is suitable for the growth of clean surfaces. In addition if films of Santovac 5 are accidently adsorbed onto the work chamber surface, they are easy to remove, since Santovac 5 only contains carbon, hydrogen,, and oxygen. It is interesting to note, that Santovac 5 has an unusually high thermal and oxidation stability, and although it may discolor with use it does not affect its operation. Also, it has little tendency to increase its viscosity, which means that there is less chance of overheating and thermal degradation.

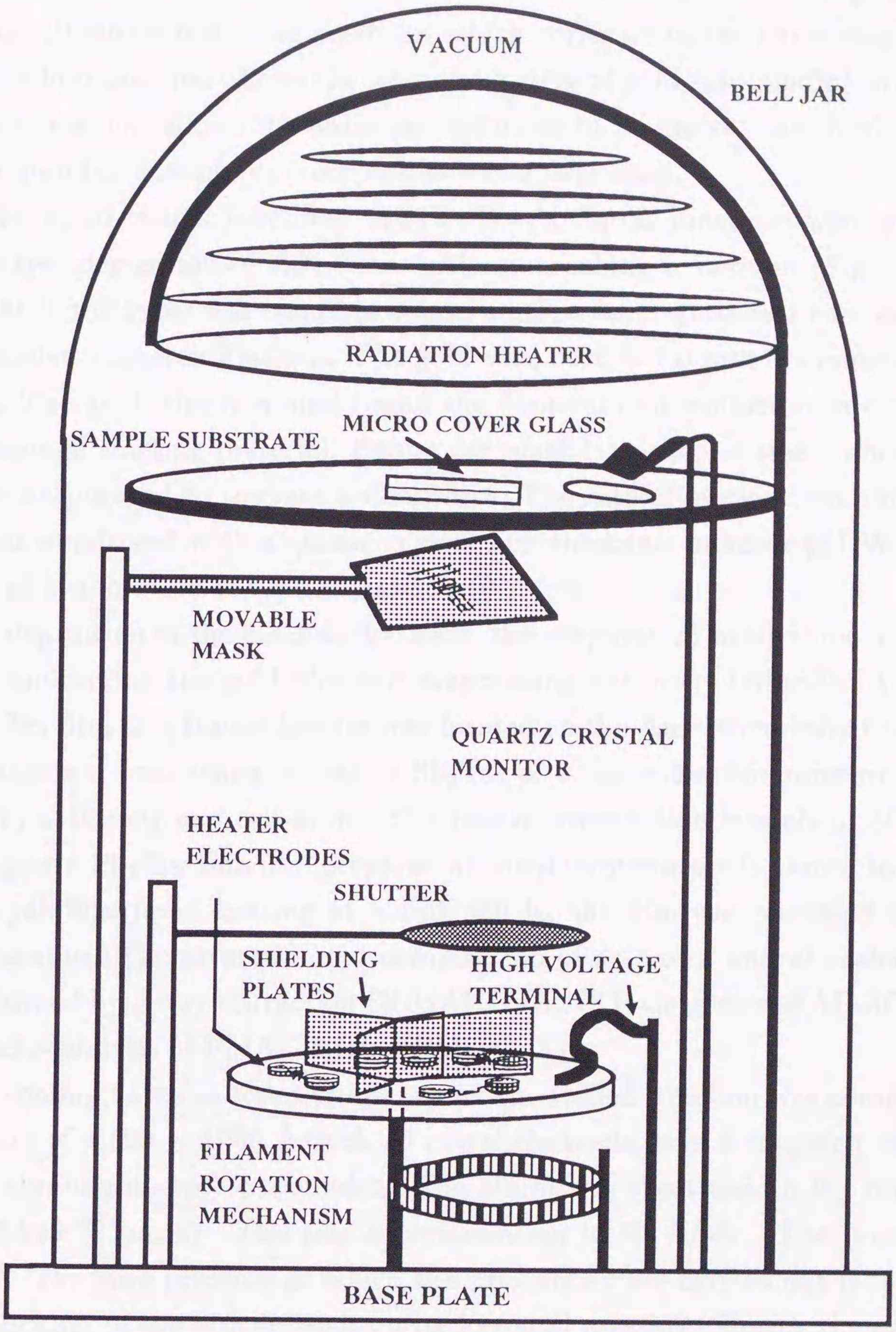

Figure 9: Evaporation bell jar.

The glass slide is placed in a sample holder in the evaporator bell jar, above a triple mask (Fig. 9) which has three positions which correlate to the three stages in the fabrication: the first position allows the lower long strip of gold (aluminum) to be evaporated; the second position allows the antimony telluride to be grown; the third position allows the aluminum (or antimony) cross-stripes to be deposited.

Au-Sb_2Te_3-Al tunnel junctions: Au-Sb_2Te_3-Al tunnel junctions were prepared by the layer-by-layer deposition of thin films without breaking a vacuum (Fig. 10 (a)) A gold film of 500 Å thickness was condensed onto a micro cover glass as a base electrode from a three stranded tungsten filament. The gold wire used is 1.0 mm in diameter and of 99.95 % purity. The gold wire is wound round the filament and doubled over on itself, so as to provide enough starting material. Before the mask is opened, a small amount of the gold should be evaporated to prepare a clean film. The rate of evaporation and the thickness of film was monitored with a quartz crystal film thickness monitor (EDWARDS FTM5). The rate of evaporation is typically about 10 Å/sec.

After deposition of the bottom electrode, the evaporation mask is moved to the second position, uncovering the gold film and evaporating antimony telluride. A 750 ~ 1150 Å thick Sb_2Te_3 film as a tunnel barrier was formed on the Au electrode by flash evaporation from a tantalum boat using pellets of Sb_2Te_3 of a stoichiometric mixture of high-purity (99.999 %) antimony and tellurium. The rate of evaporation was about 50 ~ 100 Å/sec. As an as-grown Sb_2Te_3 thin film prepared at room temperature is known to be amorphous and to crystallize upon heating at about 350 K, the film was annealed at 393 K for 1 hr in a vacuum. The structure and composition of as-grown and annealed Sb_2Te_3 films were confirmed by X-ray diffraction (RIGAKU DENKI: Geigerflex RAD-3C) and electron probe micro-analysis (EPMA, JEOL: JEM200CX).

After cooling down to room temperature, the tunnel junction was completed with the evaporation of a 500 ~ 1000 Å thick Al metal electrode from a tungsten wire on which 6 pieces of aluminum sheet is wounded. The aluminum sheet used is 0.1 mm in thickness and of 99.999 % purity. The rate of evaporation is 10 Å/sec. The junction area was 0.04 mm^2. The base pressure at which the procedures are carried out is fairly important since the quality of the film depends on background pressure. During the evaporation and annealing process the pressure was was lower than 5×10^{-7} Torr. Junctions prepared in this way had tunnel resistance in 400 - 800 Ω. The tunneling conductance was measured at 4.2 and 77 K. The resistances of good junctions were rapidly increased with decreasing temperatures and the parabolic characteristics were observed in a wide bias region at both 4.2 and 77 K.

Al-Al oxide-Sb tunnel junctions: Antimony has both covalent and metallic characters, and therefore the crystallite orientation of the films can be considered to be strongly

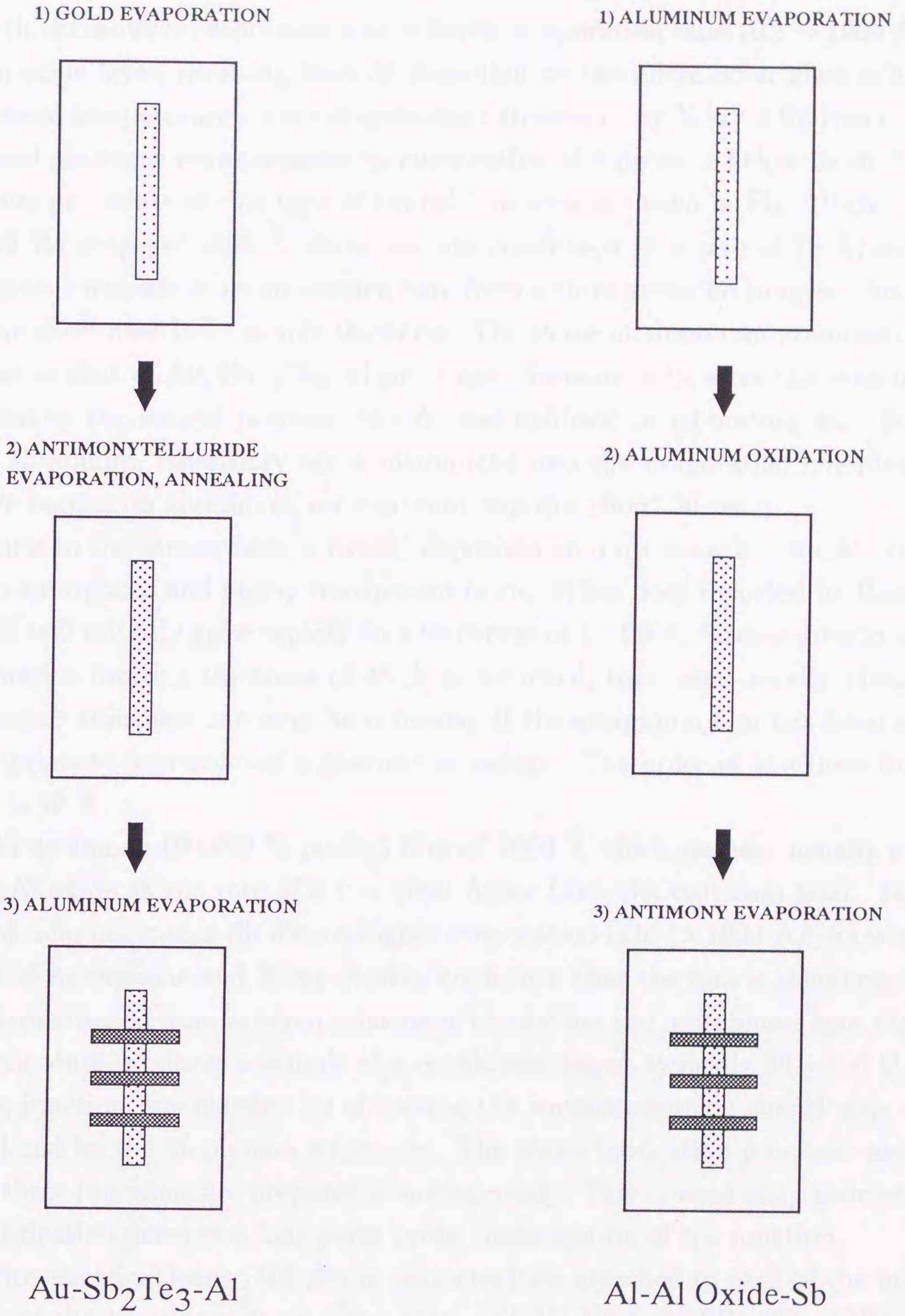

Figure 10: A schematic view of the steps involved in making crossed film junctions used in this study.

affected by the evaporation rate. Therefore, as preliminary experiments, antimony films of 1000 Å in thickness were evaporated with different evaporation rates (0.1 $\sim$ 1000 Å/sec) on aluminum oxide layer, resulting from Al deposited on the micro cover glass substrate and kept at room temperature, to investigate their structures by X-ray diffraction. Al-Al oxide-Sb tunnel junctions were prepared by evaporation at a pressure below 2×10^{-6} Torr. The fabrication procedure of this type of tunnel junctions is shown in Fig. 10 (b). First, an Al (99.999 %) stripe of 1000 Å thickness was condensed at a rate of 10 Å/sec on a micro cover glass substrate at room temperature from a three stranded tungsten filament. The aluminum sheet used is 0.1 mm in thickness. The shape of aluminum wounded on the wire is similar to that of Au-$Sb_{1-x}Te_x$-Al junctions. Subsequently, after the evaporation mask is moved to the second position, the Al was oxidized in laboratory air. For the oxidation of aluminum, laboratory air is introduced into the evaporation chamber. To grow an oxide barrier on aluminum, air exposure requires about 30 sec.

On exposure to the atmosphere, a freshly deposited aluminum surface would immediately form an amorphous and highly transparent oxide. It has been reported by Hass[150] that the oxide will initially grow rapidly to a thickness of 15–20 Å; further growth occurring slowly until a limiting thickness of 45 Å is achieved, this takes usually about one month. A greater thickness can only be achieved, if the aluminum film has been slowly deposited to promote formation of a granular structure. The order of thickness for this type of layer is 90 Å.

Finally, an antimony (99.999 % purity) film of 1000 Å thickness was usually evaporated on the Al oxide at the rate of 0.1 $\sim$ 1000 Å/sec from the tantalum boat. For the preparation of inhomogeneous Sb films a higher evaporation rate ($>$ 1000 Å/sec) was crucial. An optical microscope and X-ray studies confirmed that the film is inhomogeneous and that it is constituted from random mixture of crystalline and amorphous spot regions. The above procedure produces a sample of a usable resistance, typically 50 – 200 Ω. The quality of the junction was checked by observing the superconducting energy gap structure of the Al and by the Sb phonon structures. The above fabrication processes are such that a set of three junctions are prepared simultaneously. This crossed strip geometry, of the tunnel fabrication permits a four-point probe investigation of the junction.

Copper wire electrical leads (500 μm in diameter) are attached to each of the bottom and top films of the junctions, using silver paste (FUJIKURA KASEI CO., LTD). The other sides of wires are attached to the plugs on the sample holder.

3.2 Junction Evaluation

Once the junction fabrication is complete, the tunneling experiment should be carried out as soon as possible in order to avoid deterioration of the junction particularly after it has been removed from the vacuum system. The junction can usually be preserved indefinitely at liquid nitrogen temperature, but frequent thermal cycling may destroy it. After fabricating junctions with a resistance suitable for measurement it is important to examine them closely before time and effort is expended in taking and interpreting detailed derivative plots. Junctions should therefore satisfy the following criteria[151, 152, 153].

1. Junctions of different areas can be evaporated simultaneously. Upon cooling to liquid nitrogen temperature, the junction resistance should be proportional to area within ± 20 %.

2. When the junction is cooled to liquid helium temperature, its resistance should increase only slightly.

3. At 1 K, when one electrode is in the superconducting phase, the conductance at zero bias should be 10^{-3} of the conductance observed when the superconductivity is quenched by application of a magnetic field. And below the critical temperature T_c, an energy gap structure should be also observable in a good junction.

4. If both electrodes are in the superconducting phase, then the cusp in the $I-V$ characteristic at $(\Delta_2-\Delta_1)$ should be quite sharp and the negative resistance region from $(\Delta_2-\Delta_1)$ to $(\Delta_1+\Delta_2)$ should be well defined.

5. For junctions with electrodes in the normal state, the conductance should follow a parabolic dependence on voltage. This is a reasonably good test of tunneling and can also test a junction to fairly high voltage as compared to the superconducting characteristics, which are observed only at low voltages.

6. Structure in the second derivative curves due to phonon excitation in the electrodes and the barrier should also be observable in a good tunnel junction. For example, junctions of the type Al-AlO$_x$-M should show a strong peak at 120 meV, which has been identified with the OH bending mode in aluminum hydrate.

7. One expects for tunneling voltage $V \rightarrow 0$,

   $$G(T) = G(0)\,\frac{\pi C_{10} k_B T}{\sin\left(\pi C_{10} k_B T\right)}$$

   with C_{10} as a parameter characterizing the tunneling barrier.

8. If the lead electrodes are used and in the superconducting states, the $I-V$ characteristic exhibits a tunneling structure corresponding to the superconducting energy gap of lead. We define the junction quality in terms of $Q = 100\left[1-\left(I_0 - I_{BCS}\right)/I_{nn}\right]$[154], where I_0 and I_{BCS} are the measured and the theoretically predicted values of the

junction current, respectively, at 1 mV and T=1.8 K. I_{nn} is the current at V=1 mV in the normal state of lead. We require the quality Q larger than 85 %.

9. If superconducting electrode is in the normal state, the tunneling characteristics do not depend on the magnetic field above the superconducting critical field of the material.

The quality of Au-Sb_2Te_3-Al and Al-Al Oxide-Sb tunnel junctions was verified by the above criteria (2), (5), and (2), (3), (5), (6), respectively.

3.3 Measurement Cryostat

The sample holder and a stainless steel tubular probe used in this study, are shown in Figs. 11 (a) and (b), respectively. The samples prepared are mounted in the sample holder, which constitutes of a modified printed circuit board[155] with terminal spacing of 15 mm. The sample holder is designed to fit down the the liquid helium storage dewer with an internal neck diameter of 36 mm. Three junctions are connected with the sample holder by eight small screw clamps. Electrical connections to the tubular probe (approximately, 1 m long) are made via modified IC connectors. The modification of the IC connectors is achieved by the careful removal of surplus plastic and by bending the connected pins. Such an arrangement provides a convenient and effective cryostat for work at 4.2 K. The use of modified IC connectors provide a holder which is very easy to use and makes the technique of tunneling spectroscopy much more convenient for routine analysis work by facilitating rapid four-terminal measurements on each of three junctions. Indeed, the use of this holder reduces the time during which junctions are exposed to room air to about 10 mins. BNC connectors for coaxial cables for tunneling and temperature measurements are equipped with the top flange of the tubular probe.

3.4 Derivative Measurement Circuit

The use of tunneling spectroscopy to probe the physics of solids is facilitated by the derivative techniques. Singular points at energy gap edges, various elementary excitations, or other threshold behaviors are manifested by a break in slope of the $I-V$ characteristic of the junction. Since the additional current is often slight to the point of invisibility, derivatives of the $I-V$ curve are taken to enhance observation of the threshold voltage. In the study of tunneling behavior there are three characteristics that are measured in order to obtain information on the fundamental tunneling process. There are: (1) I versus V, (2) the tunneling derivative conductance $\mathrm{d}I/\mathrm{d}V$ versus V, and (3) the derivative of the conductance (tunneling derivative spectra) $\mathrm{d}^2I/\mathrm{d}V^2$ versus V. The purpose of the present section is to describe measurement technique to obtain the $\mathrm{d}V/\mathrm{d}I$ and $\mathrm{d}^2V/\mathrm{d}I^2$.

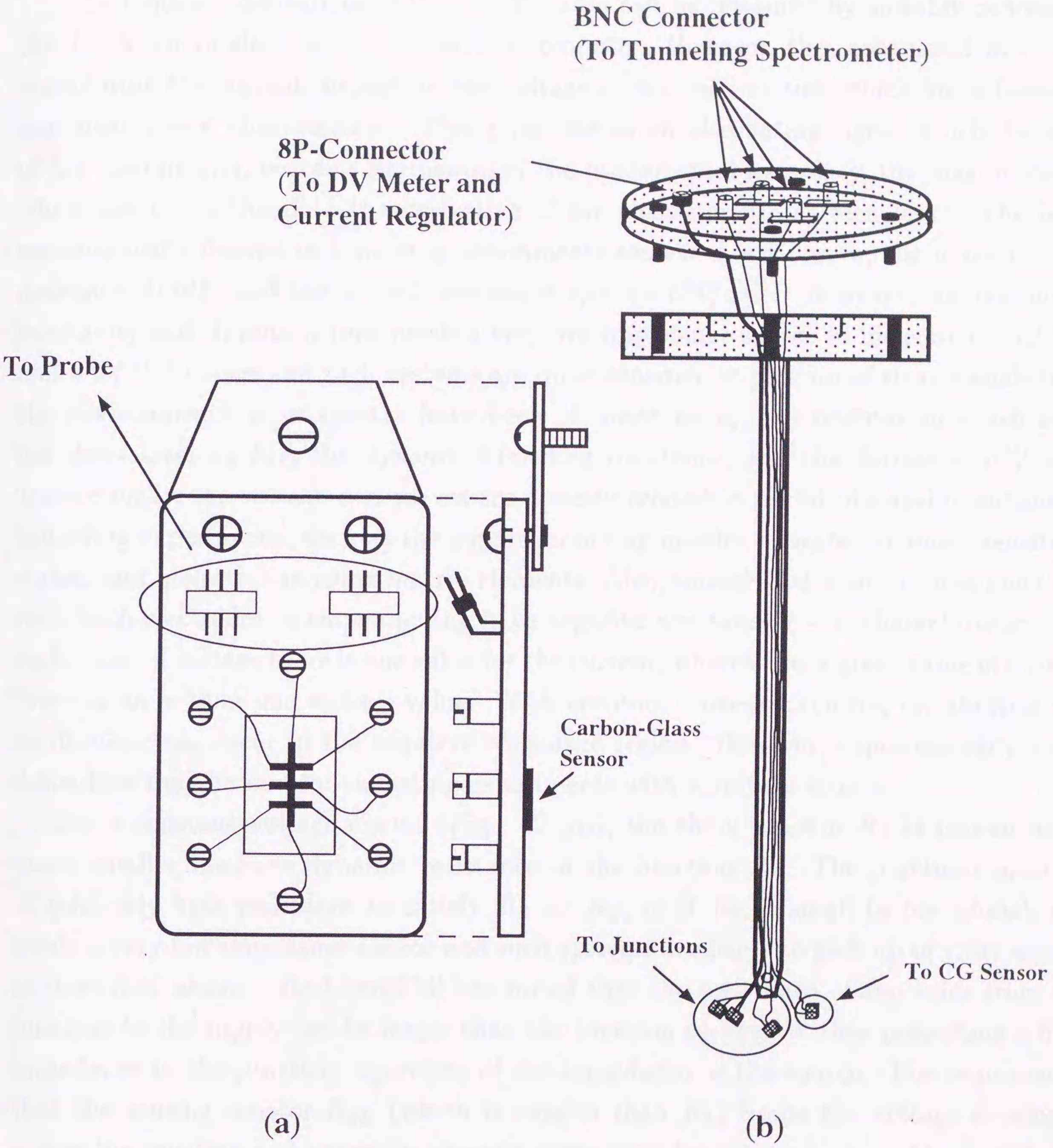

Figure 11: (a) A sample holder and (b) a tubular probe.

3.4.1 Modulation Technique

The requisite derivatives of the $I - V$ curve can be obtained by suitably processing the $I - V$ curve electronically or with a computer. However, the more usual way is by modulating the current through or the voltage across the junction which has a (weakly) nonlinear $I - V$ characteristic. This gives rise to an alternating signal which, because of the nonlinearity, contains harmonics of the fundamental frequency, the magnitudes of which are proportional to the derivative of the characteristic as seen later. The basic measurements desired in tunneling experiments are the $I - V$ curve, the dynamic conductance $\mathrm{d}I/\mathrm{d}V$ and the second derivative spectra $\mathrm{d}^2I/\mathrm{d}V^2$. However, for reasons of sensitivity and simplicity (one needs a very low impedance source to measure the $\mathrm{d}I/\mathrm{d}V$ and $\mathrm{d}^2I/\mathrm{d}V^2$ curves and such systems are quite sensitive to pick up of stray signals from the environment), most spectra have been obtained using instrumentation which gives the derivatives $\mathrm{d}V/\mathrm{d}I$, the dynamic tunneling resistance, and the derivative $\mathrm{d}^2V/\mathrm{d}I^2$. Theoretically, the voltage derivatives are directly related to useful physical quantities in tunneling experiments, such as the superconducting density of states, phonon density of states, and inelastic tunneling matrix elements. Also, tunnel diodes and tunnel junctions with both electrodes superconducting have negative resistance $I - V$ characteristics. For each value of voltage there is one value for the current, whereas for a given value of current there is more than one voltage value. With constant current circuitry, instabilities and oscillations can occur in the negative resistance region. However, experimentally, some difficulties may be met for tunneling experiments with a voltage source.

For a constant voltage circuit (Fig. 12 (a)), the shunt resistor R_S is chosen to be much smaller than the dynamic resistance of the junction R_T. The junctions must be of relatively high resistance to satisfy $R_S \ll R_T$, or if R_T is small (a few ohms), one needs a very low impedance source and such systems are likely to pick up of stray signals as described above. Blackford[156] has noted that the resistance of the leads from the junction to the supply can be larger than the junction resistance, thus presenting a high impedance to the junction regardless of the impedance of the source. The requirement that the sensing resistor R_{SE} (which is smaller than R_T) limits the voltage developed across the junction and generally presents some impedance matching problems with the signal processing circuitry. These reasons probably account for the fact that current source types have been more widely used. When it is desired to measure $\mathrm{d}I/\mathrm{d}V$ or $\mathrm{d}^2I/\mathrm{d}V^2$, the commonly used procedure is not to measure these quantities directly but rather to measure the $\mathrm{d}V/\mathrm{d}I$ and its derivative $\mathrm{d}^2V/\mathrm{d}I^2$, and then use these values to calculate $\mathrm{d}I/\mathrm{d}V$ or $\mathrm{d}^2I/\mathrm{d}V^2$. The derivatives are related by the identities $\mathrm{d}I/\mathrm{d}V = 1/(\mathrm{d}V/\mathrm{d}I) = 1/\mathrm{G}$ and $\mathrm{d}^2I/\mathrm{d}V^2 = -G^3\mathrm{d}^2V/\mathrm{d}I^2$ *. The method of measuring $\mathrm{d}I/\mathrm{d}V$ or $\mathrm{d}^2I/\mathrm{d}V^2$ suffers from the

---

*$\mathrm{d}^2I\,/\mathrm{d}\,V^2 = (\mathrm{d}/\mathrm{d}V)(\mathrm{d}I/\mathrm{d}V) = (\mathrm{d}I\,/\mathrm{d}V)(\mathrm{d}/\mathrm{d}I)[1/(\mathrm{d}V/\mathrm{d}I)] = -\,\mathrm{G}^3(\mathrm{d}^2V/\mathrm{d}I^2)$.

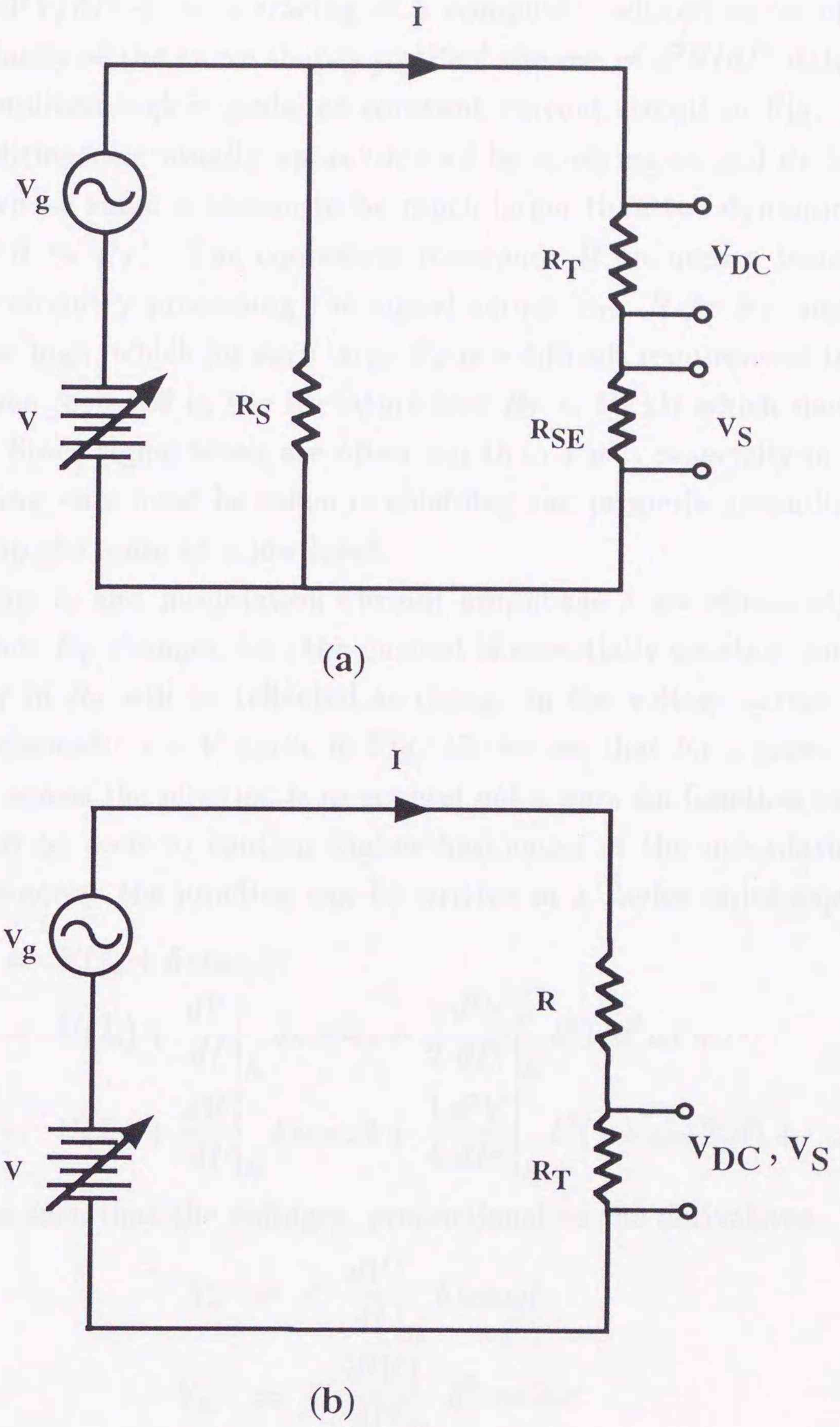

Figure 12: Simplified (a) constant voltage and (b) constant current circuits.

fact that it is less sensitive than a measurement of $\mathrm{d}V/\mathrm{d}I$ and $\mathrm{d}^2V/\mathrm{d}I^2$. Since both $\mathrm{d}V/\mathrm{d}I$ and $\mathrm{d}^2V/\mathrm{d}I^2$ can be obtained, the inversion to G and $\mathrm{d}G/\mathrm{d}V$ can be obtained using ratio or computer techniques. Jennings and Merrill[157] made a comparison of a tracing of original data for $\mathrm{d}^2V/\mathrm{d}I^2$–$V$ to a tracing of a computer reduced curve of $\mathrm{d}^2I/\mathrm{d}V^2$–$V$. The striking similarity of the curve shapes justified the use of $\mathrm{d}^2V/\mathrm{d}I^2$ data.

Consider a simplified high-impedance constant current circuit in Fig. 12 (b). Constant current conditions are usually approximated by applying ac and dc biases through series resistor R whose value is chosen to be much larger than the dynamic resistance of the junction R_T ($R \gg R_T$). The equivalent resistance R includes a term representing the impedance of circuitry processing the signal across R_T. $R \gg R_T$ implies that this impedance must be high, which for very large R_T is a difficult requirement to fulfill. However, most junctions reported in the literature had $R_T < 10$ kΩ which does not present much of problem. Since signal levels are often less than 1 μV, especially in the detection of inelastic tunneling, care must be taken in shielding and properly grounding the system components to keep the noise at a low level.

The bias current I_0 and modulation current amplitude δ are effectively constant as the tunnel resistance R_T changes, i.e., the current is essentially constant and determined by R. The change in R_T will be reflected as change in the voltage across the junction. Referring to the schematic $I - V$ curve in Fig. 13, we see that for a given I_0 and δ, the voltage developed across the junction is in general not a *pure* sin function but, on Fourier decomposition, can be seen to contain higher harmonics of the modulation frequency, $\omega/2\pi$. The voltage across the junction can be written in a Tayler series expansion as

$$\begin{aligned} V(I) &= V(I_0 + \delta\cos\omega t) \\ &= V(I_0) + \left.\frac{dV}{dI}\right|_{I_0} \delta\cos\omega t + \left.\frac{1}{2}\frac{d^2V}{dI^2}\right|_{I_0} \delta^2\cos^2\omega t + \cdots \\ &= V(I_0) + \left.\frac{dV}{dI}\right|_{I_0} \delta\cos\omega t + \left.\frac{1}{4}\frac{d^2V}{dI^2}\right|_{I_0} \delta^2(1+\cos 2\omega t) + \cdots . \end{aligned} \tag{46}$$

From this it can be seen that the voltages, proportional to the derivatives,

$$V_\omega = C\left.\frac{dV}{dI}\right|_{I_0} \delta\cos\omega t \tag{47}$$

$$V_{2\omega} = C\left.\frac{d^2V}{dI^2}\right|_{I_0} \delta^2\cos 2\omega t \tag{48}$$

are available across the junction and can be obtained using a lock-in amplifier. As is obvious from (48), the second harmonic term can be detected by the lock-in amplifier at the reduced signal levels for smaller modulation current amplitude.

The broadening at the singular points in the tunneling conductance, or the line width broadening in the second derivatives is determined by thermal broadening, modulation

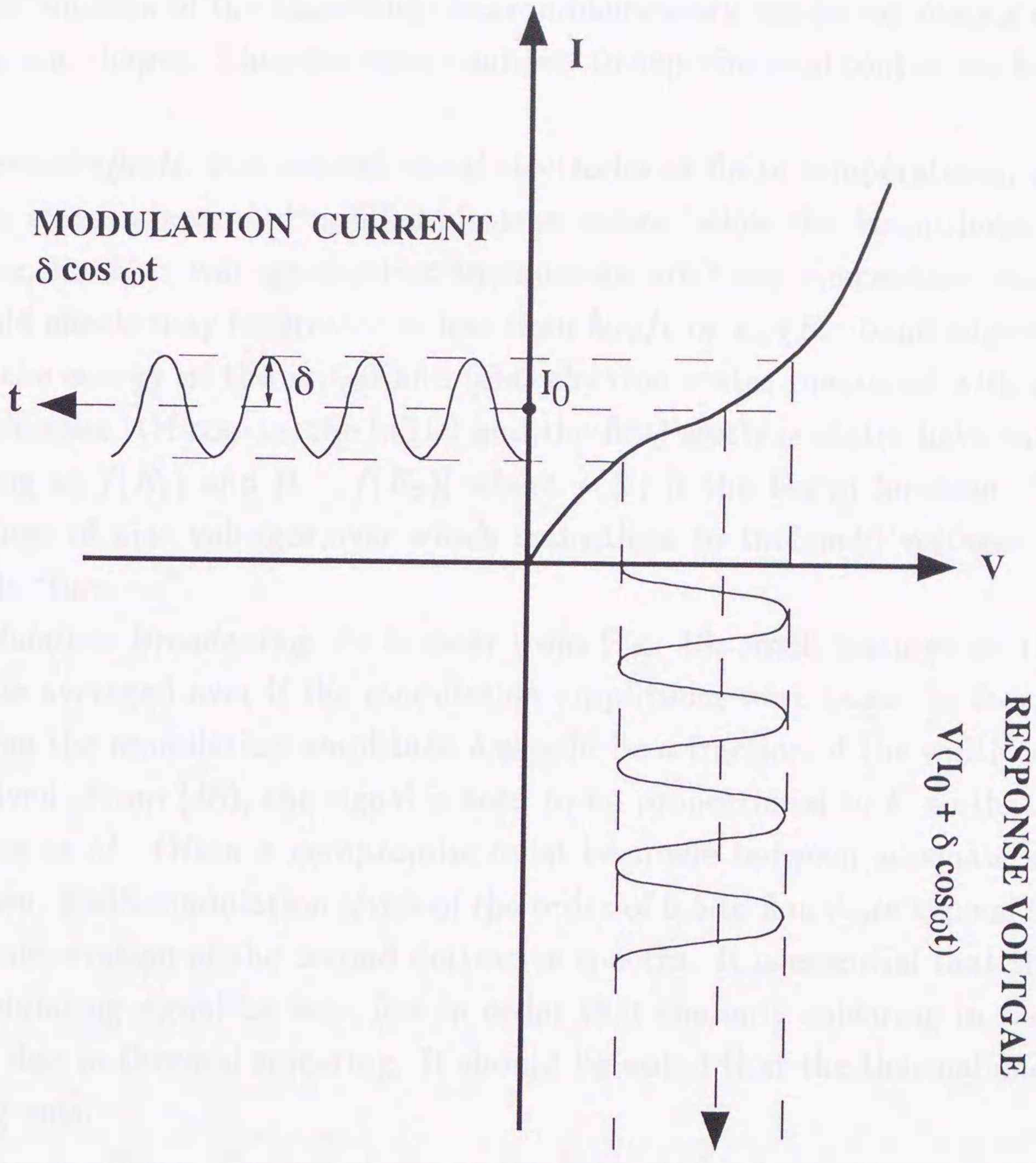

Figure 13: Explanation of modulation technique for measurements of the first- and second derivative curves in $I-V$ characteristics.

broadening, electrode (density of states) effects, and natural width (life time) of various excitations[158]. No analytic expression is available for this natural width since it is a complex function of the tunneling electron-elementary excitation matrix element, barrier heights, and shapes. Thus the effects subject to experimental control are focused attention on.

Thermal effects: For normal metal electrodes at finite temperatures, there exist filled electron states above and unfilled electron states below the Fermi level E_F. As a consequence, the bias voltage required to cause an arbitrary elementary excitation or other threshold effects may be greater or less than $\hbar\omega_0/e$ or E_c (E_c: band edge energy) depending on the energy of the initial and final electron states measured with respect to their Fermi energies. Of course, the initial and the final electron states have values distributed according to $f(E_1)$ and $[1-f(E_2)]$ where $f(E)$ is the Fermi function. Thus there will be a range of bias voltages over which transitions to threshold voltages or the inelastic channels "turn on".

Modulation Broadening: As is clear from Fig. 13, small features on the $I-V$ curve would be averaged over if the modulation amplitudes were large. In fact, for reasonable resolution the modulation amplitude δ should be a fraction of the width of the feature to be resolved. From (48), the signal is seen to be proportional to δ^2 so that signal to noise decreases as δ^2. Often a compromise must be made between adequate signal and high resolution. RMS modulation levels of the order of 0.5 to 2 mV are typical in the literature for the observation of the second derivative spectra. It is essential that the amplitude of the modulating signal be kept low in order that the only smearing in the characteristic be that due to thermal smearing. It should be noted that the thermal energy kT at 1 K is 86 μV rms.

Electrode effects: The use of one or the both electrodes provide a number of benefits. To determine whether the transport mechanism of electrons carried by the junction is tunneling (as opposed to that carried by shorts or bridges between electrodes) one looks at the $I-V$ or derivatives - V curves near zero bias. The sudden rise in current at $V=\Delta/e$ results in a strong structure in $\mathrm{d}I/\mathrm{d}V$. Similarly, $\mathrm{d}^2I/\mathrm{d}V^2$ has an intense feature at Δ/e rising from the onset of tunneling. Second the resolution is improved due to a significant reduction in the thermal smearing at the Fermi level. The number of electrons thermally excited across the gap is governed by the Fermi distribution which, in the tail, is (roughly) the Boltzmann distribution $e^{-(E+\Delta)/kT}$ where E is the electron energy. At 1 K Δ may be 10 to 20 times kT, so that effectively there is a sharp boundary in energy between filled and unfilled states. One can say crudely that the gap cuts off the tail of the Fermi function. There is a second effect of importance and that is superconducting density of states N_S at the gap is very large and sharp as given by $N_S = N_N\,|E|\,/(E^2-\Delta^2)^{1/2}$. N_N

is the normal state density. Since the number of states in a very small energy range at the gap edge is so very large for $E \sim \Delta$, tunneling into these states dominates and results in a very sharp second derivative shape. Note that there is also change in line shape with the drop following the sharp peak. Thus, when the electrodes are superconductivity, the onset of the inelastic current occurs over a much narrower range than for normal electrodes. Giaever *et al.*[159] have reported an increase in resolution by a factor of 5 in going from normal to superconducting electrodes. For Sn-Sn oxide-Sn junction measured at 0.3 K the width of the onset was 0.003 meV which is to be compared to 0.15 meV with electrodes normal.

3.4.2 Filter Network Type Tunneling Spectrometer

This section describes a rejection-selection filter network tunneling spectrometer used in this study in detail, including some details of the design of the circuit, its performance, and the construction of its essential.

A rejection-selection filter network type tunneling spectrometer has originally been used by Thomas and Rowell[160] for solving the problem of measuring specifically the superconducting second derivative, at high resolution. A clever alternative strategy due to Thomas and Rowell is to build passive resonant circuits to assist in the selection and amplification of the required signal. The Thomas-Rowell circuit contains two meshes: an input mesh feeds the fundamental signal ω to the junction and simultaneously suppresses the transmission of any second-harmonic content from the source, while the second mesh also transforms the impedance level from the low value of the junction to the high value of the preamplifier input. A great merit of this approach is that sufficient gain may be achieved, before the signal enters the active amplifier circuitry to reduce noise insignificant in the detection process. The present design draws on the Thomas-Rowell idea but in combination with high-impedance elements in some parts of the circuit, and furthermore with a computer data acquisition system. In practice the circuit turns out to be robust in so far as it may be operated successfully in quite noisy environments and the quality of the spectra is not significantly degraded when the circuit is interfaced to a desktop-computer-control data acquisition system. Also it is sensitive enough to be used with the very low modulations (~100 μV peak to peak) which are essential when detailed spectral line shapes and width are being studied at helium temperatures.

Circuit Description: The circuit applies a 50 kHz modulation current to the tunnel junction in parallel with DC bias which is slowly swept during the taking of a spectrum. The choice of 50 kHz as the fundamental frequency, with detection at 50 or 100 kHz, follows Lambe and Jaklevic[40], who noted qualitatively that junction noise falls off with increasing frequency, while frequencies above about 100 kHz lead to capacitive currents which cause increasing difficulty. The 100 kHz range is also optimum from the point of view of noise figures in typical amplifiers. The DC bias is monitored on the digital voltmeter (HP-3478A) and from there is fed to a microcomputer (NEC PC9801RA) and stored while the amplitude of the ac voltage signal appearing across the junction at 50 or 100 kHz is fed through a preamplifier and lock-in amplifier to the same microcomputer and stored on it.

A complete circuit used in tunneling spectrometer is shown in Fig. 14. In order to minimize ground loop problem, a modified DC bias sweep circuit as in Fig. 15, which Rogers originally designed[161], is used as the source of the DC bias current. This circuit can change sweep time in a wide range by selecting R and C. A fine adjustment of sweep time can be performed with 50 kΩ potentiometer. 470 μF×2 capacitors are inserted at the final output of operational amplifier (BURR-BROWN, OPA111) to reject higher frequency noise. The circuit provides the sweep and, depending on the resistance of the sample, an appropriate range-limiting resistor is selected with a 12-way rotary wafer switch. Typically, if a sample has resistance R, a series resistor of $75R$ would be chosen to provide a sweep out in the desired bias voltage region. In practice, the sample resistances are not exactly controllable so it will be purely fortuitous if exactly the ideal value for the series resistor is available. Instead a slightly lower value will usually be used. Under normal operating conditions, the AC current applied in parallel with the DC sweep is first adjusted to give a few mV peak to peak modulation across the junction with the DC bias held in the region of a few tens to 100 mV. The modulation is monitored on a screened floating input to a sensitive (YEW MODEL 3663) oscilloscope during adjustment but the oscilloscope is disconnected once the amplitude has been set. When a small amplitude of AC current (~100 μV) is applied across the junction, a preamplifier must be inserted before the oscilloscope. The input 50 kHz AC current is filtered by a 100 kHz parallel resonant LC circuit on one input line and a 50 kHz parallel resonant LC circuit across the two input lines. In addition, a 10 kΩ resistor at the oscillator output protects against overloading (harmonic) distortion of the oscillator at resonance. Another 10 kΩ resistor between the filters and the sample acts as a potential divider and thereby allows the filters to be driven at a high enough power level to make pick-up signals relatively insignificant. The implication of this arrangement is that the oscillator itself should have a fairly high output; the NF MODEL FG121B in this spectrometer has a maximum output of 10 V peak to peak though full output is not normally necessary. The pickup of airborne signals (including 60 Hz magnetic signals) by the ferrite cores of these filters is simply but effectively dealt with by maintaining a high-level signal from the oscillator into the filters sufficient to dwarf pickup signals, followed by a pick-up-free resistive potential divider to reduce the level to that appropriate for the junction modulation. The remaining

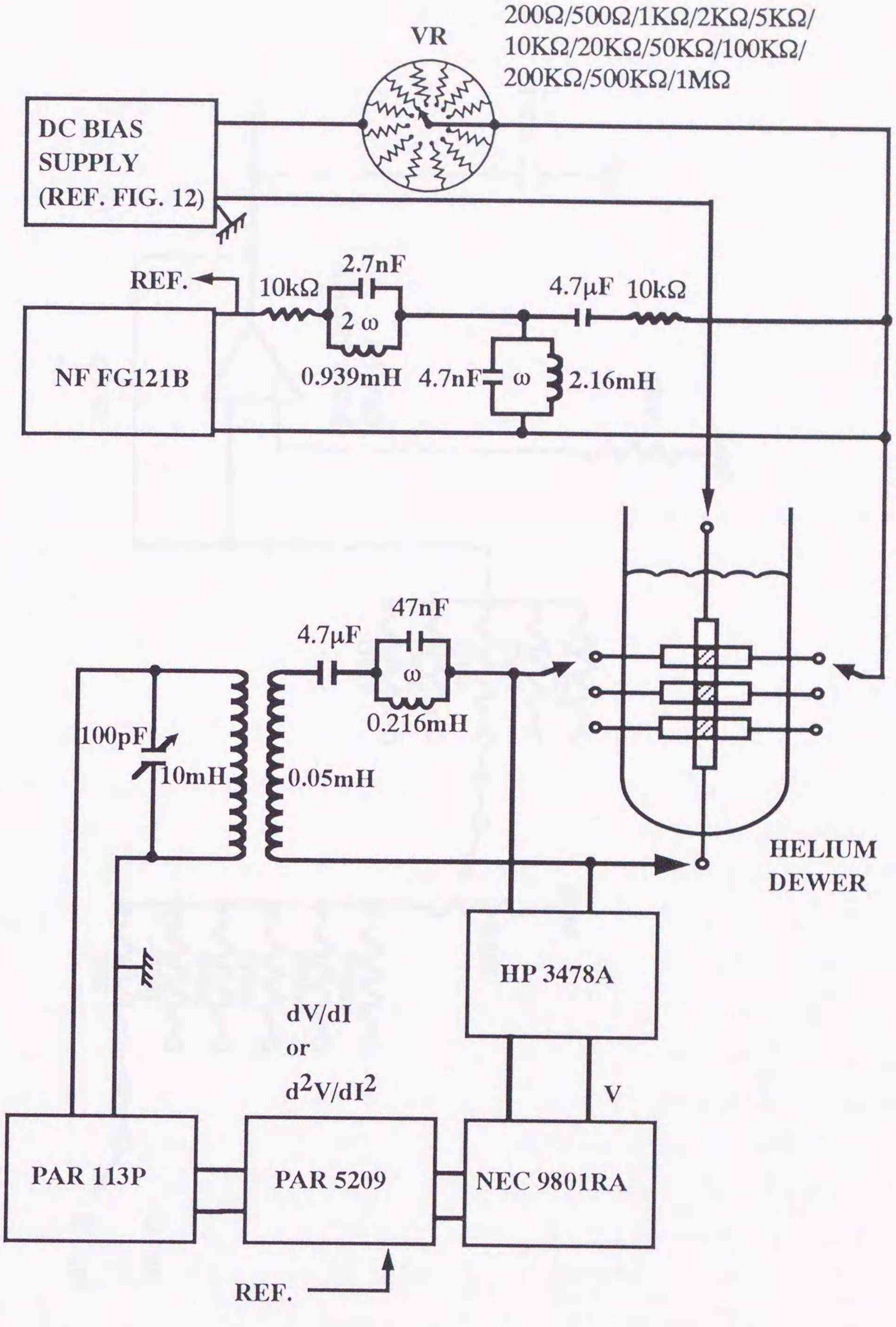

Figure 14: Filter network tunneling spectrometer system.

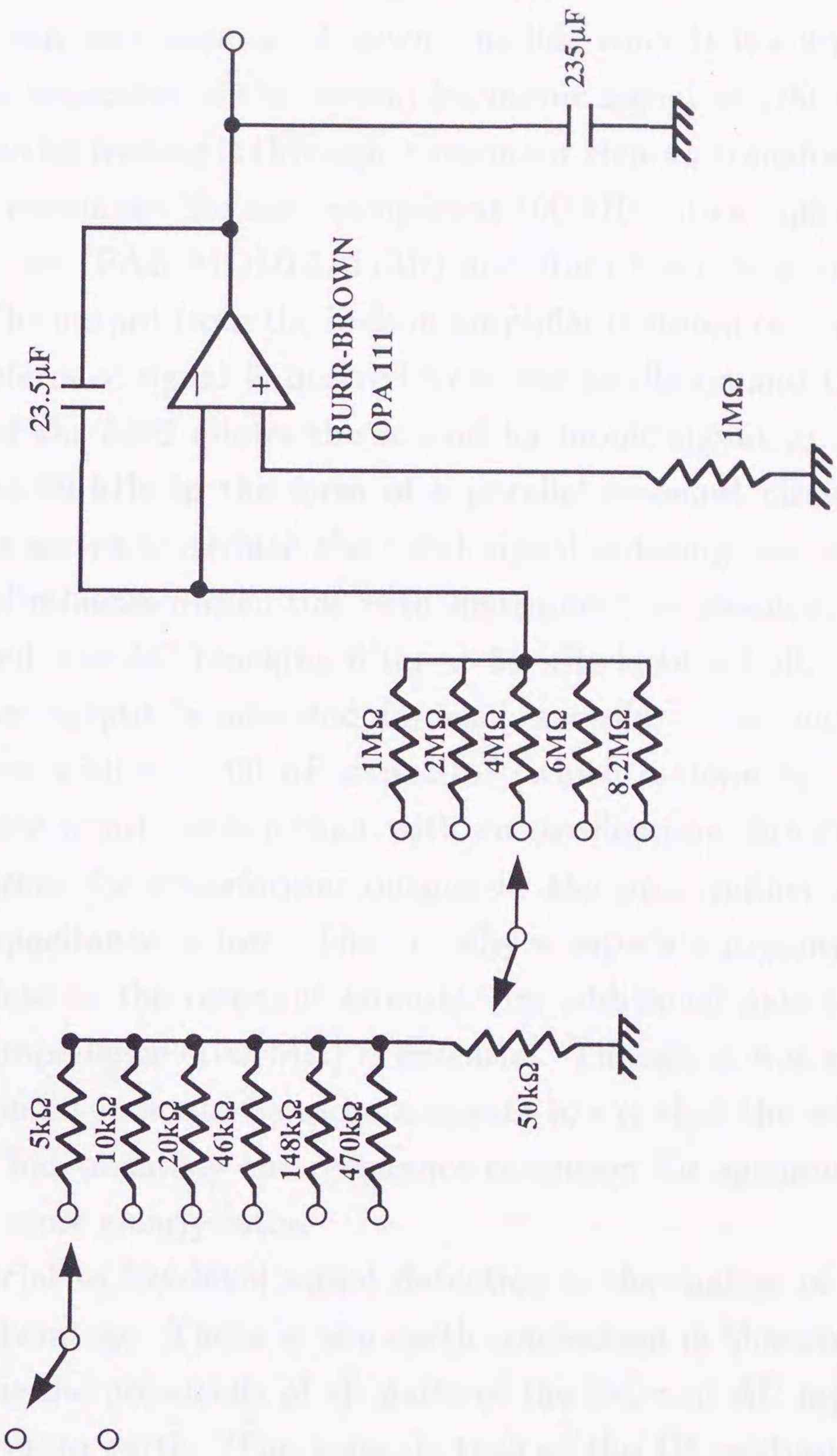

Figure 15: A DC bias circuit for tunneling spectrometer.

component in the AC current input is a 4.7 μF capacitor to block the DC current from the sweep circuit which would polarize the ferrite cores of the inductors (which could lower the resonant circuit Q values). The DC bias is monitored directly on the digital voltmeter, without amplification of the signal of filters in the line. It is crucially important that noise should not be transmitted down this line since it is connected directly to the sample. Optimum detection of the second harmonic signal at 100 kHz generated by the junction is achieved by feeding it through *a resonant step-up transformer* whose secondary circuit is tuned to resonance (for each sample) at 100 kHz into a high input impedance (10^8 Ω) preamplifier input (PAR MODEL 113P) and from there to a lock-in amplifier (PAR MODEL 5209). The output from the lock-in amplifier is stored on a microcomputer (NEC PC9801RA). A reference signal is derived from the oscillator and the internal frequency doubling facility of the 5209 allows the second harmonic signal to be detected. There is a blocking filter at 50 kHz in the form of a parallel resonant circuit located before the transformer. This serves to reduce the total signal entering the preamplifier and lock-in amplifier and eliminates difficulties with instrument overloaded, while when the first derivative is desired, the LC blocking filter at 50 kHz is tuned off. The tuning capacitor on the transformer output is adjusted for each sample. The tuning of the secondary circuit to resonance with the 100 pF capacitor (which is done by using the NF LI-75A as a high-impedance input, rather than with an oscilloscope directly) is possible only if the coaxial lead from the transformer output to the preamplifier is kept short, say 25 cm, so that its capacitance is low. That is why a separate preamplifier is desirable: it may be located close to the resonant circuits. Its additional gain (×100) is not needed but a high input impedance (100 MΩ) is essential. Though it was stated above that the transformer is resonant it would be more accurate to say that the whole circuit including the blocking filter has to satisfy the resonance condition for optimum performance. This will be illustrated more clearly later.

Absolutely crucial to low-level signal detection is the matter of choosing earths and grounds to best advantage. There is one earth connection in this circuit. It derives from the oscillator. Thus the potentials of all parts of the DC and AC input circuitry are well defined with respect to earth. The same is true of the DC output circuit and the AC output circuit as far as the transformer primary. All of the circuit with the exception of the DC supply, is housed in an aluminum box. The low-signal (earthed) line from the oscillator is grounded to the box. The transformer secondary circuit is separately grounded to the aluminum box and this defines the potentials of all remaining points on the AC output circuit.

Some effort was made to optimize the quality factor of the coils in the resonant circuits. The three single coils were wound on TDK ferrite pot cores, type H_{6H3}, P22/13, A250-

52H. Flanges, Trimmers, and Bobbins are TDK TF 4.5-2C1, TB 4.5-4C1-T, and BP 22/13-6/2, respectively. Specifically, the 0.94 mH inductance has 61 turns of 0.4 mmϕ lacquer-insulated copper wire, the 2.2 mH inductance has 93 turns of 0.32 mmϕ wire, and the 0.22 mH inductance has 29 turns of 0.5 mmϕ wire. The cores are 22 mm in diameter, and 13 mm high with an inductance factor, A_L, of 250 nH per turn. The transformer is on a TDK ferrite pot core, type H_{6A3}, P26/16 (26 mm diameter, 16 mm high), A400-52H with an A_L of 400 nH per turn. Flanges, Trimmers, and Bobbins are TDK TF 5.5-2C1, TB 5.5-4D2-U, and BP 26/16-622, respectively. The 0.05 mH primary has 110 turns of 0.5 mmϕ wire, and the secondary has 155 turns of 0.25 mmϕ wire to give a self-inductance of 10 mH. Typical quality factor (Q) values were 100. The ferrite cores have tuning slugs (trimmers) but they do not offer good resolution and it is convenient to have 100 pF trim capacitors on the 2.5 nF and 5 nF components. The circuits can not be tuned reliably when monitored with a standard 1 MΩ input impedance oscilloscope; the NF LI-75A preamplifier performs well as a buffer in this task.

In order to facilitate data analysis, the spectrometer has been interfaced with an NEC PC9801RA microcomputer. It is therefore possible to store in digital form the appropriate output from the lock-in amplifier and the junction bias.

Further some attentions must be paid to the circuit description. The use of coaxial or shield wires is crucial except for ground lines. For the input of the preamplifier, the use of the differential input is crucial. A separation of groundings between the first and second circuits in the transformer is necessarily done. The ground terminal in an input of the lock-in amplifier is floating. A separation between electronic instrumentations is done with line filters (TDK NOISE FILTERS TYPE ANF-106). An aluminum plate (2 mm thickness) is put for a separation between a microcomputer and other electronic instrumentations. The indicator for $2f$ band pass filter of lock-in amplifier is used for the adjustment of the oscillator frequency. The applied bias voltage across the tunnel junction is monitored on HP Model 3478A, and from there is fed to and stored on the computer. For the adjustment of the small amplitude (typically, 200 μV peak to peak) across the junction, the preamplifier (NF LI-75A) is used. The output bias voltage from the digital voltmeter (HP-3478A) and the f or $2f$ output voltage from the lock-in amplifier are under the control of a microcomputer (NEC PC 9801RA) with GP-IB controller, and are stored on the hard disk.

To test the spectrometer, the low-bias Pb superconducting phonon spectrum is measured in a Pb-Pb oxide-Pb tunnel junction. Here modulation amplitude has been reduced to 250 μV peak to peak (88 μV RMS) in order to allow the superconducting Pb phonon structure to be traced out for Pb-Pb oxide-Pb junction at a temperature of 4.2 K. This spectrum is taken with a lock-in time constant of 3 sec. The resulting superconducting

Pb phonon spectrum is shown in Fig. 16. The more fine structure of Pb phonon is clearly observed[9, 12, 162].

Circuit Analysis: The tuned filters of the input circuit may each be treated as an independent unit and designed to satisfy the usual resonance condition, $\omega^2 LC = 1$. Also, they can be tuned individually in isolation from the rest of the circuit. Component values are chosen in the light of inductor core availability[†].

The detection circuit, on the other hand, must be considered as a whole if its performance is to be optimized. Although it has a filter circuit tuned to 50 kHz to reduce the modulation signal to the transformer, this same circuit will behave as a capacitor (of 37.5 μF for the circuit of Fig. 14) at 100 kHz. The 4.7 μF blocking capacitor has a low impedance at 100 kHz and may be neglected. Analysis of the detection side then follows straightforwardly.

Suppose a 100 kHz signal V_i is developed by the tunnel junction and is fed into the primary circuit of the transformer. If the self-inductance of the primary is L_1, the capacitance of the 50 kHz parallel resonant circuit at 100 kHz is C_1, and the transformer mutual inductance is M, the circuit reduces to that shown in Fig. 17. The secondary winding of the transformer has self-inductance L_2, and the tuning capacitor is denoted C_2. Current flowing in the primary circuit is i_1, and that in the secondary i_2. The latter develops an output voltage signal, V_0. The overall impedance of the circuit as seen by the junction is Z_i.

For the primary circuit we may write

$$V_i = i_1 Z_i = i_1 \left(\frac{1}{j2\omega C_1} + j2\omega L_1 \right) + j2\omega M i_2, \tag{49}$$

and for the secondary circuit

$$0 = i_2 \left(\frac{1}{j2\omega C_1} + j2\omega L_2 \right) + j2\omega M i_1, \tag{50}$$

where we assume that the inductors are ideal. It follows that

$$\frac{V_o}{V_i} = \frac{-(2\omega)^2 M C_1}{1 - (2\omega)^2 (L_1 C_1 + L_2 C_2)}, \tag{51}$$

and maximum output is achieved when

$$(2\omega)^2 (L_1 C_1 + L_2 C_2) = 1. \tag{52}$$

[†] See for example TDK FERRITE CORES-2 DATA Book (1988) or equivalent publications from other manufactures.

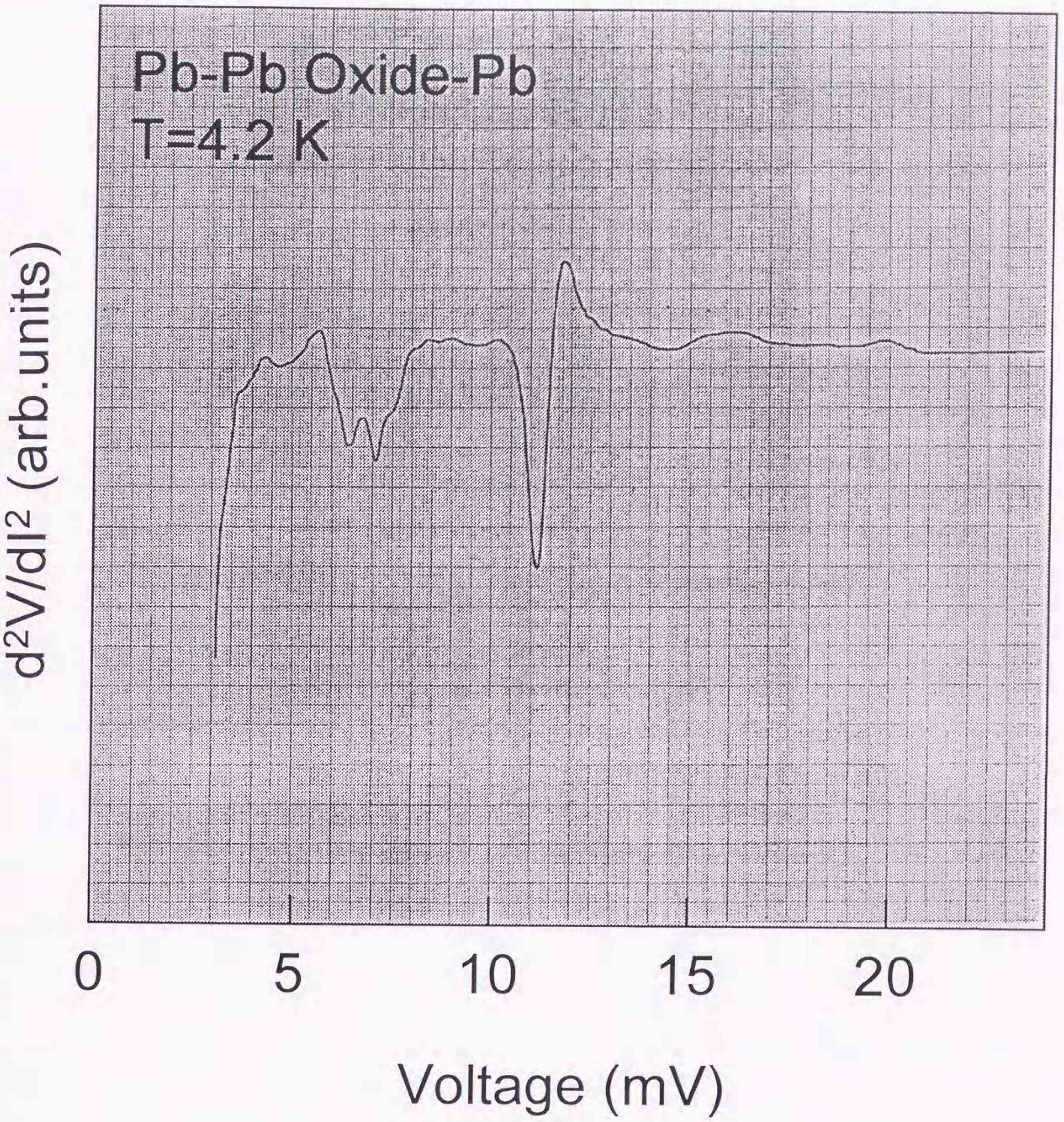

Figure 16: Second derivative d^2V/dI^2 spectrum of Pb-Pb oxide-Pb tunnel junction at 4.2 K. The both electrodes are superconducting. The fine structures of the superconducting Pb phonons are observed clearly. X axis: 1mV/cm; Y axis: d^2V/dI^2 (arb.units).

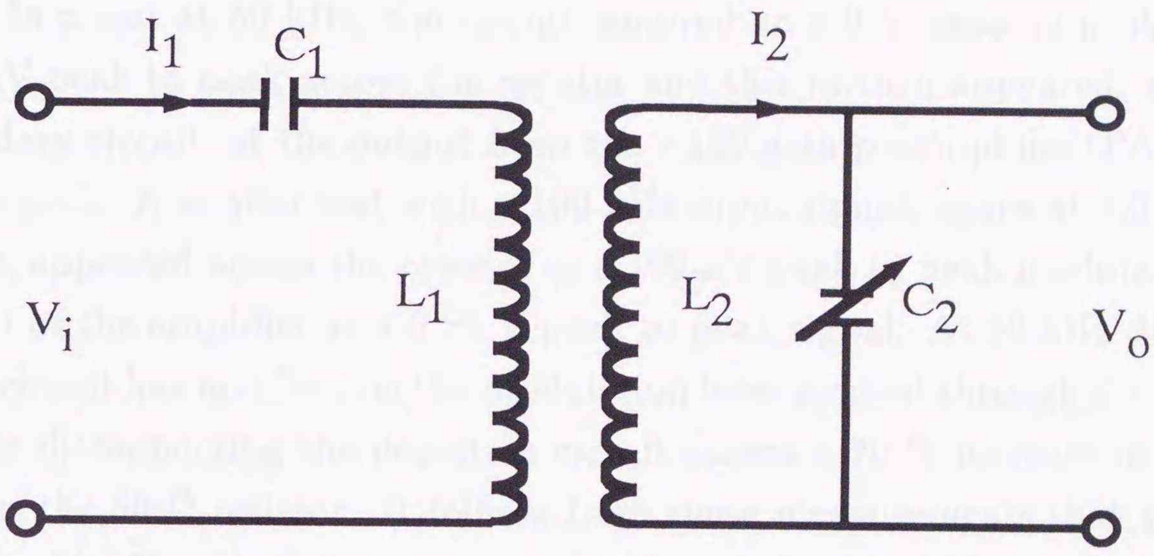

Figure 17: Equivalent circuit at 100 kHz for detection and amplification of second harmonic signal generated in tunnel junction.

When the resistance of the inductor windings is included the resultant output remains finite[‡]. The important result is that both primary and secondary circuit components must be chosen to meet the resonance condition. Good balance between the primary and secondary circuits dictates that L_1C_1 and L_2C_2 should be approximately equal. At the same time it is clear from (51) that at resonance

$$\frac{V_o}{V_i} \propto \left(L_1C_1 \cdot L_2C_2\frac{C_1}{C_2}\right)^{1/2}, \tag{53}$$

(where we assume perfect transformer coupling) and it is desirable to make C_2 as small as possible while the transformer step-up ratio, L_2/L_1, should be as large as possible. These considerations have led to the selection of component values shown in Fig. 14.

Circuit performance: The circuit performance may be examined by applying a 50 kHz or 100 kHz sinusoidal signal from the oscillator and substituting a 50 Ω resistor for the junction. In a test at 50 kHz, the circuit required an 8.0 V peak to peak input signal to give 20 mV peak to peak across the resistor and this in turn appeared, after negotiating the secondary circuit, at the output from the ×100 gain preamplifier (PAR 113P) at 0.26 V peak to peak. A similar test with a 100 kHz input signal, again at 8.0 V peak to peak amplitude, appeared across the resistor as a 100 μV peak to peak modulation and then at the output of the amplifier as a 0.27 V peak to peak signal. At 50 kHz disconnecting the detection circuit has no effect on the modulation level applied through the primary circuit; at 100 kHz disconnecting the detection circuit causes a 70 % increase in the modulation seen across the 50 Ω resistor. It follows from these measurements that the input circuit reduces the 50 kHz signal by a factor of 400 and the 100 kHz signal by 8×10^4: a net preference for the fundamental by a factor of 200:1. The output circuit further suppresses the 50 kHz signal by a factor of 7.7, but enhances the 100 kHz signal by 27. This time a 208:1 preference acts in favor of the harmonic.

Since the whole circuit transmits both fundamental and harmonic from the oscillator with roughly equal amplitude at the output to the preamplifier, it could be embarrassing if the oscillator had substantial harmonic distortion in its output. Then the lock-in amplifier might become overloaded with unwanted harmonic signal. Equally, variations in the harmonic content of the oscillator output with time could be troublesome. Neither problem was found with the oscillator used.

Screening and mains filtering: The problem of noise, both radiated and mains-borne is substantially eliminated in the present spectrometer by performing all measurements in a screened box with a filtered mains supply. The box is totally screened with aluminum

---

[‡] As well as resistance of the inductors, the capacitance, C_s, of the samples has been disregarded in this analysis. When included the latter requires C_1 to be replaced by $C_1C_s/(C_1+C_s)$ in (52). It represents only a small correction.

sheets of thickness 2.0 mm and the mains filtered by means of NF noise filter transformer (model NT-500C). The thickness of aluminum used ensures substantial screening. Operation at lower frequencies is avoided for two reasons. The first is that adequate screening would require excessive thickness of aluminum in the construction of the box, or the use of magnetic materials. The second reason is that, in general, noise from a given junction drops as the frequency of operation increases.

Four-point probe measurements: For measurements of the energies of either accurate singular points in tunneling conductance or particular modes in the $\mathrm{d}^2V/\mathrm{d}I^2$, it is necessary to measure accurately the potential difference across the junction. To achieve this, four-point probe measurements are generally used. The essential features of a four-point probe measurement on a sample of resistance R are shown in Fig. 18. Current is supplied via I_1 and I_2 and the potential difference across the specimen is measured using two separate leads P_1 and P_2. Parasitic resistances r_1, r_2, r_3, and r_4 are associated with these four leads. If the potential difference is measured with a voltmeter of sufficiently high impedance, then ohmic potential drops associated with r_3, r_4 are negligible compared with that across the specimen, and those associated with r_1, r_2 are irrelevant.

In general, if the bias voltage is measured using a method other than the four-point technique, then the part of the voltage measured will be that developed across the electrodes and connecting leads; this will vary from device to device depending upon the electrode and junction characteristics. Therefore the real bias across the tunnel junction will be less than is actually recorded, resulting in a spectrum line which is apparently shifted up in energy from its correction position. For example, if measurements were made on junctions of effective resistance 500 Ω, with electrode and connecting wire resistance of 10 Ω, then the bias measurement, using anything other than a four-point technique, would lead to upward shifts in peak position of 2 %.

4 Results and Discussion

> Wir dürfen nicht vergessen: auch unsere feineren, mehr philosophischen Bedenken haben eine instinktive Grundlage.
>
> L. W. Wittegenstein

4.1 Tunneling through Narrow Gap Semiconductor Antimony Telluride: The Effect of Dispersion Relation in Tunneling Barrier

The influence of energy band nonparabolicity in semiconductor physics has been extensively studied in bulk narrow-gap semiconductor materials[163], heterojunctions[164], inversion layers[139], etc.. The formalism for nonparabolicity in narrow-gap semiconductor

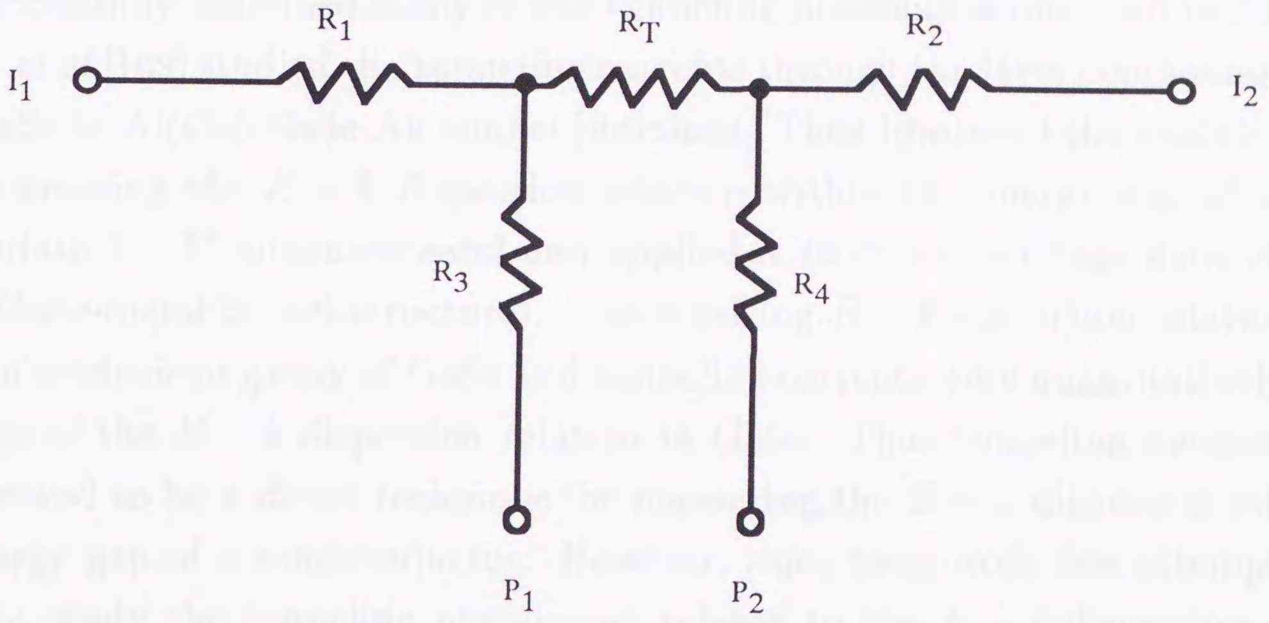

Figure 18: Schematic diagram of junction and connecting wires for four-point probe voltage measurements.

is well established based on Kane's $k \cdot p$ model[165]. On the other hand, GaAs is not a typical narrow-gap semiconductor ($E_g = 1.52$ eV at room temperature) as usually defined, but according to a more general definition that a narrow-gap semiconductor is a material where the electron energy can become an appreciable fraction of the energy gap, conduction electrons in GaAs exhibit typical narrow-gap semiconductor features due to the small band edge effective mass of electrons, $m_e^* = 0.067 m_0$ (m_0: free electron mass), and conduction electrons in GaAs were described theoretically using five-level $k \cdot p$ model[166]. Ariel Altschul *et al.*[167] derived a dispersion relation using $k \cdot p$ model, which can account for nonparabolicity in both narrow- and wide-gap isotropic semiconductors.

Stratton *et al.*[168] recognized the importance of the $E - k$ dispersion relation within the forbidden gap in describing tunneling through solids, and were able to piece together an $E - k$ relation for AlN by measuring the thickness dependence of the tunneling probability at several values of applied bias. This experimentally determined $E - k$ relation successfully described many of the tunneling phenomena observed in AlN thin films. Kurtin *et al.*[169] studied the tunneling currents through the layer compound semiconductors GaSe in Al(Cu)-GaSe-Au tunnel junctions. They improved the analytical technique for determining the $E - k$ dispersion relation within the energy gap of a solid (from appropriate $I - V$ measurements) and applied it to current-voltage data obtained from metal-GaSe-metal tunnel structures. The resulting $E - k$ dispersion relation was shown to be an intrinsic property of GaSe and tunneling currents were quantitatively understood in terms of the $E - k$ dispersion relation in GaSe. Thus tunneling measurements have been proved to be a direct technique for measuring the $E - k$ dispersion relation within the energy gap of a semiconductor. However, since their work few attempts have been made to study the tunneling phenomena related to the $E - k$ dispersion relation in a semiconductor used as a tunneling barrier in a normal metal-semiconductor-normal metal tunnel structure. For the superconducting metal electrodes, they have been continuously studied in relation to Josephson junctions[170]. These studies have been motivated by the possibility of high-frequency applications such as detectors, superconducting quantum interference device (SQUID) magnetometers, etc.[152], due to the relatively low dielectric constant of the semiconductors. M–I–M systems with a semiconductor barrier are intrinsically interesting with regard to the physics of tunneling. Narrow-gap semiconductors are especially good candidates for the tunneling barrier, since a small energy gap leads to the coupling of the conduction and valence bands, namely, a nonparabolic dispersion relation. In metal-NGS-metal tunnel structures, the small forbidden gap of a semiconductor consists of a tunneling barrier and therefore it is expected that there exists a variety of tunneling conductance which reflects the nonparabolic dispersion relation even with a small applied voltage. This interest is based upon an assumption that the energy dependence of the decay constant k in tunneling electrons can be described by the dispersion relation in the forbidden gap of the semiconductor.

In this section, electron tunneling experiments on Au-Sb_2Te_3-Al tunnel junctions to investigate the correlation effects between tunneling electrons and the coupling effects (nonparabolicity in $E-k$ dispersion relation) between the conduction and valence bands in the Sb_2Te_3 tunnel barrier in which the Sb_2Te_3 is a narrow-gap semiconductor[171], where the dispersion relation in conduction and valence bands are nonparabolic, are discussed[172, 173]. This experimental results are compared to the theoretically calculated tunneling conductance in a Au-Sb_2Te_3-Al tunnel junction where the effect of the energy band nonparabolicity in the $E-k$ dispersion relation of Sb_2Te_3 is involved in the tunneling probability.

The tunneling conductance in a Au-Sb_2Te_3-Al tunnel junction at 4.2 K is shown on an extended scale of bias voltage in Fig. 19. The tunneling conductance enlarged in the low bias voltage region is presented in Fig. 20. Positive bias corresponds to raising the Fermi level of the Au with respect to that of the Al. Some very interesting features are observed. First, the measured tunneling conductance shows a prominent narrow width peak just at 0 meV. Second, after the conductance decreases to the conductance minimum at about ± 6 meV and shows sharp undershoot structures (and the shoulder structures at ± 2 and ± 3 meV considered as impurity bands are observed, that could be described later), it increases sharply and reaches some value at about ± 7 meV. On the other hand, the curve measured at 77 K shows a usual parabolic curve as shown in Fig. 21.

Similar zero bias conductance peaks have been observed as spin-flip (Zeeman) transition caused by paramagnetic ions included in various tunnel structures[25, 26]. But the width of the zero bias conductance peak caused by magnetic impurity atoms is much larger than that of the conductance peak observed in this study. Moreover, for the conductance peaks observed before, such substructures, i.e., undershoot structures after zero bias conductance peak and the abrupt lowering of the rate of increase after sharp increase of the conductance have never been observed. Therefore these interesting features in the tunneling conductance should be ascribed to another physical origin.

The observed features can be associated with the nonparabolic dispersion relation within the energy gap of the narrow-gap semiconductor Sb_2Te_3. First, a tunneling equation involving the $E-k$ dispersion relation has to be formulated.

We start with the equations (4) and (7). That is, surface effects such as surface levels, accumulation or inversion layer, are ignored. The rationale for ignoring the above effects will be described later. Moreover, the rationale for using the WKB approximation with no prefactors will be also described later. In general, the decay constant K is a function of the electron energy E, parallel component of the wave vector $\mathbf{k}_t$, and the position of the

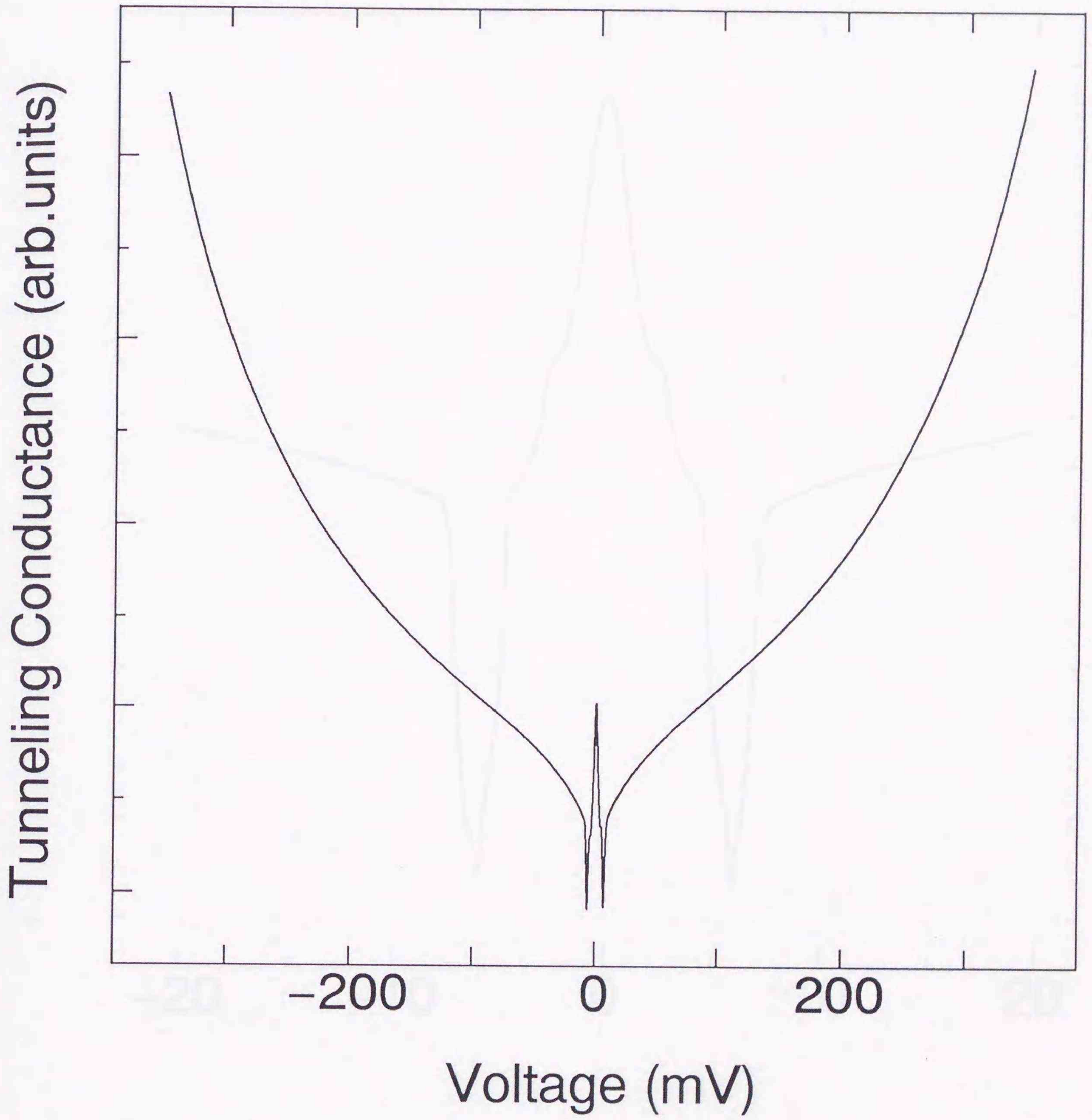

Figure 19: Tunneling conductance dI/dV versus bias voltage of Au-Sb_2Te_3-Al tunnel junction measured at 4.2 K.

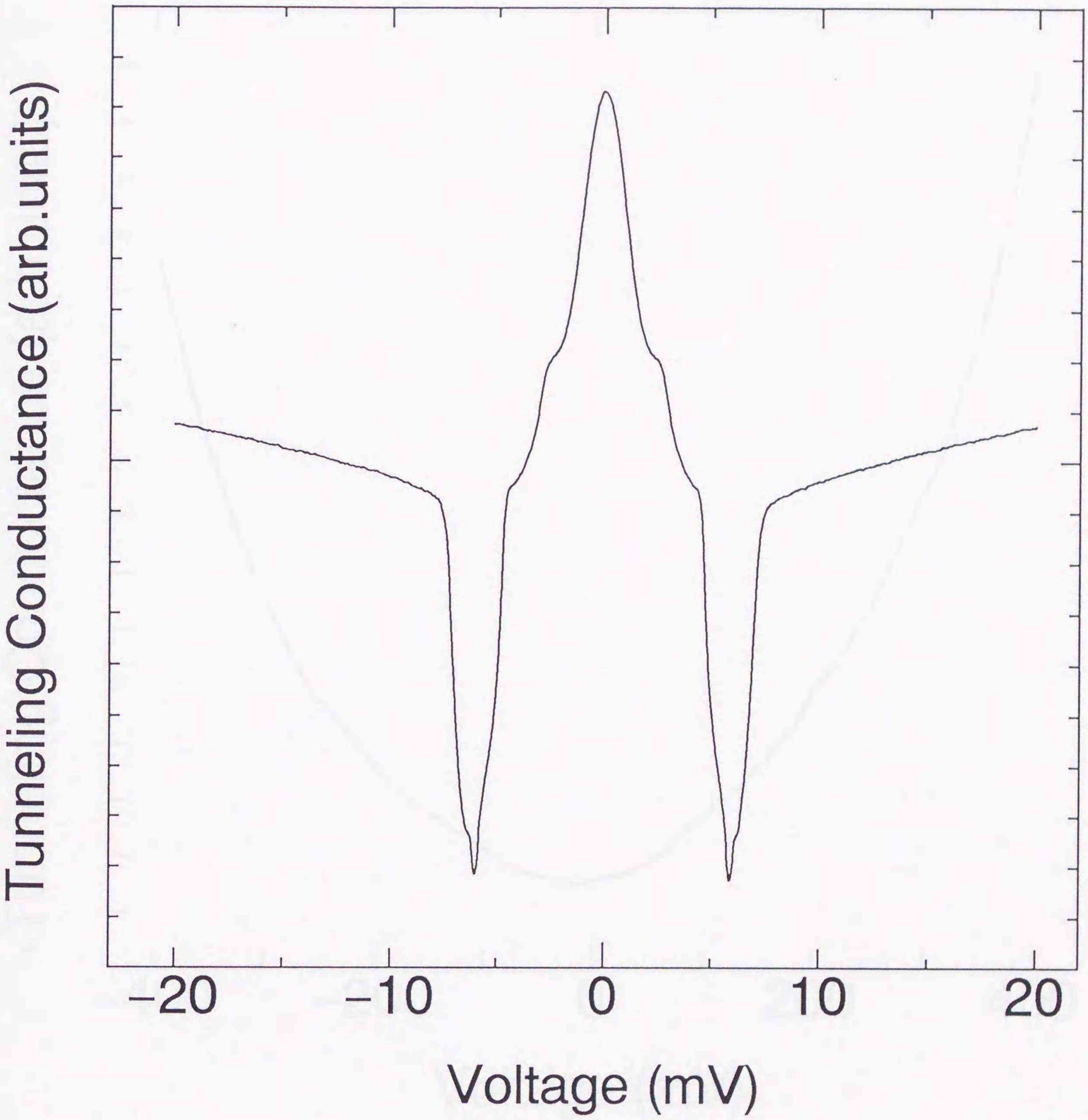

Figure 20: Tunneling conductance dI/dV versus bias voltage near the zero bias voltage of Au-Sb_2Te_3-Al tunnel junction.

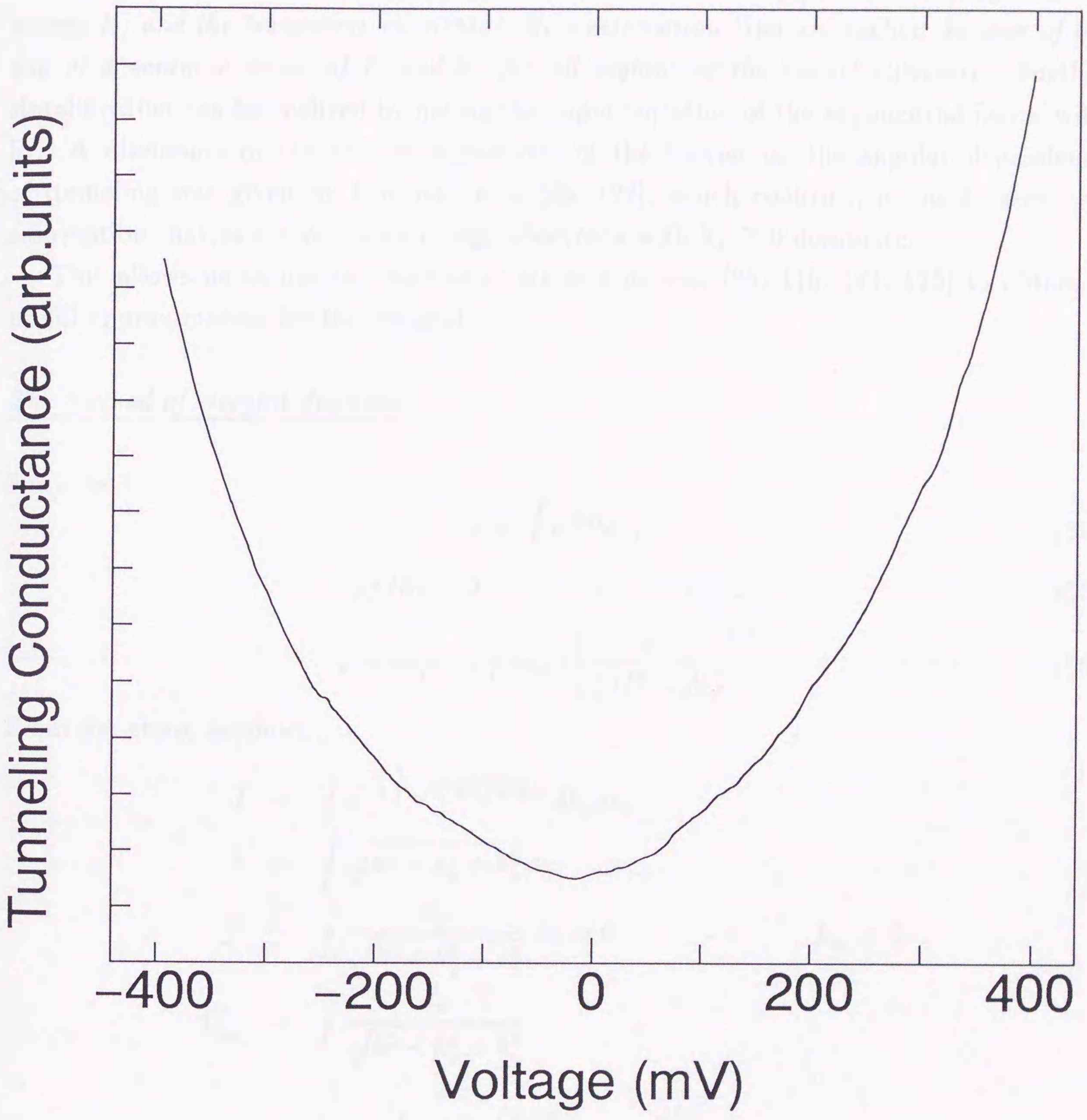

Figure 21: Tunneling conductance dI/dV versus bias voltage of Au-Sb_2Te_3-Al tunnel junction measured at 77 K.

tunneling barrier x. The dependence on x is due to the applied potential, and interface potentials which change the features of the band structure of the tunneling barrier relative to the electron's energy. Here the Fermi function factors $[f(E) - f(E + eV)]$ guarantee that the initial state is occupied and that the final state is empty. *The tunneling electron energy E, and the transverse momentum $\mathbf{k}_\mathrm{t}$ conservation laws are explicit because of the use of a common value of E and $\mathbf{k}_\mathrm{t}$ for all regions of the tunnel structure.* Further simplification can be realized by noting the rapid variation of the exponential factor with $\mathbf{k}_\mathrm{t}$. A discussion of the role of eigenstates of the barrier on the angular dependence of tunneling was given by Dowman *et al.*[28, 122], which confirms, in most cases, the assumption that at a given total energy, electrons with $\mathbf{k}_\mathrm{t} \cong 0$ dominate.

This allows us to use *the method of steepest descents*[25, 116, 174, 175] to obtain a useful approximation for the integral.

The method of steepest descents

For $\nu \gg 1$,

$$I = \int_c e^{\nu(z)} dz, \tag{54}$$

$$\partial f / \partial z = 0 \qquad \longrightarrow \qquad z = z_0 \tag{55}$$

$$I = \exp\left(-\nu f\left(z_0\right)\right) \left[\frac{\pi}{\frac{\nu}{2}\left|f''\left(z_0\right)\right|}\right]^{1/2}. \tag{56}$$

From the above method,

$$\begin{aligned}
I &= \int e^{-2\int \sqrt{k^2+k_y^2+k_z^2}\,dx}\, dk_y dk_z \\
f &= \int \sqrt{k^2+k_y^2+k_z^2}\, dx \\
f' &= \int \frac{k_y}{\sqrt{k^2+k_y^2+k_z^2}}\, dx = 0 \qquad \longrightarrow \qquad k_{y_0} = 0 \\
f''_{k_{y_0}} &= \int \frac{dx}{\sqrt{k^2+k_y^2+k_z^2}}
\end{aligned}$$

$$\longrightarrow I = \int e^{-2\int \sqrt{k^2+k_z^2}\,dx} \frac{\pi^{1/2}}{\left(\int \frac{dx}{\sqrt{k^2+k_z^2}}\right)^{1/2}}\, dk_z. \tag{57}$$

We note that the integrand in (57) becomes zero with k_z. Therefore, we can put k_z

$= 0$ in the denominator and take out of the integration.

$$I = \left. \frac{\pi^{1/2}}{\left(\int \frac{dx}{\sqrt{k^2+k_z^2}}\right)^{1/2}} \right|_{k_z=0} \int e^{-2\int \sqrt{k^2+k_z^2}\,dx} dk_z$$

$$= \pi \left(\int \frac{dx}{k}\right)^{-1} e^{-2\int k\,dx} \tag{58}$$

We take the dependence of $K\left(E, \mathbf{k_t}, x\right)$ on ${\mathbf{k_t}}^2$ to be given by

$$K\left(E, \mathbf{k_t}, x\right) = \left[k_x^2\left(E,0,x\right) + {\mathbf{k_t}}^2\right]^{1/2}, \qquad {\mathbf{k_t}}^2 = k_y^2 + k_z^2. \tag{59}$$

We can apply the above method for (59). As the result, we obtain the following equation;

$$\begin{aligned} J\left(V\right) &= \frac{e}{2\pi h}\int_{-\infty}^{\infty} dE \exp\left(-2\int_{x_L}^{x_R} k_x\left(E,0,x\right)dx\right) \\ &\times \left(\int_{x_L}^{x_R} \frac{dx}{k_x\left(E,0,x\right)}\right)^{-1} \left[f\left(E\right) - f\left(E+eV\right)\right]. \end{aligned} \tag{60}$$

Since most tunneling experiments are performed at low temperatures to eliminate thermionic currents over the barrier, so it is sufficient to consider this equation within the limits of $T \cong 0$ K[25, 26]. Therefore the Fermi function factors disappear by $T = 0$ K approximation†.

There remains one useful simplification of (60) to be discussed. The energy E may be related to the spatial coordinate x such that k_x becomes a function of single variable $\xi(x)$. This new variable $\xi(x)$ is the difference in energy between the conduction band edge and the energy of an electron located at x (this means that the conduction band edge in NGS is taken as the origin of the energy):

$$\xi = \varphi(x) + E. \tag{61}$$

Therefore,

$$\begin{aligned} \frac{d\xi}{dx} &= \frac{d\varphi}{dx} \\ dx &= \frac{d\xi}{(d\varphi/dx)}. \end{aligned} \tag{62}$$

Representing $J(V)$ in terms of $\xi(x)$,

$$J(V) = \frac{e}{2\pi h}\int_{-\infty}^{\infty} dE \exp\left(-2\int_{\xi_{x_L}}^{\xi_{x_R}} \frac{d\xi}{d\varphi/dx} k\left(\xi\right)\right) \left(\int_{\xi_{x_L}}^{\xi_{x_R}} \frac{d\xi}{(d\varphi/dx)\,k\left(\xi\right)}\right)^{-1}. \tag{63}$$

$^{\dagger}\int_{-\infty}^{\infty} \to \int_0^V$

This expression, although somewhat approximate, is of adequate precision and contains the fundamental physics of tunneling.

Assuming now the trapezoidal barrier potential as shown in Fig. 22,

$$\varphi(x) = -\varphi_1 + \frac{\varphi_1 - \varphi_2 + eV}{d} x, \tag{64}$$

and for an applied bias in the range $-\varphi_1 < V < \varphi_2$, (63) becomes

$$\begin{aligned} J(V) &= \frac{e}{2\pi h} \int_0^V dE \exp\left(\frac{-2d}{\varphi_1 - \varphi_2 + eV} \int_{-(\varphi_1 - E)}^{-(\varphi_2 - eV - E)} d\xi k(\xi) \right) \\ &\quad \times \left(\int_{-(\varphi_1 - E)}^{-(\varphi_2 - eV - E)} \frac{d\, d\xi}{(\varphi_1 - \varphi_2 + eV)\, k(\xi)} \right)^{-1} . \end{aligned} \tag{65}$$

This equation is a suitable basis for an analysis of the tunneling characteristics near 0 K through the semiconductor tunnel barrier which has an arbitrary $E - k$ dispersion relation. In the formation in which the dispersion relation is incorporated, it is clear that a tunneling electron has a different wave vector dependent on the tunneling electron energy.

The use of trapezoidal barrier means that we ignore surface effects such as surface levels, inversion, or accumulation layer and that the slope of the band edges in the semiconductor is linearly dependent upon the applied voltage. The presence of space charge in the barrier and the effect of image charges induced in the electrodes, may lead to the deviation of the barrier shape from the assumed trapezoidal form. Space charge distorts the shape of the potential barrier because field lines originate or terminate on the trapped charge. The worst case is such that all traps are ionized and that the space charge is distributed uniformly throughout the barrier region. On the other hand, as for image charges, electrons tunneling through the barrier interact with electrons in the two metallic electrodes. This interaction can be modeled by adding, to the expression for a trapezoidal barrier potential, the potential due to image charges which one would expect (in the classical approximation) to be induced in the electrodes. This effect leads to the rounding of the edges of the barrier and to slightly lower the average barrier height. In the derivation of the tunnel equation, the above two effects are ignored, because the effects could not result in the remarkable change in tunneling conductance in the case. For example we try to estimate the thickness of depletion layer in the metal-semiconductor interface. We can estimate the interfacial thickness from the following equation;

$$\begin{aligned} d &= \sqrt{\frac{2\epsilon_s \epsilon_0}{q N_A} (V_D + V)} \\ &\simeq 25\,\text{Å}, \end{aligned} \tag{66}$$

(where the following values are used; $q = 1.6 \times 10^{19}$ cm^{-3}, $N_A = 1 \times 10^{20}$ cm^{-3}, $\epsilon_s = 36.6$[176], $\epsilon_0 = 8.85 \times 10^{-12}$ F/m, $V_D = 150$ meV, and $V = 0$ meV). Therefore the effect

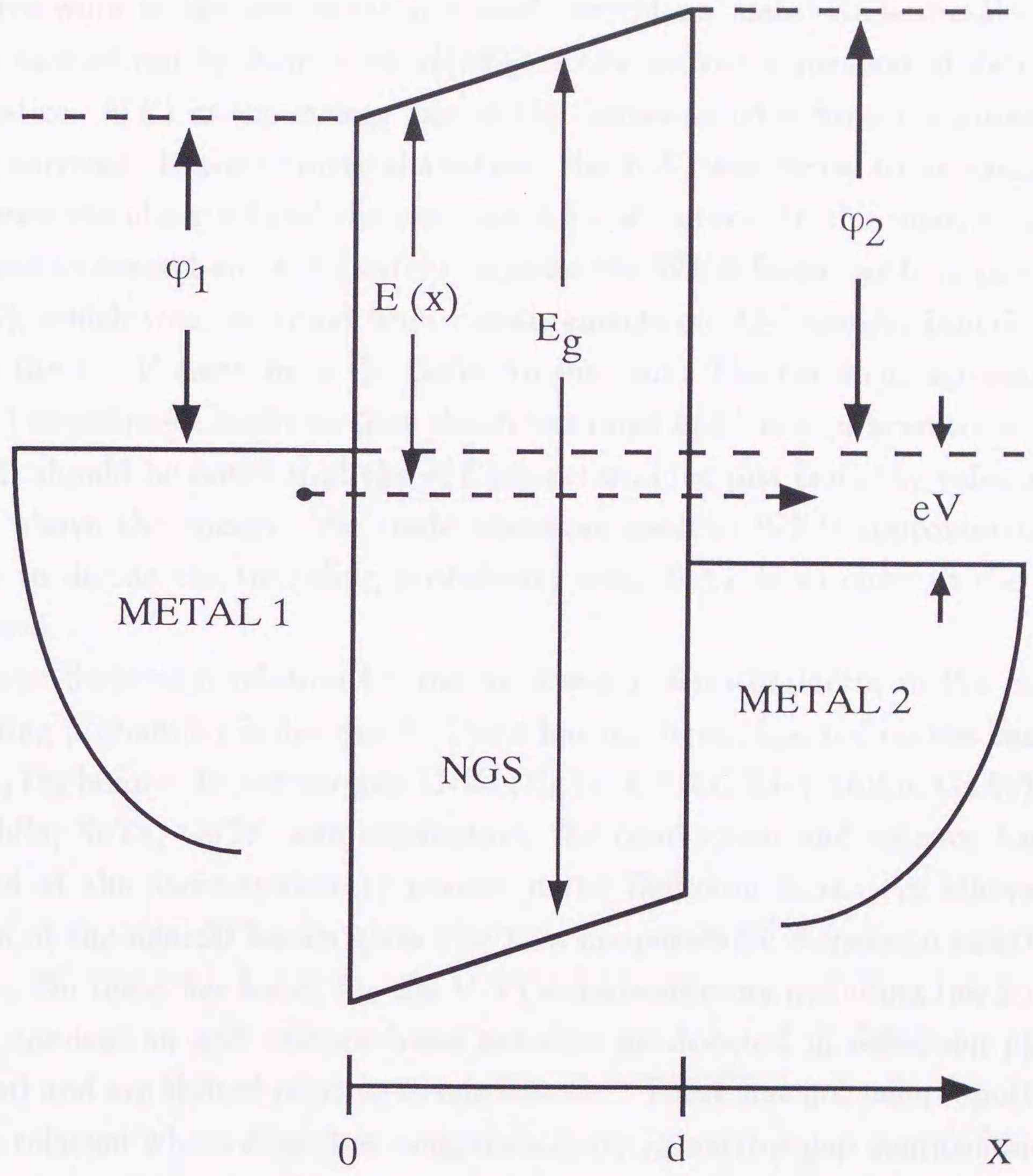

Figure 22: Schematic energy-band diagram of a metal-semiconductor-metal tunnel structure. $\varphi_{1,2}$ are metal-semiconductor barrier height. E_g is an energy gap. Metal 1 is negatively biased by eV. The trapezoidal barrier potential is assumed. $E(x)$ is the energy of the electron tunneling from metal 1 to metal 2. The zero for energy is defined at the conduction band edge at the left-hand side of the barrier.

of interfacial layer can be ignored. Next, it should be considered about the rationale for using the WKB approximation with no prefactors when E_F is so close to the edge of the valence band. For the use of the WKB approximation in the above case, there is certainly reported on a definitive and thoroughly quantitative work to justify the use of the WKB approximation with no prefactors to the valence band edge experimentally. A thoroughly quantitative work of the one electron tunnel current on metal-GaSe-metal tunnel structures was carried out by Kurtin *et al.*[169]. They proved a method of determining the $E-k$ relation, $k(E)$ in the energy gap of the semiconductor from measurements of the tunneling currents. In the numerical analysis, the $k(E)$ was varied to minimize the difference between the observed and the calculated $I-V$ curves. In this analysis the equation they derived to extract the $k(E)$ surely includes the WKB factor with no prefactors. The GaSe $k(E)$, which was extracted from measurements on Al-GaSe-Au junctions was used to predict the $I-V$ curve for a Cu-GaSe-Au junction. The excellent agreement between theory and experiment confirms that the determined $k(E)$ is a sufficiently accurate $k(E)$ of GaSe. It should be noted that the $k(E)$ is determined just from the valence band edge to 1.5 eV above the energy. We could therefore use the WKB approximation with no prefactors to decide the tunneling probability even if E_F is so close to the edge of the valence band.

Next, the dispersion relation for the narrow-gap semiconductor in the calculation of the tunneling probability is discussed. There has not been reported on the band structure for the Sb_2Te_3 before. In narrow-gap II-VI (HgTe, CdTe), III-V (InSb, GaAs), and IV-VI (PbTe, PbSe, SnTe, GeTe) semiconductors, the conduction and valence band extrema are located at the same symmetry points in the Brillouin zone. An allowance for the interaction of the nearest bands gives rise to a nonparabolic dispersion relation, $k(E)$ of Kane type. On the other hand, for the V-VI semiconductors including the Sb_2Te_3 in this work, the conduction and valence band extrema are located in reflection planes (space group $R\bar{3}m$) and are shifted relative to one another. There has not been reported on $E-k$ dispersion relation which describes nonparabolicity in narrow-gap semiconductors whose conduction and valence band extrema are located at the different symmetry points in the Brillouin zone before. So anyway, as an attempt, there has been carried out a fitting procedure between the experimental and theoretical curves using the dispersion relation of Kane type to confirm the effect of the nonparabolicity in the dispersion relation of Sb_2Te_3 for the appearance of narrow width zero bias conductance peak. Essentially, instead of the dispersion relation of Kane type, a nonparabolic dispersion relation which the different position of the bottom of conduction band and the top of valence band gives rise to, have to be used; however, as is described later, it is believed that the dispersion relation of Kane type reflects a feature of $E-k$ relation in the Sb_2Te_3.

Equation (43) has been widely accepted as the first-order approximation to Kane's $k \cdot p$ model for isotropic narrow-gap semiconductor[138, 165, 177]. Here it should be noted that the band structure of energy gap in narrow-gap semiconductors can be reflected into the smaller value of isotropic band edge effective mass m_i^*, and that the coupling term E/E_g between the conduction and valence bands is explicitly included. As for the similarities of the conduction and valence bands, there have not been reported on the detailed information about the effective masses in different $\mathbf{k}$ directions. At present we can find $m_e^* = 0.3$, $m_h^* = 0.34$ as the band edge effective masses in bulk Sb_2Te_3 single crystal from table of values in semiconductors. Therefore, it could be considered that the average effective masses of electrons and holes in Sb_2Te_3 are almost the same in absolute value; however, these effective masses would be probably anisotropic exactly. From the fact that average electron and hole effective masses are almost the same, the above dispersion relation can be used to describe both conduction and valence bands in the Sb_2Te_3. From $m_e^* = m_h^* = m^*$, equation (43) can be rewritten in the following form,

$$\frac{\hbar^2 k^2}{2m^*} = E\left(1 + E/E_g\right). \tag{67}$$

Next, we extend the $E - k$ dispersion relation in the conduction and valence bands into the energy gap, that is, we could take the $E - k$ dispersion relation in the forbidden gap as the mirror image of the conduction and valence bands. Therefore the dispersion relation in the energy gap can be described by the imaginary part of the wave vector, so we take $k = iK$, $i = \sqrt{-1}$. We should note again that Kane's model can continue the conduction and valence bands by the $E - k$ curve analytically only when the conduction and valence band edge effective masses are exactly the same or that this model can only be applied to semiconductors that have exactly the same conduction and valence band edge effective masses. The above method of analysis is introduced from the fact that *a priori* there is no reason to assume that there is any difference in the tunnel conduction between the structure where the Fermi level E_F is near the conduction band edge E_C of the semiconductor and the structure where E_F is near the valence band E_V. In a wave mechanical description of the tunneling process, the transmission of electrons or holes is mediated by an exponentially decaying wave function across the barrier. The magnitude of $k(E)$, the imaginary part of wave vector of particle in the barrier, is determined by the band structure of the barrier material, and it is physically reasonable to assume that $k(E)$ should be small for E near both E_V and E_C since $k(E) = 0$ for $E < E_V$ and $E > E_C$. Generally, the larger effective mass in the valence band tends to decrease the tunneling conductance near the valence band edge. For "indirect" semiconductors (Si, for example) the fact that E_C is not at $k = 0$ could decrease the conductance near the conduction band edge.

Substituting (67) into (65), we have the equation which is a basis for understanding tunneling conductance in metal 1-narrow-gap semiconductor-metal 2 tunnel structures using the tunneling probability considering nonparabolic dispersion relation in a narrow gap semiconductor. We can calculate the tunneling conductance-voltage curves for an arbitrary metal 1-narrow-gap semiconductor-metal 2 tunnel junction using the above equation only if the band edge effective mass m^*, the barrier width d, the energy gap E_g, and the metal$_{1,2}$-semiconductor barrier height $\varphi_{1,2}$ are given. In the analysis below, generally accepted energy gap E_g = 300 meV is used. The result for Sb_2Te_3 thin films by Damodora Das *et al.*[131], m^* = 0.02 for the effective mass is adopted, because Sb_2Te_3 thin film is used as a tunneling barrier in this study. It finds out that the use of value 0.34 in bulk Sb_2Te_3 leads to a extremely small tunneling current which we can not observe.

The theoretical curve obtained from the above equations, (65) and (67) is presented in Fig. 23 along with the experimental result in Fig. 19. As the tunneling barrier width, the measured value d = 1150 Å is used. As for the metal-semiconductor barrier height, $\varphi_{1,2}$ = 272.0 meV are chosen to fit the energy value of the conductance minimum in the experimental curve to the value in theoretical curve. This value means that the Fermi level in Sb_2Te_3 is located slightly above the valence band edge. This result seems consistent with a picture that antimony telluride is always a p-type narrow-gap semiconductor despite numerous attempts by different investigators to produce n-type semiconductor by doping or introducing appreciable alterations in the proportion of antimony and tellurium[131, 133]. The high symmetry in the tunneling conductance on an extended scale also supports the assumed value ($\varphi_{1,2}$ = 272.0 meV), because this value means that the barrier asymmetry is very small. It is seen that the theoretical curve shows a narrow width conductance peak just at 0 meV, and that in higher energy ($V > | \sim 6$ meV$|$) after conductance minimum there is a upward curvature. Therefore the theoretical curve reflects qualitatively these two features in the experimental curve well. But, the undershoot structure at about ± 6 meV and the abrupt lowering of the rate of increase in tunneling conductance at about ± 7 meV in the experimental curve do not appear in the theoretical curve. This cause has not been clear at present. Essentially, instead of (67) it should be used a nonparabolic dispersion relation where the different position of the bottom of conduction band and the top of valence band gives rise to, however, from the above result it is believed that (67) reflects a feature of $E - k$ dispersion relation in the narrow-gap semiconductor Sb_2Te_3.

Next, the tunneling conductance in a Au-$Sb_{43}Te_{57}$-Al tunnel junction at 4.2 K is shown on an extended scale of bias voltage in Fig. 24. The tunneling conductance enlarged in the low bias voltage region is presented in Fig. 25. The data obtained on the tunnel junction is shown with the theoretical curve in Fig. 26. As the metal-semiconductor barrier height, $\varphi_{1,2}$ = 297.0 meV is chosen as the fitting parameter, and the measured

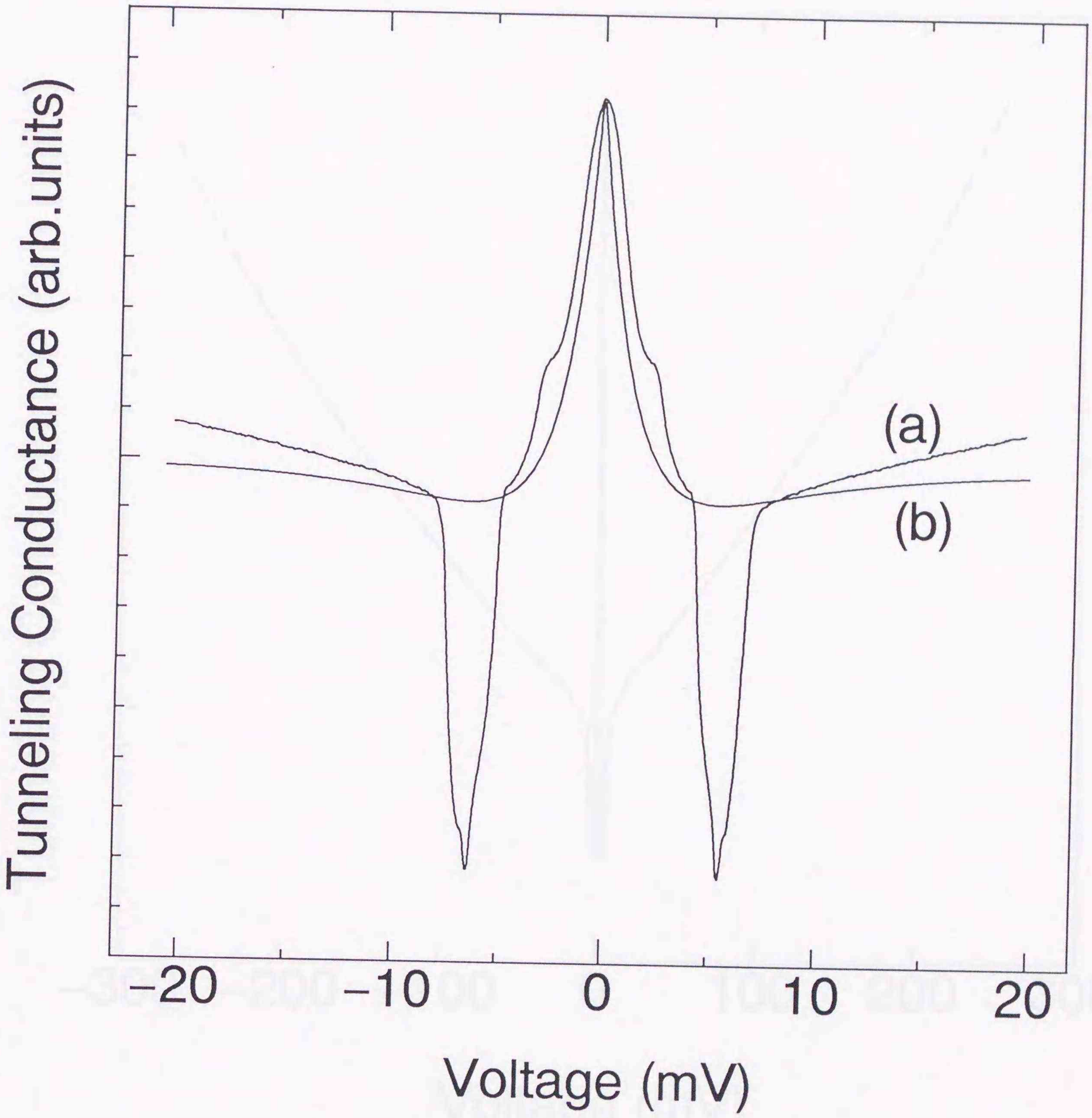

Figure 23: Comparison of the theoretical and experimental curves of Au-Sb_2Te_3-Al tunnel junction. The curve (a) is the experimental conductance and the curve (b) is the calculated conductance. $m^* = 0.02$, $d = 1150$ Å, $E_g = 300.0$ meV, $\varphi_{1,2} = 272.0$ meV.

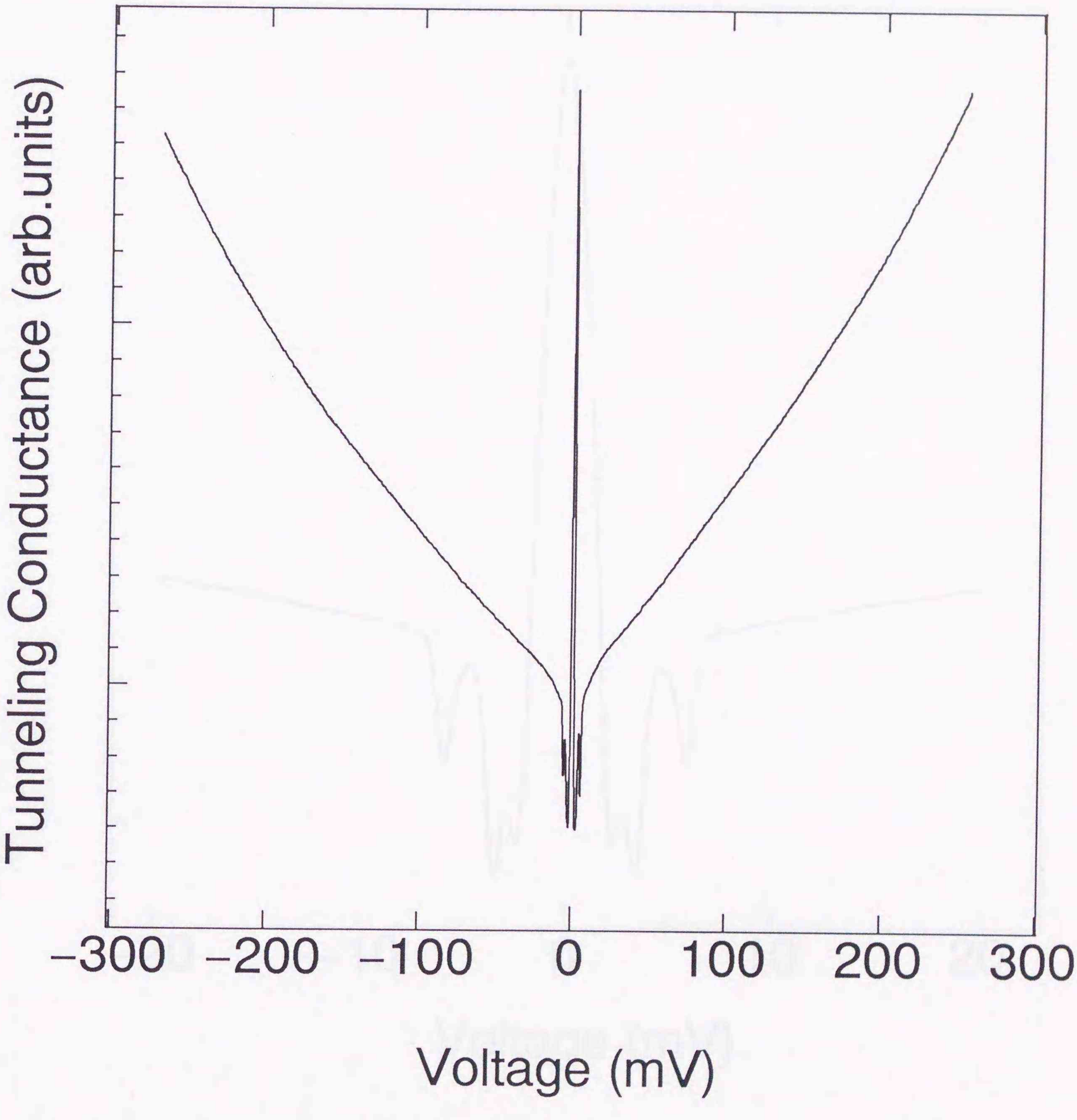

Figure 24: Tunneling conductance dI/dV versus bias voltage of Au-$Sb_{43}Te_{57}$-Al tunnel junction measured at 4.2 K.

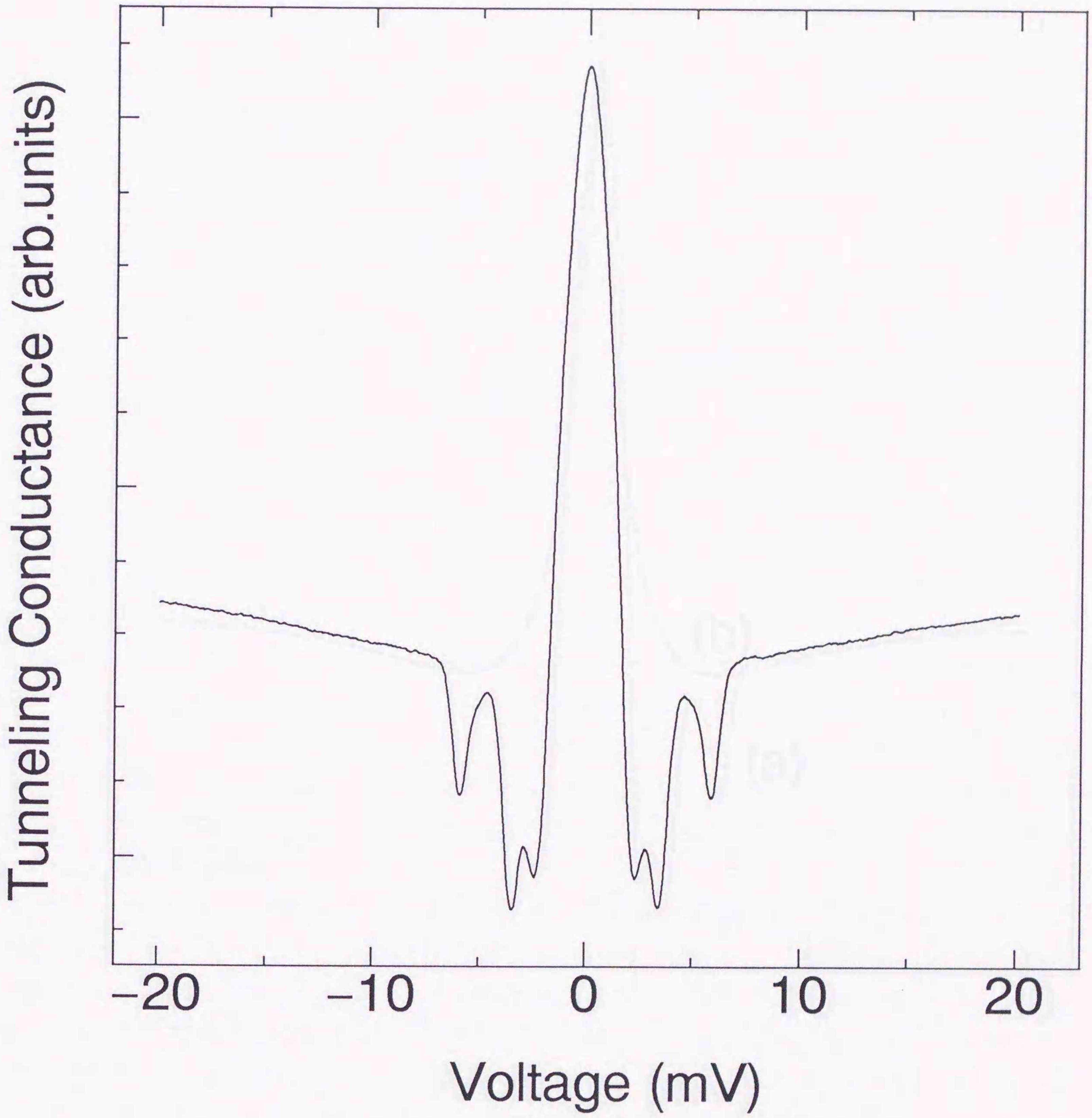

Figure 25: Tunneling conductance dI/dV versus bias voltage near the zero bias voltage of Au-$Sb_{43}Te_{57}$-Al tunnel junction measured at 4.2 K.

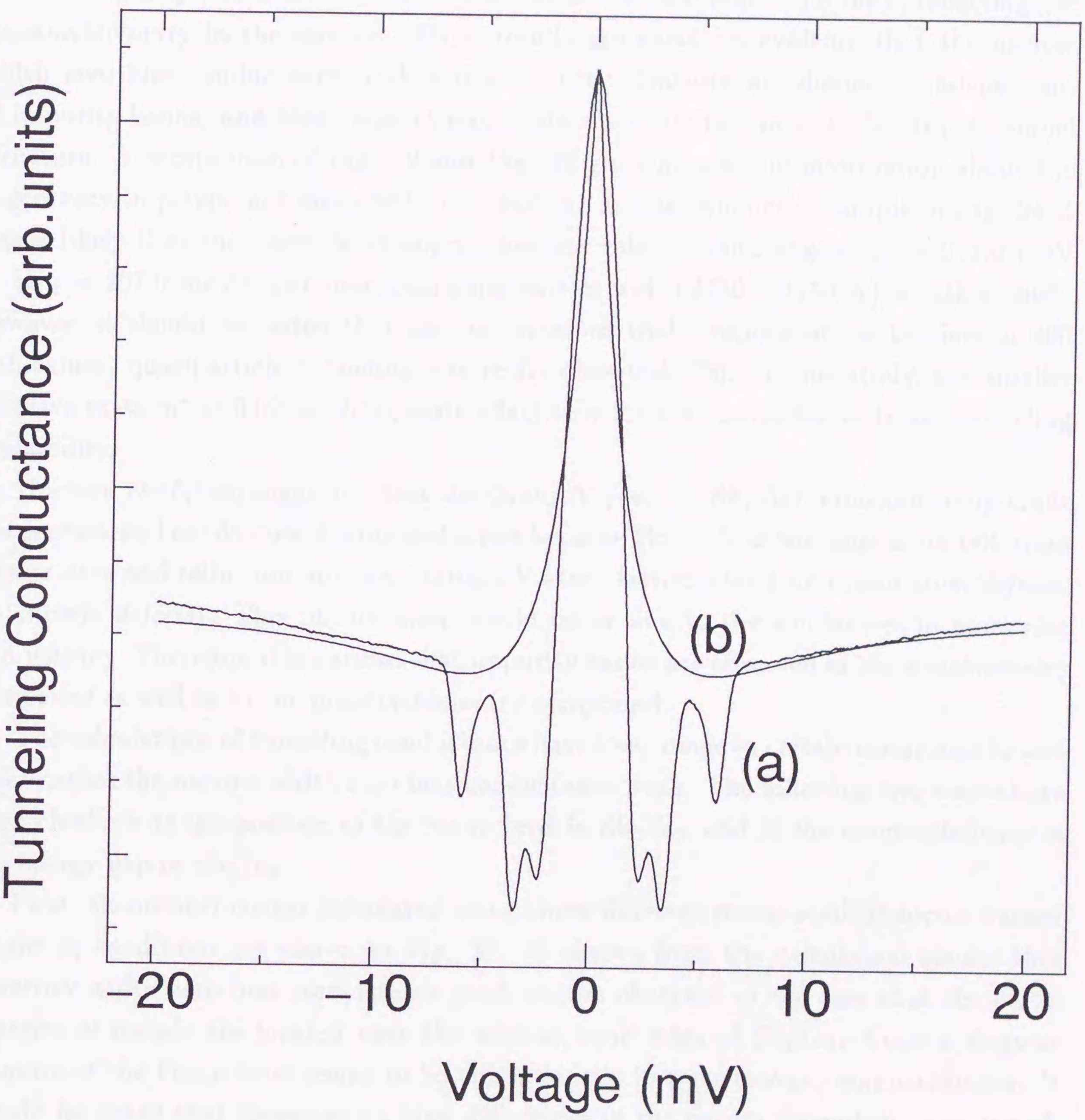

Figure 26: Comparison of the theoretical and the experimental curves of Au-$Sb_{43}Te_{57}$-Al tunnel junction. The curve (a) is the experimental conductance and the curve (b) is the calculated conductance. $m^* = 0.02$, $d = 750$ Å, $E_g = 300.0$ meV, $\varphi_{1,2} = 297.0$ meV.

value d = 750 Å is used as a tunneling barrier width. This figure also shows narrow width zero bias conductance peak, undershoot structures at about ± 3.5 meV, and the abrupt lowering of the rate of increase in conductance at about ± 6.5 meV. The two distinct impurity bands are appeared at about ± 3.0 meV and ± 4.5 meV, reflecting the nonstoichiometry in the sample. These results are excellent evidence that the narrow width zero bias conductance peak and some other features are distinctly independent of impurity bands, and that these characteristics are intrinsic in a Au-Sb_2Te_3-Al tunnel structure. A comparison of Fig. 19 and Fig. 25 gives us a useful information about the degeneracy in p-type antimony telluride. For the nonstoichiometric sample in Fig. 24 it seems likely that the Fermi level approaches the valence band edge ($\varphi_{1,2}$ = 272.0 meV → $\varphi_{1,2}$ = 297.0 meV). The used tunneling barrier width (750 – 1150 Å) is rather thick; however, it should be noted that also in junctions with evaporated Ge barriers of 800 Åthickness, quasiparticle tunneling was really observed[178]. In this study, the smaller effective mass $m^* = 0.02$ would operate effectively for the realization of larger tunneling probability.

Harman *et al.*[134] suggested that the Group V (i.e., Bi, Sb, As) tellurium compounds are necessarily heavily doped semiconductors because Group V atoms appear on tellurium lattice sites and tellurium atoms on Group V atom lattice sites (*the wrong atom defects, or antisite defects*). This phenomenon would occur due to the similarities in atom size and valency. Therefore it is natural that impurity bands are observed in the *stoichiometry compound* as well as in the nonstoichiometry compound.

The calculations of tunneling conductance have been made in certain conditions to test what causes the narrow width zero bias conductance peak. The following two issues have been checked: 1) the position of the Fermi level in Sb_2Te_3, and 2) the nonparabolicity in the energy gap in Sb_2Te_3.

First, theoretical curves calculated using three different metal-semiconductor barrier height φ_i conditions are shown in Fig. 27. It is seen from the calculation results that a narrow width zero bias conductance peak can be observed in the case that the Fermi energies of metals are located near the valence band edge of Sb_2Te_3. Such a singular location of the Fermi level seems to be characteristic in a narrow-gap semiconductor. It should be noted that there are striking differences in the curves dependent upon metal-semiconductor barrier height $\varphi_{1,2}$. Furthermore, it finds out from other calculations that such a narrow width zero bias conductance peak can be distinctly observed if either of the Fermi energies of metals is located near the valence band edge of Sb_2Te_3.

Second, the calculation using a parabolic dispersion relation ($\hbar^2k^2/2m^* = E$) as the dispersion relation within the energy gap in the calculation of tunneling probability in (65) is performed to test the effect of nonparabolic factor E/E_g in a narrow gap semiconductor.

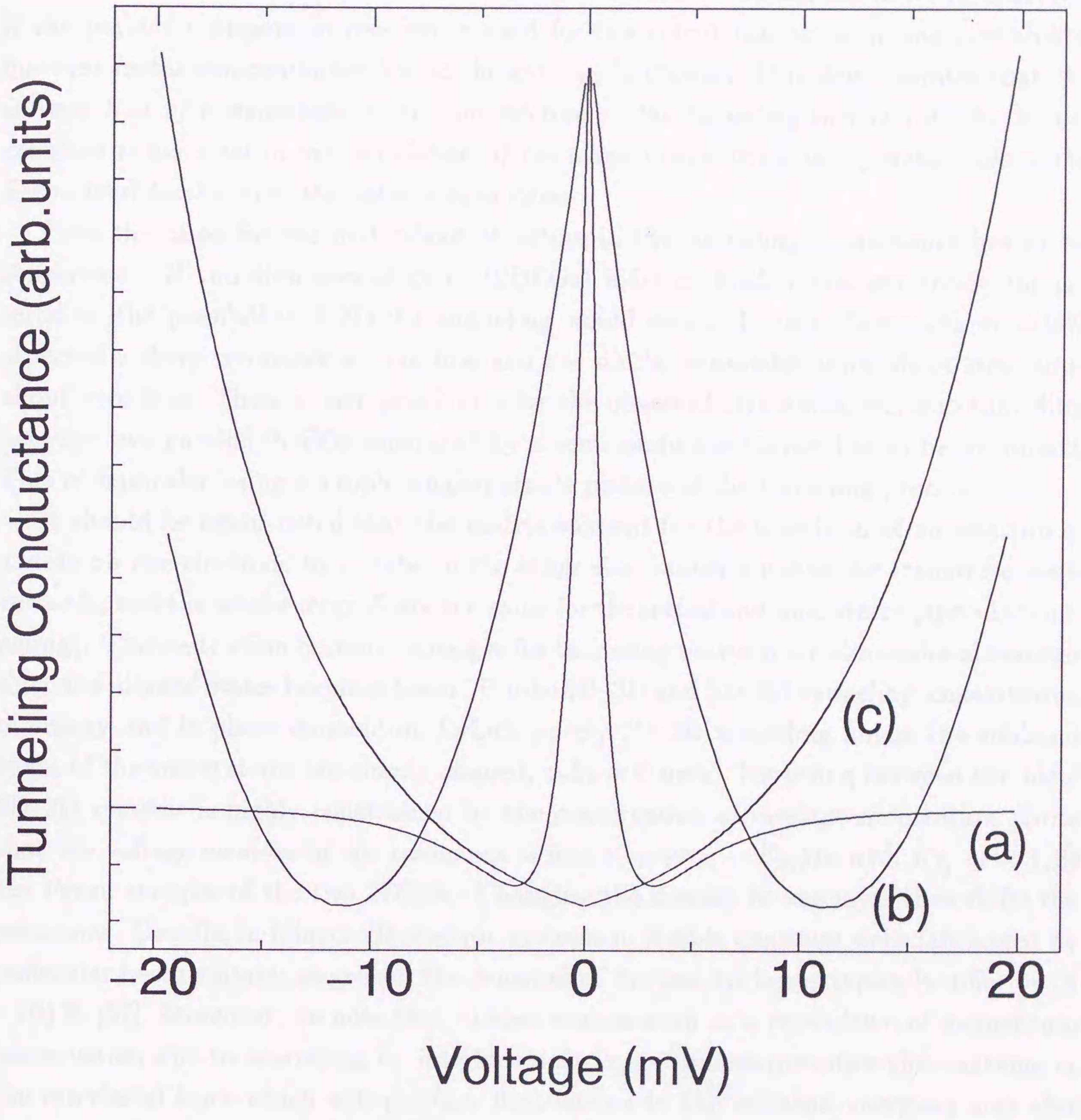

Figure 27: Theoretical curves of tunneling conductance versus bias voltage calculated for three different $\varphi_{1,2}$ values. $E_g = 300.0$ meV, $m^* = 0.02$, $d = 1150$ Å. Curve (a): $\varphi_{1,2} = 290.0$ meV; curve (b): $\varphi_{1,2} = 170.0$ meV; curve (c): $\varphi_{1,2} = 140.0$ meV.

The calculation result is shown in Fig. 28. From the result it is evident that if the same $\varphi_{1,2}$ condition is used except for the use of parabolic dispersion relation in the calculation of tunneling probability, there appears no zero bias conductance peak. It turns out from further calculation that zero bias conductance peak can never be observed if the parabolic dispersion relation is used for the calculation of tunneling probability however metal-semiconductor barrier height $\varphi_{1,2}$ is chosen. This demonstrates that *the introduction of nonparabolic dispersion relation in the tunneling barrier into the tunnel equation is essential in the calculation of tunneling conductance in a junction where the Fermi level locates near the valence band edge.*

Here the cause for the undershoot structure in the tunneling conductance has to be considered. If two-dimensional gases (2DEGs) exist at both metal-semiconductor interfaces, the possibility of 2D–2D tunneling would exist. In fact, Eisenstein *et al.*[57] observed a sharp resonance at zero bias and the similar symmetric undershoot structures about zero bias. Thus, as one possibility for the observed structures, electron tunneling between two parallel 2DEGs separated by a semiconductor barrier has to be examined. This is explicable using a simple single-particle picture of the tunneling process.

It should be again noted that the matrix element for the transition of an electron in a state on one electrode to a state on the other side vanishes unless the transverse wave vector $\mathbf{k}_t$ and the total energy E are the same for the initial and final states (specular tunneling). This restriction becomes stronger for tunneling between low-dimensional systems since the allowed states becomes fewer. Unlike 3D–3D and 3D–2D tunneling, conservation of energy and in-plane momentum forbids purely 2D–2D tunneling unless the subband edges of the two systems are closely aligned, $\Delta E_0 \approx 0$ meV. Tunneling between two ideal 2D–2D systems is highly constrained by the conservation of in-plane momentum. Note that the voltage location of the resonance is just $V = (E_{F_1} - E_{F_2})/e$ with E_{F_j} $(j = 1, 2)$ the Fermi energies of the two 2DEGs. Changing the density in one layer thus shifts the resonance. Usually, in bilayer 2D electron systems in double quantum wells fabricated by molecular beam epitaxy, as grown, the densities of the two 2D layers typically differ by (5 – 10) % [57]. Moreover, we note that various sources such as a breakdown of momentum conservation due to scattering by interface defects and inhomogeneities (fluctuations in the interfacial layer which will produce fluctuations in the subband energies) may also contribute to the broadening and the voltage location of the resonance for 2D–2D tunneling. Usually, these mechanisms could operate simultaneously. The existence of impurity bands observed in this study would strongly break the conservation of in-plane momentum. Probably, the degree of breaking of the conservation becomes different dependent upon the impurity distributions (i.e., the energy positions of impurity bands observed in this study). For the observation of conductance peak (resonance) at exactly zero bias in

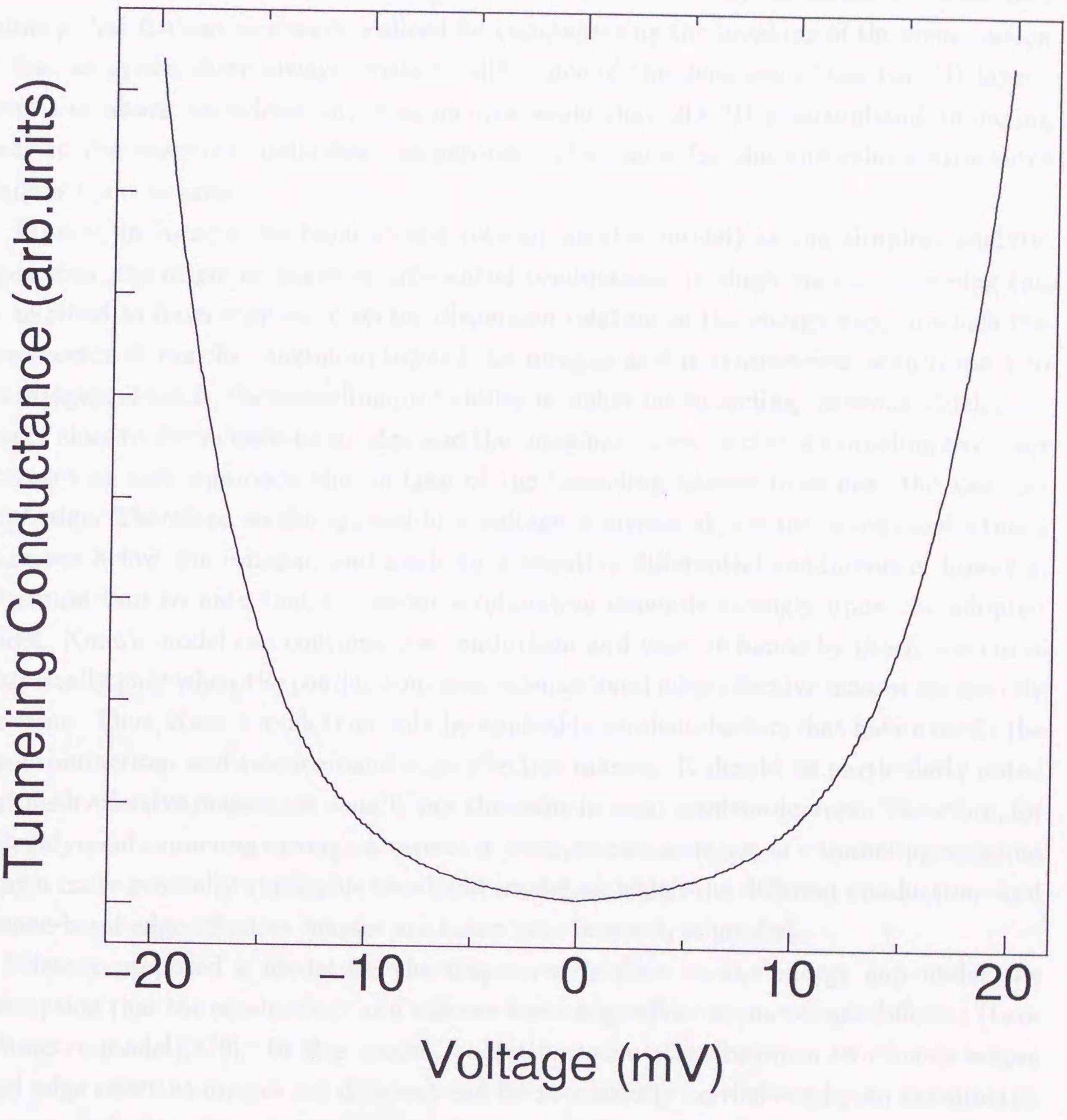

Figure 28: Theoretical curve of tunneling conductance versus bias voltage. Parabolic dispersion relation is used in the calculation of tunneling conductance. The other conditions are the same as those in Fig. 27 (a).

such circumstances, there should always exist the corresponding difference of sheet carrier density $\Delta n = n_1 - n_2$ (implying $\Delta E_F = E_{F_1} - E_{F_2}$) for compensating the break of conservation of the energy and momentum (in other words, the balance condition $n_1 = n_2$ ($E_{F1} = E_{F2}$) is obtained by centering the resonance at $V = 0$). It seems therefore very unlikely that Δn can be always realized for compensating the breaking of the conservation or that as grown there always exists no difference of the densities of the two 2D layers. From the above consideration, it is inconceivable that 2D–2D intersubband tunneling leads to the observed undershoot structures. The cause for the undershoot structures remains open at present.

Finally, in Kane's two-band model (one-parameter model) as the simplest analytic expression, the origin of negative differential conductance in single-barrier tunneling can be ascribed to its energy-wave vector dispersion relation in the energy gap, in which the wave vector shows the maximum toward the midgap and is symmetrical with respect to the midgap. That is, the tunneling probability is higher for tunneling electrons which have energy close to the valence-band edge and the imaginary wave vector of tunneling electrons increases as they approach the midgap of the tunneling barrier from near the valence-band edge. Therefore, as the applied bias voltage is increased, the tunneling conductance decreases below the midgap, and leads to a negative differential conductance; however, it is important to note that the above explanation depends strongly upon the adopted model. Kane's model can continue the conduction and valence bands by the $E - k$ curve analytically only when the conduction- and valence-band edge effective masses are exactly the same. Thus, Kane's model can only be applied to semiconductors that have exactly the same conduction- and valence-band edge effective masses. It should be particularly noted that both effective masses are usually not the same in most semiconductors. Therefore, for the analysis of tunneling through a variety of NGS, the formulation of a tunneling equation using a more generally applicable two-band model, in which the different conduction- and valence-band edge effective masses are taken into account, is needed.

Flietner proposed a model for the dispersion relation in the energy gap under the assumption that the conduction- and valence-band edge effective masses are different (two-parameter model)[179]. In this model, analytic continuation between two bands whose band edge effective masses are different can be successfully carried out by an asymmetric dispersion relation. By using this model, he successfully explained the experimental results about the surface states in the metal-semiconductor results. To apply Flietner's model in the tunnel equation (65), the dispersion relation has to be rewritten in the following way[173]:

$$\frac{\hbar^2 k^2}{2m_e^*} = E\left(1 + \frac{E}{E_g}\right)\left(1 + \alpha\frac{E}{E_g}\right), \tag{68}$$

where

$$\alpha \; = \; 1 - \sqrt{m_e^*/m_h^*}.$$

Here m_e^* and m_h^* are the effective masses at the conduction- and valence band edges, respectively. We note that Flietner's model can be reduced to Kane's model for the case of $\alpha = 0$ ($m_e^* = m_h^*$). We cannot calculate the tunnel equation (65) analytically except in the case of $\alpha = 0$, so we have to perform the calculation numerically.

The dispersion relation curves calculated using Flietner's two-band model are given in Fig. 29. As typical values in NGS, we take E_g=300 meV for the energy gap, m_e^*=0.03 for the conduction-band edge effective mass and m_e^*/m_h^* = 0.1, 1.0, 2.0 for the conduction- and valence-band edge effective mass ratio, respectively. Of these, we note that m_e^*/m_h^* = 1.0 corresponds to Kane's model. Figure 29 shows that the calculated curves that use the different conduction- and valence-band edge effective mass ratios (m_e^*/m_h^* = 0.1, 2.0) calculated with Flietner's model are quite different compared to the curve calculated with Kane's model. We thus expect that such differences in the $E - k$ relations will lead to quite different tunneling characteristics from those obtained by Kane's model. It should be emphasized that in Flietner's model the coupling effect between conduction and valence bands cannot always be the strongest in the middle of the energy gap unless the conduction- and valence-band edge effective masses are exactly the same.

4.2 Electron Tunneling into Thin Films of Antimony : Anisotropy of Fermi Surfaces and Phonons

As is described before, in tunneling experiments the confirmed anisotropy of Fermi surfaces and phonons in materials has been expected to produce anisotropy in the first and second derivatives curves which result from tunneling into different crystalline faces. However, surprisingly, there seems to be no report of this expected effect from the barrier tunneling at present, although such effects were observed in a point-contact spectroscopy experiment[124]. Since antimony, Sb is a semimetal of rhombohedral structure, i.e., a distorted cubic one, a dominant highly anisotropic electron-phonon scattering has been considered to exist, so it is of quite interest to test whether this anisotropy would be reflected in tunneling characteristics. In this section, electron tunneling experiments on a semimetal Sb carried out to investigate such anisotropic effects are discussed[180]. From the experimental results on X-ray diffraction, it turns out that exposed crystal faces can be clearly classified into three groups according to the evaporation rates. The first group is one where the evaporation rate is less than ~ 1 Å/sec, and the exposed dominant face is (003). This crystal face is characteristic of a single crystal Sb film. The second group is one where the evaporation rate is in the region between 1 and 500 Å/sec, and the dominant crystal face is (104). This crystal face appears in the films in which the longitudinal crystallites are dominant (preferred film). The third group is one where the evaporation rate is above 500 Å/sec, and the dominant crystal face is (012). This crystal face appears in the films whose textures are characteristic of a polycrystalline film. The tunneling conductance and the second derivative spectra have been measured in junctions whose antimony films are prepared by the above three kinds of evaporation conditions.

The tunneling conductances in Al-Al oxide-Sb tunnel junctions are shown to investigate the correlation between the tunneling conductances and the exposed antimony crystal faces in Fig. 30. Negative bias corresponds to raising the Fermi level of the Sb with respect to that of the Al. Hauser and Testardi[181] considered that the band edges are resolved in tunneling characteristics as the point of maximum deviation from the background parabola. Figure 30 (a), which shows the result in the Sb film exposing single crystal faces, is similar to that reported by Hauser and Testardi. Here, a major conductance bump at about -180 meV and a minor peak at about 80 meV are observed. They observed good agreement between the major conductance maximum in the tunneling curve and the optical absorption edge in the optical behavior, and therefore they identified the tunneling structure with band structure. They found an absorption edge of Sb at 200 meV. They associated this absorption edge with interband transition. If an optical transition is allowed we may expect an absorption edge to occur at the corresponding energy or perhaps a singularity of some other type in the absorptivity. If, for example, the energy gap decreases as we move away from Γ, there should be a sharp drop in the absorption at the energy corresponding to the band gap at Γ. In any case, singularities are expected in the optical conductivity, which reflect the band gaps at symmetry points. Unfortunately, the predominant structure in many cases does not arise from energy bands near the symmetry points but from large regions of wave number space where the bands are nearly parallel. Experimental studies of optical absorption in semiconductors unquestionably give information about the energy bands, but the interpretation is difficult and often ambiguous. The minor peak is quite ill defined as it depends strongly on the choice of background. They proposed that this peak may correspond to a hole Fermi energy, since it occurs near the plasma frequency.

Curves of Figs. 30 (b) and Fig (c), which shows the results in Sb films exposing the preferred, and the polycrystal orientations, respectively, are rather different from the curve of Fig. 30 (a). It turns out that the change in the tunneling conductance in curves of Figs. 30 (b) and (c) is definitely more enhanced in the negative bias. The enhancement of tunneling conductance below the bias region at which the tunneling conductance is minimum shows clearly the increase of the area (i.e., the allowed states) in the $k_y - k_z$ plane which tunneling electrons can see. This demonstrates clearly that the appearance

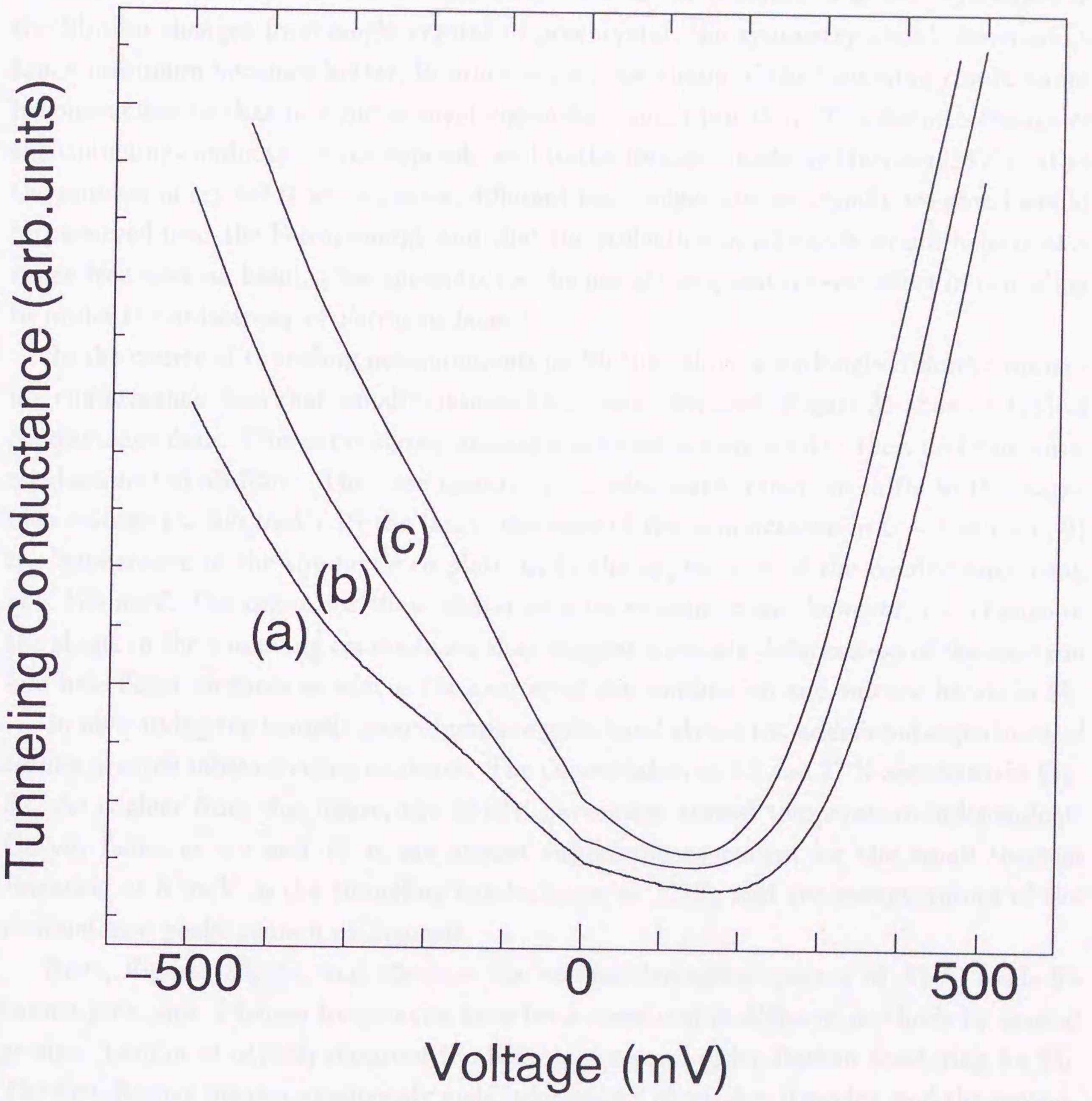

Figure 30: Tunneling conductance dI/dV versus bias voltage of Al-Al oxide-Sb tunnel junctions measured at 4.2 K. Sb thin films prepared by different preparation conditions are (a) single crystalline, (b) preferred, (c) polycrystalline.

of different crystalline faces (i.e., Fermi surfaces) can affect the shape of the tunneling conductance, although it has not been clear what kind of transition of tunneling electrons causes this change in the tunneling conductance (i.e., into which electron or hole pocket the transition occurs). Moreover it finds out that as the orientation of the crystallites of the Sb film changes from single crystal to polycrystal, the symmetry about the conductance minimum becomes better, in other words, the shape of the tunneling conductance becomes close to that in a metal-insulator-metal tunnel junction. The definite change of the tunneling conductance corresponds well to the forecast made by Harrison[182] that as the number of crystal faces increases, different band edges almost equally weighted would be observed near the Fermi energy and that the collection of all bands would behave as a single free electron band. (See appendix for the use of the quantum size effect in tunneling to probe the anisotropy of Fermi surfaces.)

In the course of tunneling measurements on Sb thin films, a strikingly different tunneling conductance than that usually observed has been obtained. Figure 31 shows a typical conductance data. This curve shows some characteristics compared to the usual tunneling conductance of Sb films. They are mainly: 1) conductance minimum shifts to the larger bias voltage ($\sim$ 205 meV), 2) the larger decrease of the conductance in 0 $\sim$ 180 meV, 3) the appearance of the conductance plateau, 4) the appearance of the conductance peak at - 478 meV. The origin for these characteristics remains open; however, the change of the shape in the tunneling conductance may suggest a certain deformation of the electron and hole Fermi surfaces as well as the overlap of the conduction and valence bands in Sb.

In identifying the tunneling conductance with band structure, additional experimental results provide substantiating evidence. The curves taken at 4.2 and 77 K are shown in Fig. 32. As is clear from this figure, the $\mathrm{d}I/\mathrm{d}V$ curves are almost temperature independent. Curves taken at 4.2 and 77 K are almost superimposed except for the small thermal smearing at 0 meV in the tunneling conductance at 77 K, and the energy values of the conductance peaks remain unchanged.

Next, Figures 33, 34, and 35 show the second derivative spectra of Al-Al oxide-Sb tunnel junctions. Phonon frequencies have been measured in different methods by several groups. Lannin *et al.*[183] reported the first- and second-order Raman scattering for Sb. The first-Raman measurements only yield information about $k \simeq 0$ modes, and the second-Raman measurements give useful information about the single-phonon density of states. This result is a consequence of the Raman scattering being primarily due to overtone scattering processes involving two phonons of the same branch of equal and opposite wave vector, rather than combination modes from different branches. The phonon dispersion in the ΓT, ΓL, and ΓX directions has been measured by Sharp and Warming[184]. Salgado *et al.*[185] have reported neutron scattering from polycrystalline semimetals using the

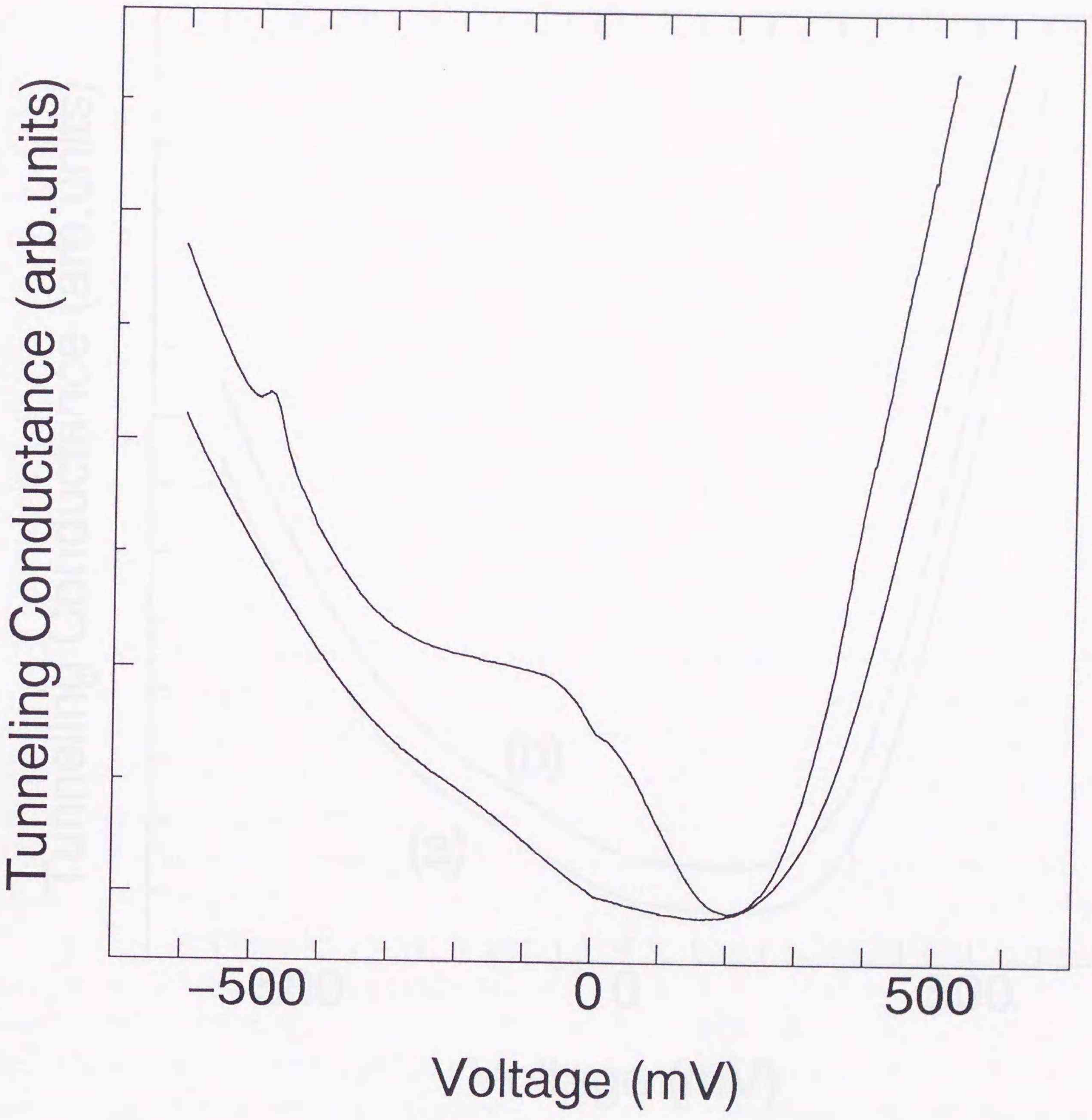

Figure 31: A strikingly different tunneling conductance dI/dV versus bias voltage of Al-Al oxide-Sb tunnel junction measured at 4.2 K (curve (a)). The curve (b) is the same as that in Fig. 30 (a).

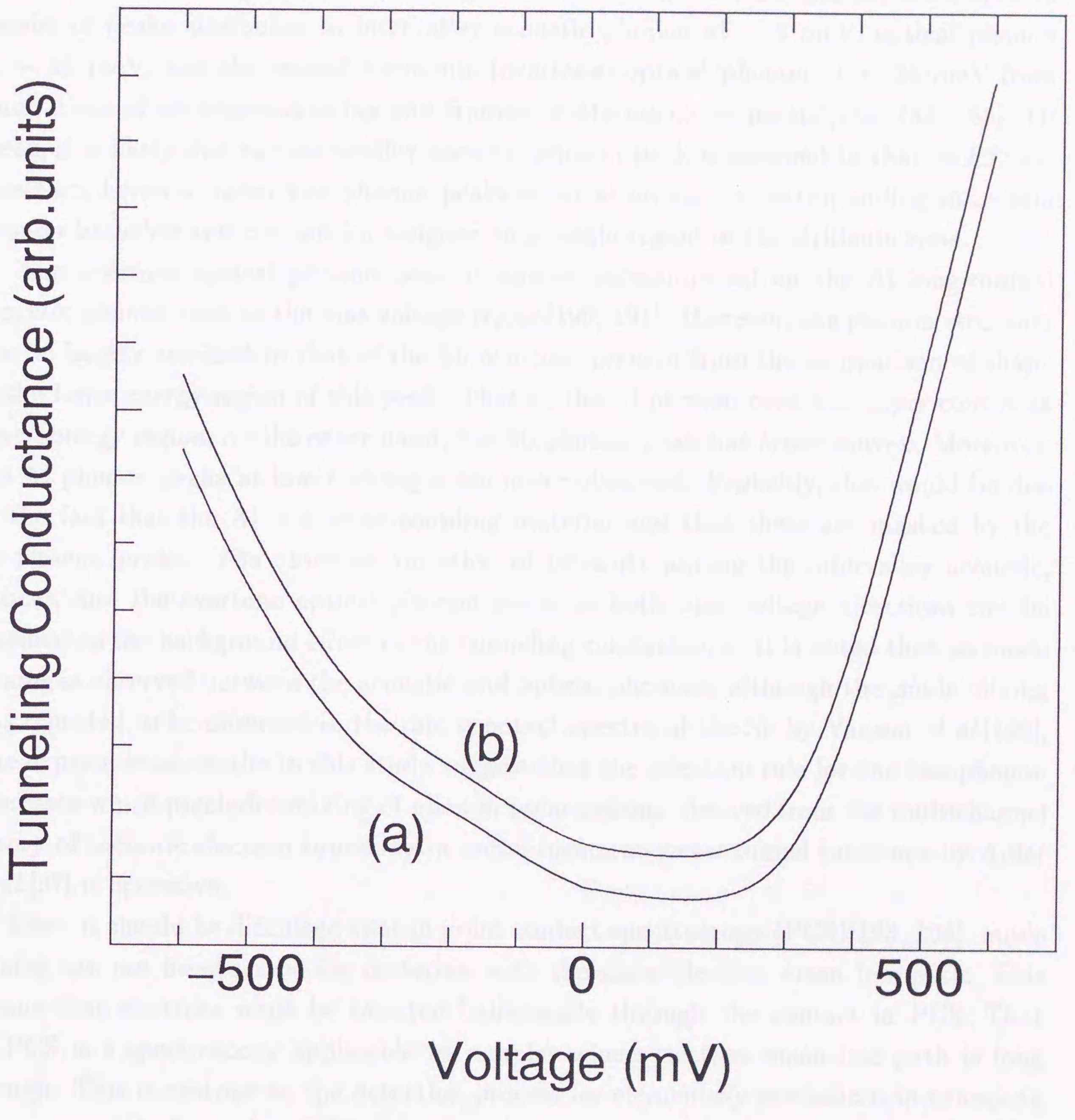

Figure 32: Temperature dependence of tunneling conductance for Al-Al oxide-Sb tunnel junction. The measurement temperatures are (a) 4.2 K and (b) 77 K.

technique of Oskotskii *et al.*[186] for coherent neutron scatterers. Their results, which yield the approximate density of phonon states, are of limited resolution of the optical modes and do not indicate the detailed features. Sosnowski *et al.*[187] calculated the theoretical optical phonon density of states. Being common to Figs. 33, 34, and 35, these spectra consist of peaks attributed to intervalley acoustic phonon at $\sim$ 8 meV, optical phonon at $\sim$ 18 meV, and the second harmonic (overtone) optical phonon at $\sim$ 36 meV from comparison of neutron scattering and Raman scattering experiments[†][183, 184, 185]. Of these, it is likely that the intravalley acoustic phonon peak is assigned to that in $\Gamma T(\lambda_3)$ direction; however, other two phonon peaks occur at an energy corresponding to certain phonon branches and can not be assigned to a single region of the Brillouin zone.

The overtone optical phonon peak is almost superimposed on the Al longitudinal acoustic phonon peak in the bias voltage region[190, 191]. However, the phonon structure can be largely ascribed to that of the Sb overtone phonon from the comparison of shape in the lower energy region of this peak. That is, the Al phonon peak has *upper* convex at lower energy region, on the other hand, the Sb phonon peak has *lower* convex. Moreover, the Al phonon peaks at lower voltages are never observed. Probably, this would be due to the fact that the Al is a weak-coupling material and that these are masked by the Sb phonon peaks. The observed variation of intensity among the intervalley acoustic, optical, and the overtone optical phonon peaks in both bias voltage directions can be ascribed to the background effect in the tunneling conductance. It is noted that no mode mixing is observed between the acoustic and optical phonons, although the mode mixing was reported to be observed in the microcontact spectra of the Sb by Yanson *et al.*[192]. The experimental results in this study suggest that the selection rule for the two-phonon processes which precludes mixing of phonon polarizations, derived from the multichannel theory of inelastic electron tunneling in metal-insulator-metal tunnel junctions by Adler *et al.*[97] is operative.

Here, it should be discussed that in point contact spectroscopy (PCS)[193, 194], mode mixing can not be observed for materials with the short electron mean free path. This means that electrons must be injected ballistically through the contact in PCS. That is, PCS is a spectroscopy applicable to samples where electron mean free path is long enough. This is contrast to the detection process for elementary excitations in tunneling spectroscopy. In fact, when PCS is applied to the sample in which mean free path is short, 1-phonon peak as well as multiple phonon peak become difficult to observe. This propose

---

[†] The number of optical phonons decreases exponentially with decreasing temperature. As a result, the scattering of an electron within the annihilation of an optical phonon is significant only at high temperatures. That is, anti-Stokes scattering can be ignored in tunneling process at low temperatures. *However,* in the process of scattering a new optical phonon can be created by an energetic electron at any temperature. This process has a weak temperature dependence.

that PCS is probably a spectroscopy more sensitive to the electron mean free path than in tunneling spectroscopy. The effect of the mean free path for the phonon detection is not evident in tunneling spectroscopy; however 1-phonon peaks are all clearly observed although 2-phonon (mode mixing) peak is not observed. The condition for which 2-phonon peak can not be observed in PCS, therefore, could not account the experimental result in this study. It should be noted that the point contact spectroscopy and the tunneling experiment can be distinguished from each other. The comparison between the point contact and the barrier-type tunneling was reported[195]. It was concluded that the barrierless contact shows a reverse energy dependence of $\mathrm{d}V/\mathrm{d}I$ compared with barrier-type tunneling. In addition to the peaks common to Figs. 33, 34, and 35, it should be particularly emphasized that a shoulder or a peak is clearly observed near 0 meV in Figs. 34 and 35, respectively. These structures have never been observed in neutron scattering experiments or Raman spectra before. Sondheimer[129] pointed that the intravalley electron-phonon interaction in semimetals could be different from that in conventional metals. Blewer *et al.*[148] considered an effective Debye temperature θ^* Sondheimer pointed out in an analysis of lattice thermal conductivity in Sb at low temperatures. They obtained $\theta_e^* =$ 2.7 meV, $\theta_h^* = 2.1$ meV for electrons and holes, respectively. On the other hand, in this study the corresponding shoulder or peak is observed at about 2.4 meV. It is therefore identified that this shoulder or peak corresponds to the intravalley acoustic phonon. This is the first observation of intravalley acoustic phonon peak in tunneling spectroscopy. At present, however, it can not be identified to which transition in the valleys the shoulder or peak should be attributed. The fact that an intermediate value was obtained between θ_e^* and θ_h^* is in agreement with the qualitative considerations made on the anisotropy of the pockets and the existence of two bands of charge carriers. That is, the effect due to the anisotropy would probably be more important than the effect brought about by the distinction between holes and electrons, and tunneling electrons would see various cross-sections of wave vector ($k_{||}$) spaces of both electron and hole pockets dependent upon the exposed crystal faces. The definite appearance of an intravalley acoustic phonon peak in tunneling spectra on the definite crystal faces demonstrates clearly that the confirmed anisotropy of phonons in Sb films produces anisotropy in the second derivative curves. Another point to be particularly noted is the difference of the half-width between intervalley acoustic and optical phonon peaks. That is, the half-widths of these peaks in Fig. 34 and Fig. 35 are much smaller than those in Fig. 33, and as the result, the separation of these peaks becomes much better. This also demonstrates that certain phonons can be detected selectively by specular tunneling. Such anisotropy of tunneling spectra has never been reported before. However, it has not been clear what kind of transition of tunneling electrons causes this change in the tunneling spectra (i.e., into which electron or hole

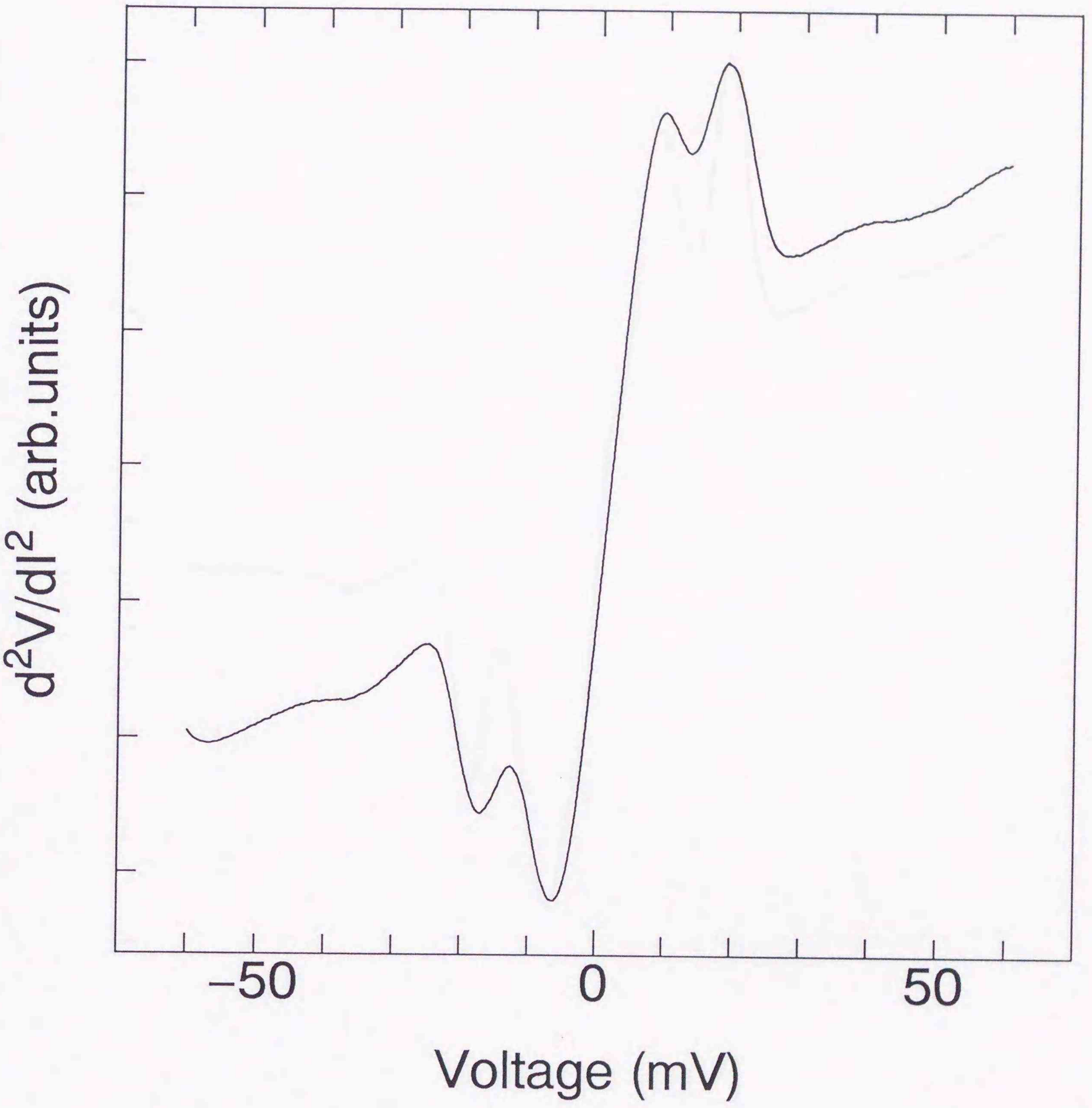

Figure 33: Second-derivative tunneling spectra of Al-Al oxide-Sb tunnel junction measured at 4.2 K. The Sb is “single crystalline”.

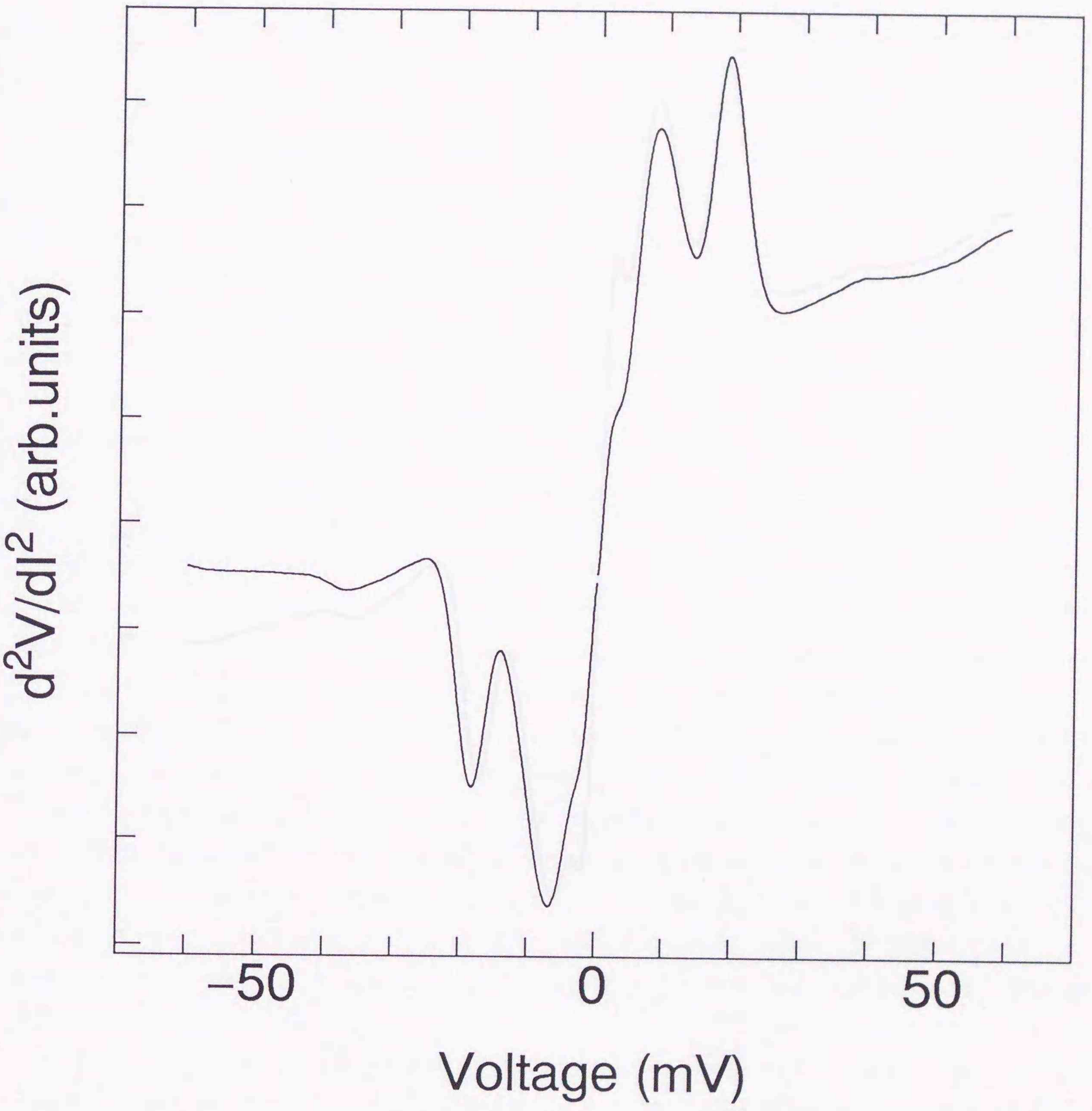

Figure 34: Second-derivative tunneling spectra of Al-Al oxide-Sb tunnel junction measured at 4.2 K. The Sb is "preferred".

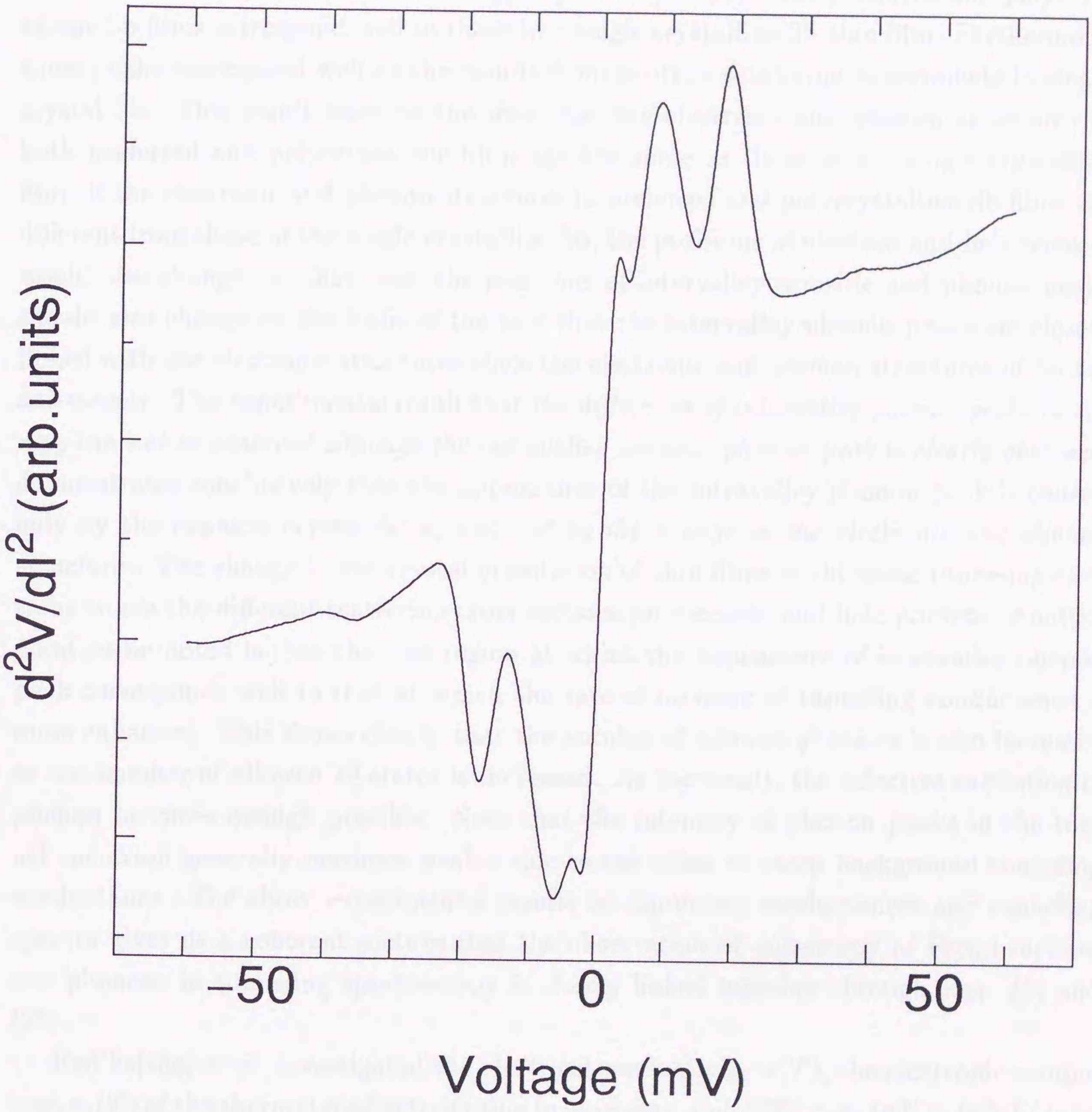

Figure 35: Second-derivative tunneling spectra of Al-Al oxide-Sb tunnel junction measured at 4.2 K. The Sb is "polycrystalline".

pocket the transition occurs); this is probably due to the anisotropic (lower-symmetrical) locations of electron and hole Fermi pockets (that is, the tunnel transition into identified pockets is impossible for Sb).

It is noteworthy that all the intervalley phonon peaks in both preferred and polycrystalline Sb films correspond well to those in a single crystalline Sb thin film. Furthermore, these peaks correspond well to the results from neutron scattering experiments in single crystal Sb. This result leads to the idea that the electronic and phonon structures in both preferred and polycrystalline films are the same as those in the single crystalline film. If the electronic and phonon structures in preferred and polycrystalline Sb films are different from those of the single crystalline Sb, the positions of electron and hole pockets would also change. In that case, the positions of intervalley acoustic and phonon peaks should also change on the basis of the fact that the intervalley phonon peaks are closely linked with the electronic structures since the electronic and phonon structures of Sb are anisotropic. The experimental result that *the difference of intervalley phonon peaks in energy can not be observed although the intravalley acoustic phonon peak is clearly observed*, demonstrates conclusively that the appearance of the intravalley phonon peak is caused only by the exposed crystal faces, and *not by the change in the electronic and phonon structures.* The change in the crystal orientation of thin films could cause tunneling electrons to see the different scattering cross sections for electron and hole pockets. Another point to be noted is that the bias region at which the appearance of intravalley phonon peak corresponds well to that at which the rate of increase of tunneling conductance is more enhanced. This shows clearly that the number of allowed $q^{||}$ states is also increased as the number of allowed $k^{||}$ states is increased. As the result, the selective excitation of phonon becomes enough possible. Note that the intensity of phonon peaks in the tunnel spectrum generally becomes weaker due to the effect of steep background tunneling conductance. The above experimental results for tunneling conductances and tunneling spectra gives us a coherent picture that the observation of anisotropy of Fermi surfaces and phonons in tunneling spectroscopy is closely linked together through Eqs. (5) and (25).

Red'ko[188] *et al.* investigated the electrical conductivity $\sigma(T)$, the electronic component $\kappa_e(T)$ of the thermal conductivity due to electrons, and $L(T) = \kappa_e/\sigma T = (\pi^2 k_B^2/3e)\times \left(\tau^T_{E_F}/\tau^E_{E_F}\right)$ to obtain information on the electron scattering mechanism in Sb. If the carriers in a metal are scattered by phonons then its σ, κ_e, and the relation between σ and κ_e change with temperature in the following way. At a temperature T high in comparison to the Debye temperature Θ, where all of the phonons are excited, which can interact with the current carriers, then: 1) $\sigma \sim T^{-1}$, 2) $\kappa_e \sim T^0 = \text{const}$, and 3) the Wiedemann-Franz law $\kappa_e/\sigma T = L_0$ is fulfilled, where the Lorenz number L_0 is a universal constant:

$$L_0 = \frac{\pi^2}{3}\left(\frac{k_B}{e}\right)^2 = 2.44 \times 10^{-8} V^2/deg^2,$$

while σ and κ_e differ by factors of a hundred for different metals. In this case the electron scattering is elastic and the relaxation of the electron distribution function f is characterized by a time τ, independent of the deviation of f from equilibrium due to the *electric or temperature fields* ($\tau_\sigma = \tau_{\kappa_e}$). With $T < \Theta$, where one begins to "measure" the large wave vector phonons, the ability to scatter an electron by a large angle and the momentum relaxation of f are slowed because: 1) σ begins to grow rapidly with decreasing T (theoretically in the simplest case $\sigma \sim T^{-5}$); 2) there is also an increase of κ_e although not so fast (theoretically in the simplest case $\kappa \sim T^{-2}$) since relaxation of the function f displaced from equilibrium by the temperature field can also arise from thermal small-wave vector phonons, which even during small-angle electron scattering always effectively equilibriate their energies; 3) the indicated difference in the rate at which f relaxes (when it is displaced from equilibrium by either an electric or temperature field) means that with $T < \Theta$ the phonon scattering becomes inelastic, $\tau_\sigma > \tau_{\kappa_e}$, an the Lorenz number L will cease to be a universal constant and will decrease with decreasing temperature (theoretically as $L \sim T^2$) until impurity scattering comes into play, which is elastic. With the increasing role of impurity scattering $L(T)$ passes throughout a minimum and begins to increase up to the initial value L_0. It can be seen from their data that for Sb with $T > 25$ K neither $\sigma(T)$ nor $\kappa_e(T)$ follows the regularities expected with $T > \Theta^*$ where Θ^* is the above effective Debye temperature for the electron-intravalley acoustic phonon interaction determined by the Fermi energy, while the curve is lower than L_0, which, in view of the degeneracy of the carriers, indicate an inelastic scattering mechanism already with $T \leq 100$ K. *The two minima on the curve $L(T)$ indicate the existence of two inelastic scattering mechanisms with two values Θ_1^* and Θ_2^*.* One of them occurs with $T < 10$ K, i.e., with $T < \Theta_1^* \simeq 2.2$ meV and is due, one might suppose, to the measuring of the phonons which can scatter carriers by large angles within the Fermi surface of one ellipsoid (intravalley acoustic phonon scattering). The rise on this part of the curve with $T < 4$ K is due to the growing role of elastic impurity scattering. The other inelastic impurity scattering mechanism, which appears in $L(T)$ between 100 and 10 K, can be due to intervalley acoustic phonon scattering with Umklapp scattering phonon processes between different ellipsoids. Such Umklapp processes should involve participation by larger wave vector phonons with higher values of Θ^*. From their experimental data on $\kappa_e(T)$, $\sigma(T)$, and $L(T)$, $\Theta_2^* = 8.6$ meV, which corresponds approximately to the theoretical estimate which can be gotten from the model of the Sb spectrum[189] and is the effective Debye temperature for intervalley acoustic phonon scattering. The investigation of the Lorenz number thus gives us some information on the dominant electron-phonon scattering mechanisms in certain temperature regions.

Moreover, being common to the tunneling spectra of the above three types, the overtone optical phonon peak shows an asymmetric band structure. From a comparison of the Sb overtone phonon tunneling spectrum with previously reported phonon density of states[183, 185, 187], it finds out that the symmetry of the tunneling spectrum is opposite to that of the reduced Raman spectrum and that it is similar to that of the theoretical phonon density of states. The slope of the peak in both the tunnel spectrum and the theoretical phonon density of states becomes steeper at the higher energy side, on the other hand, that in the reduced Raman spectrum becomes steeper at the lower energy side. It is noted that the behavior of the overtone phonon peak is common to all three kinds of spectra. The detailed theoretical calculations for both "bare" phonon density of states $F(\omega)$ and "electron (or photon in Raman spectra) - phonon coupling function weighted" phonon density of states $\alpha^2 F(\omega)$ are at present completely lacking for the semimetal. The above comparison, however, would provide qualitative information about the electron-phonon coupling in Sb. It is understood that the coupling function $\alpha^2_{Raman}(\omega)$ in the Raman spectrum would change rapidly at lower energy, but that in the tunneling spectrum the coupling function $\alpha^2_{tunnel}(\omega)$ would change rapidly at higher energy[183, 185, 187]. Such an asymmetry in the overtone phonon peak was not observed in the point contact spectra of Sb by Yanson *et al.*[192]. This might be due to the difference in the energy dependence of the electron-phonon coupling function for the tunneling spectroscopy and the PCS. But clear explanation for such differences in the coupling function remains open.

4.3 Disorder Induced Semimetal-Metal Transition: A Tunneling Study

The metal-insulator transition has been a subject of study for the last decade and much progress has been made in understanding the physics in disordered materials[196]. In a disordered material the electron motion is diffusive, hence, the electron screening is retarded and the Coulomb interactions among electrons are enhanced. The electronic properties of weakly disordered metal at low temperatures are governed by the effect of long-range electron-electron interaction, which leads to a correction of the $N(E)$. Tunneling anomalies in the $N(E)$ have been widely observed in amorphous (magnetic) alloys[44, 46, 197], granular metals[198], doped semiconductors[199], and weakly disordered metals[74, 83]. But, for example, granular metals include essentially a correlated system of rather regularly alternating metallic and insulating regions[200]. More attention has been paid to much more complicated and interesting structures, which would occur when the random solid mixture appears as a result of an aggregation process or of a phase transition in some parts of the sample[201]. For the latter case, it is well known that inhomogeneous Sb films can be prepared as the random mixture of amorphous and crystalline phase - a collection of amorphous spots of Sb embedded in an otherwise semimetallic film - by the deposition under high evaporation rate[202, 203]. In contrast to the quantum correction due to weak localization and electron-electron interaction in disordered metals which seems well established, tunneling experiments have not been almost made on the electron-electron correlation in disordered *semimetals*. The theory of Altshuler and Aronov is for single-carrier, single-valley metallic systems, with no accounting being taken of the existence of two-carriers (electrons and holes) and intervalley scattering between separate volumes in momentum space, which occurs in semimetals. It has not been clear whether the above mentioned theory is valid for such a minor carrier system. From the above points of view, electron tunneling experiments on inhomogeneous Sb films have been performed[204].

In Fig. 36 the typical differential tunneling conductance $G(V)$ vs. voltage curves at 4.2 K are shown. Negative bias corresponds to raising the Fermi level of the Sb with respect to that of the Al. For the curve of Fig. 36 (a) of the polycrystalline film, the $G(V)$ shows structures at voltages corresponding to the band edges of the Sb as in usual metal-oxide-semimetal tunnel junctions[180, 181]. On the other hand, the curve of Fig. 36 (b), which was measured for the inhomogeneous film, shows an anomaly with a minimum at the Fermi energy and symmetrical around zero voltage. First, it is examined whether this zero bias anomaly can be interpreted in terms of the theory of electron-electron interaction in weakly disordered metals. Altshuler and Aronov theory provides a framework of quantitative analysis[69, 70]. As described previously, the behavior of corrections of the $N(E)$ for three-dimensional and two-dimensional disordered metals are square-root and logarithmic, respectively. For a given thickness of the film a dimensional crossover occurs as a function of the energy of the electrons. For low energies the $N(E)$ behavior is logarithmic and is square-root for higher voltages. A critical energy separates the two dependencies. The tunneling conductance near zero voltage is shown as a function of $\sqrt{e|V|}$ in Fig. 37, and as a function of $\ln(e|V|/E_0)$, ($E_0 = 1$ meV) in Fig. 38. From the figures it finds out that the measured $G(V)$ behavior yields a good agreement to the theory. The voltage dependence of the tunneling conductance for the film investigated here is logarithmic for low voltages and square-root for higher voltages. The experimentally observed critical energy is about 5 meV. The square-root behavior can be obtained up to about 25 meV. This value is comparable to those observed in disordered metal films[82]. The logarithmic $G(V)$ dependence for low voltages can be clearly observed except the thermal smearing of the Fermi level. From the above examination we can see that the $G(V)$ behavior in inhomogeneous Sb films can be well interpreted in the framework of the Altshuler and Aronov theory.

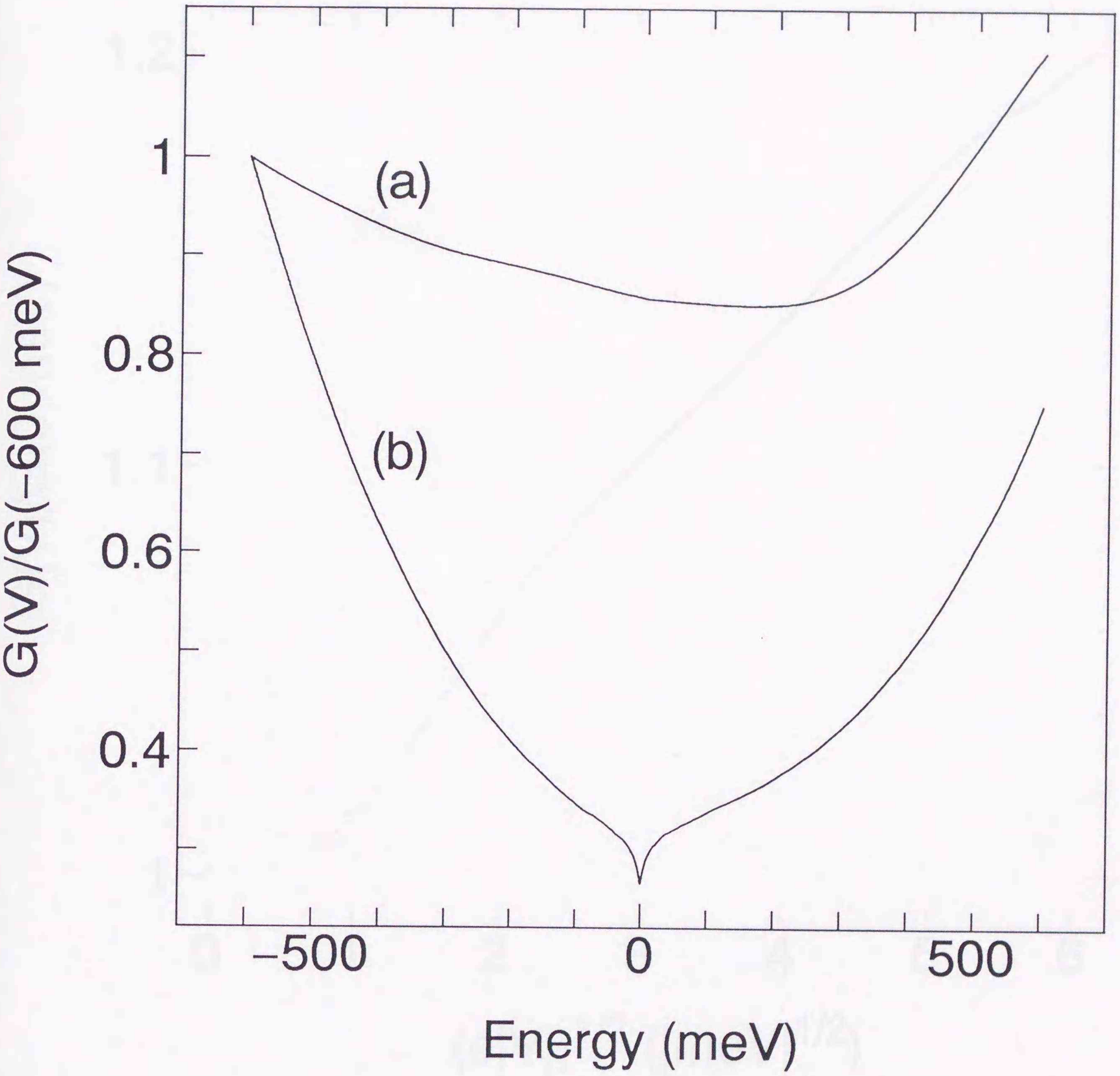

Figure 36: Tunneling conductance $G(V)/G(\text{-600 meV})$ vs. energy for junctions with (a) polycrystalline and (b) inhomogeneous Sb films at 4.2 K.

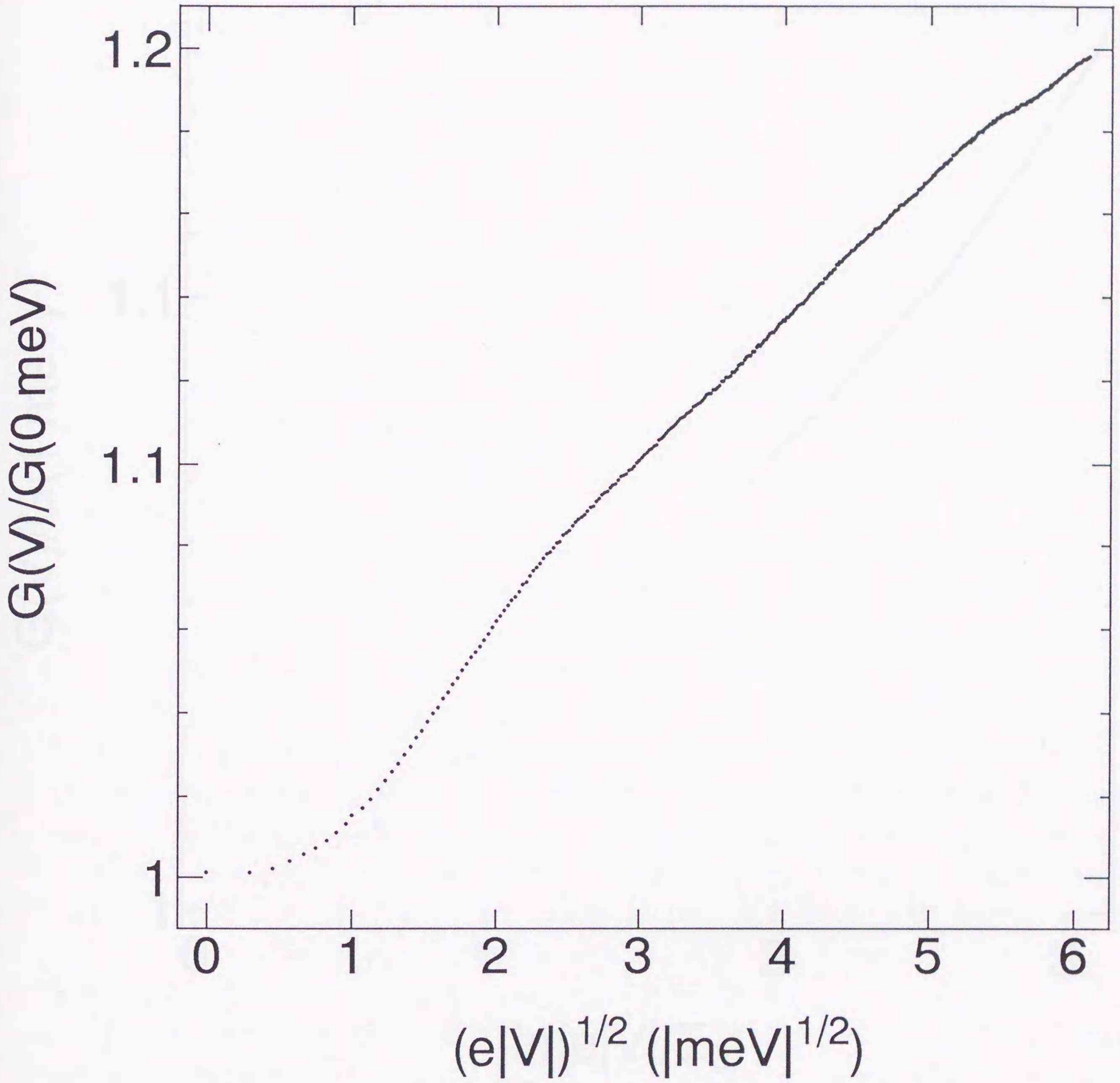

Figure 37: Normalized tunneling conductance $G(V)/G(0 \text{ meV})$ vs. $(e|V|)^{1/2}$ for the inhomogeneous Sb film.

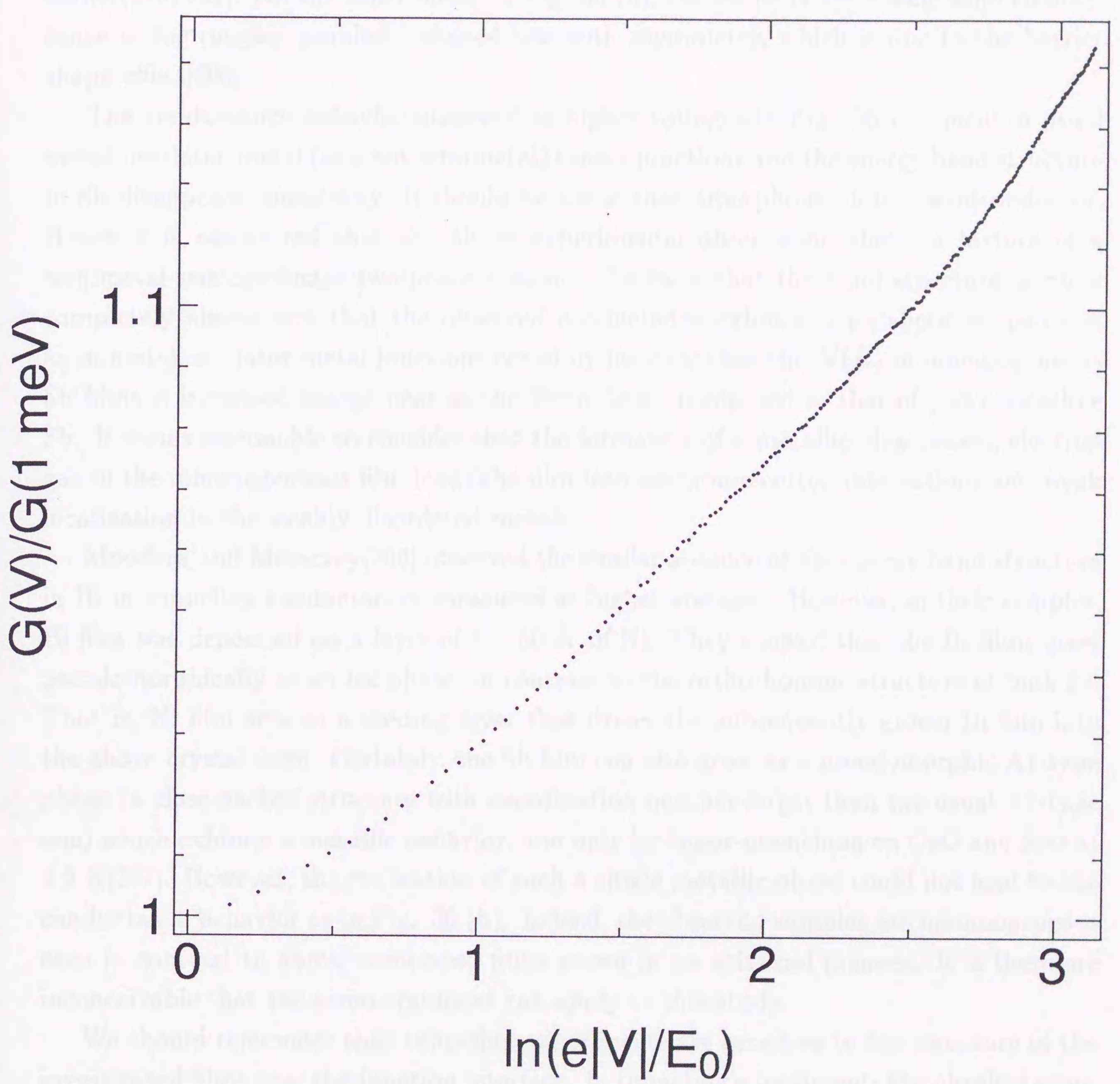

Figure 38: Normalized tunneling conductance $G(V)/G(1\text{ meV})$ vs. $\ln(e|V|/E_0)$ ($E_0 = 1$ meV) for the inhomogeneous Sb film.

Next the $G(V)$ behavior at higher voltages is considered. In Fig. 36 (a) a major conductance bump is observed at -180 meV and the conductance increases almost linearly between 400 and 600 meV. The conductance behavior agrees well with those observed earlier[180, 181]. On the other hand, in Fig. 36 (b), the shape of the background conductance is the roughly parabolic-shaped one with asymmetry, which is due to the barrier shape effect[205].

The conductance behavior observed at higher voltages in Fig. 36 is typical in usual metal-insulator-metal (and not semimetal) tunnel junctions and the energy band structure in Sb disappears completely. It should be noted that amorphous Sb is a semiconductor. Hence it is considered that the above experimental observation shows a feature of a semimetal-semiconductor two-phase system. The facts that the band structure in Sb is completely absent and that the observed conductance exhibits a parabolic shaped one as in metal-insulator-metal junctions certainly indicate that the $N(E)$ in inhomogeneous Sb films is increased except near at the Fermi level, compared to that of polycrystalline Sb. It seems reasonable to consider that the formation of a metallic, degenerate, electron gas in the inhomogeneous film leads the film into electron-electron interactions and weak localization in the weakly disordered metals.

Moodera and Meservey[206] observed the similar absence of the energy band structure in Bi in tunneling conductances measured at higher voltages. However, in their samples, Bi film was deposited on a layer of 1 – 50 Å of Ni. They showed that the Bi films grow pseudomorphically as an fcc phase, in contrast to the orthorhombic structure of bulk Bi. That is, Ni film acts as a seeding layer that drives the subsequently grown Bi film into the above crystal form. Certainly, the Sb film can also grow as a pseudomorphic A1-type phase (a close-packed structure with coordination number larger than the usual A7-type one) which exhibits a metallic behavior, and only by vapor-quenching on CaO and SrO at 4.2 K[207]. However, the realization of such a single metallic phase could not lead to the conductance behavior as in Fig. 36 (b). Indeed, the observed samples are inhomogeneous ones in contrast to above mentioned films grown in an epitaxial manner. It is therefore inconceivable that the same argument can apply to this study.

We should remember that tunneling experiments are sensitive to the structure of the investigated films near the junction interface. In tunneling experiments the physical properties of the investigated films are probed by tunneling electrons only within the sampling depth from the interface. The sampling length is small in disordered materials. On the other hand, the metastable phase of the metal usually exist only at low temperatures or high pressures[208], but may also exist in extremely disordered regions[209], which will be most obtained in the vicinity of the junction interface in this study. This result therefore seems to suggest that an unknown metastable metallic phase of Sb exists at the junction

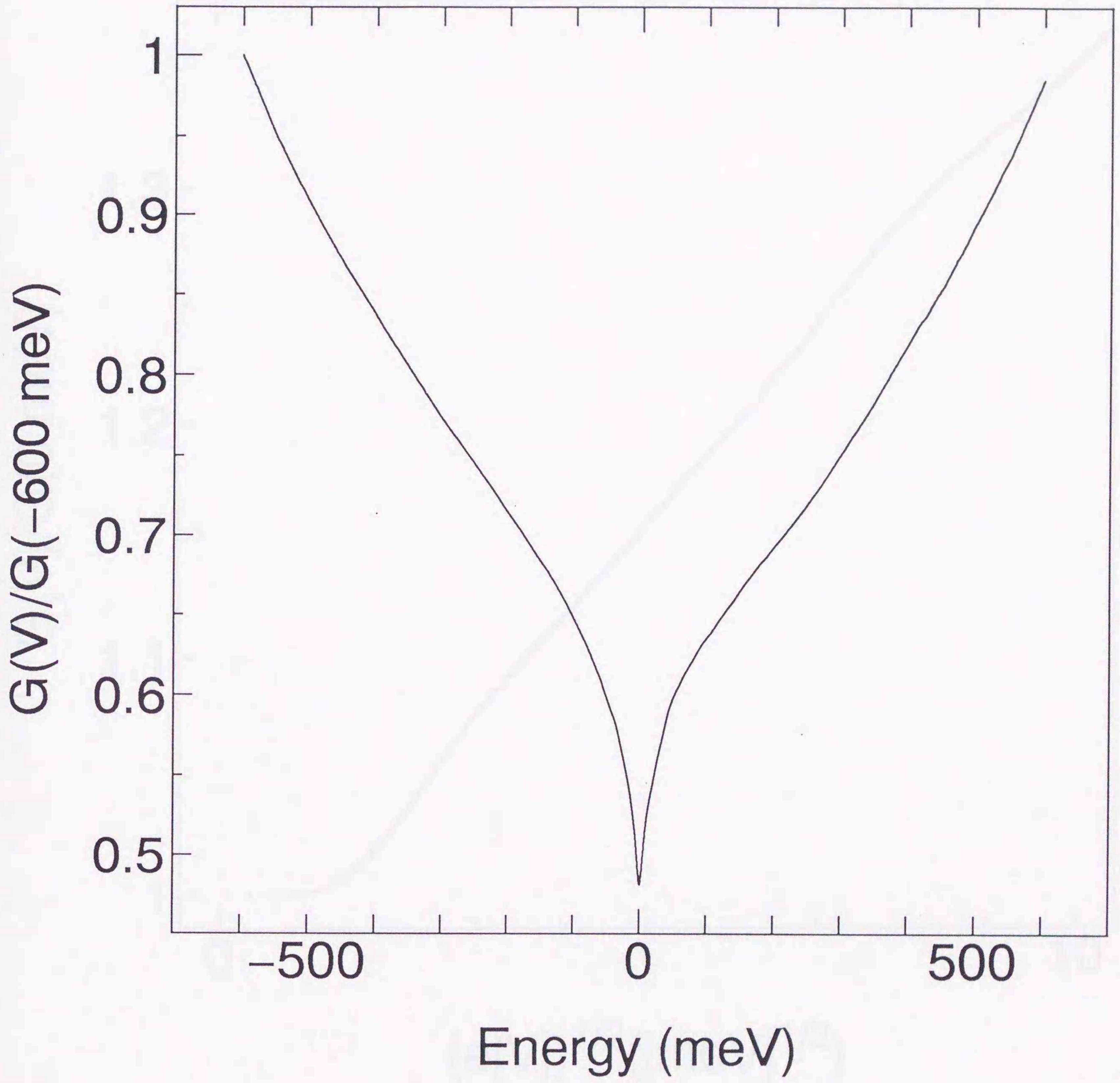

Figure 39: Tunneling conductance $G(V)/G(\text{-}600\ \text{meV})$ vs. energy for another typical junction with inhomogeneous Sb film at 4.2 K.

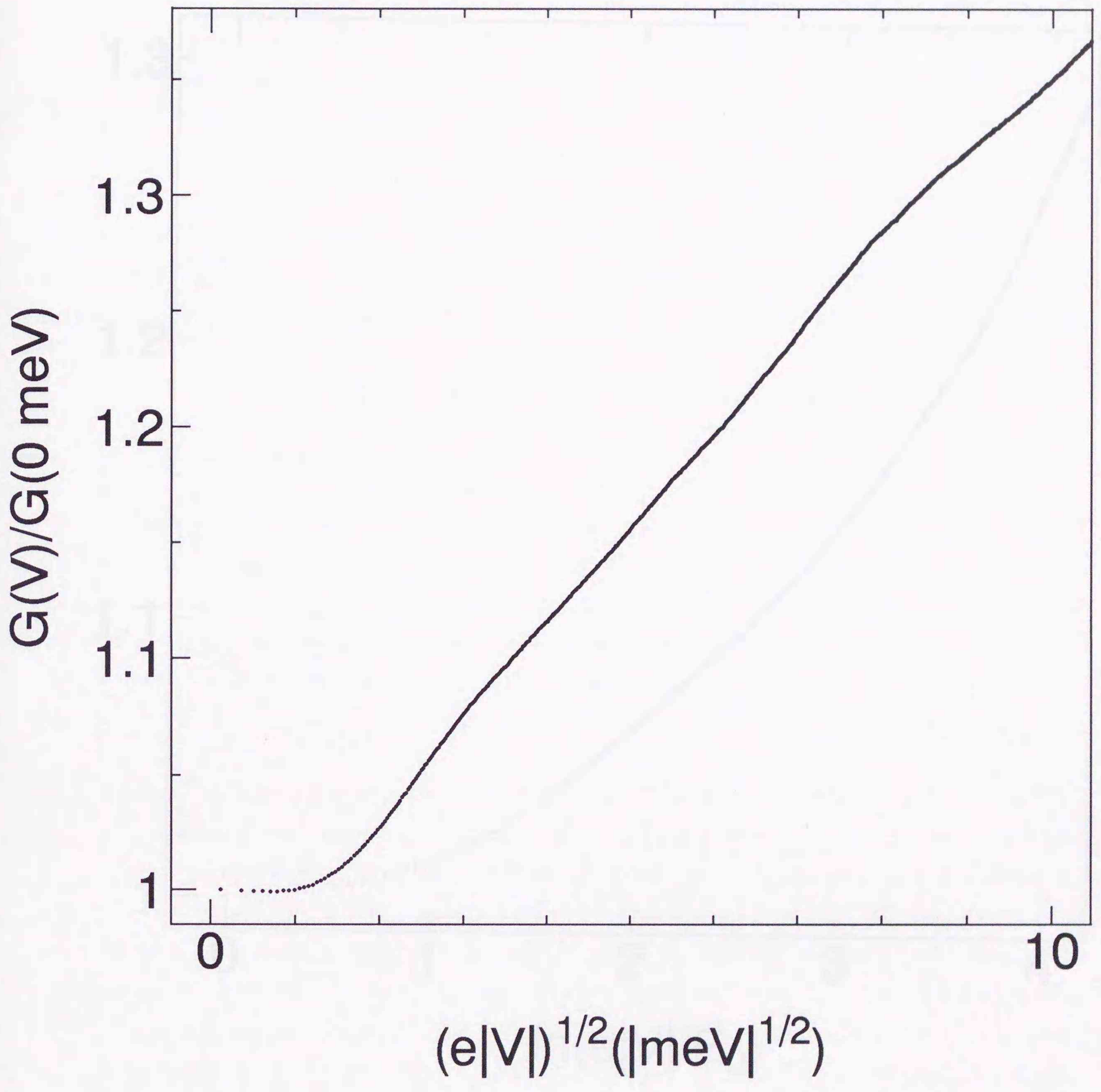

Figure 40: Normalized tunneling conductance $G(V)/G(0\ \mathrm{meV})$ vs. $(e\,|V|)^{1/2}$ for the inhomogeneous Sb film.

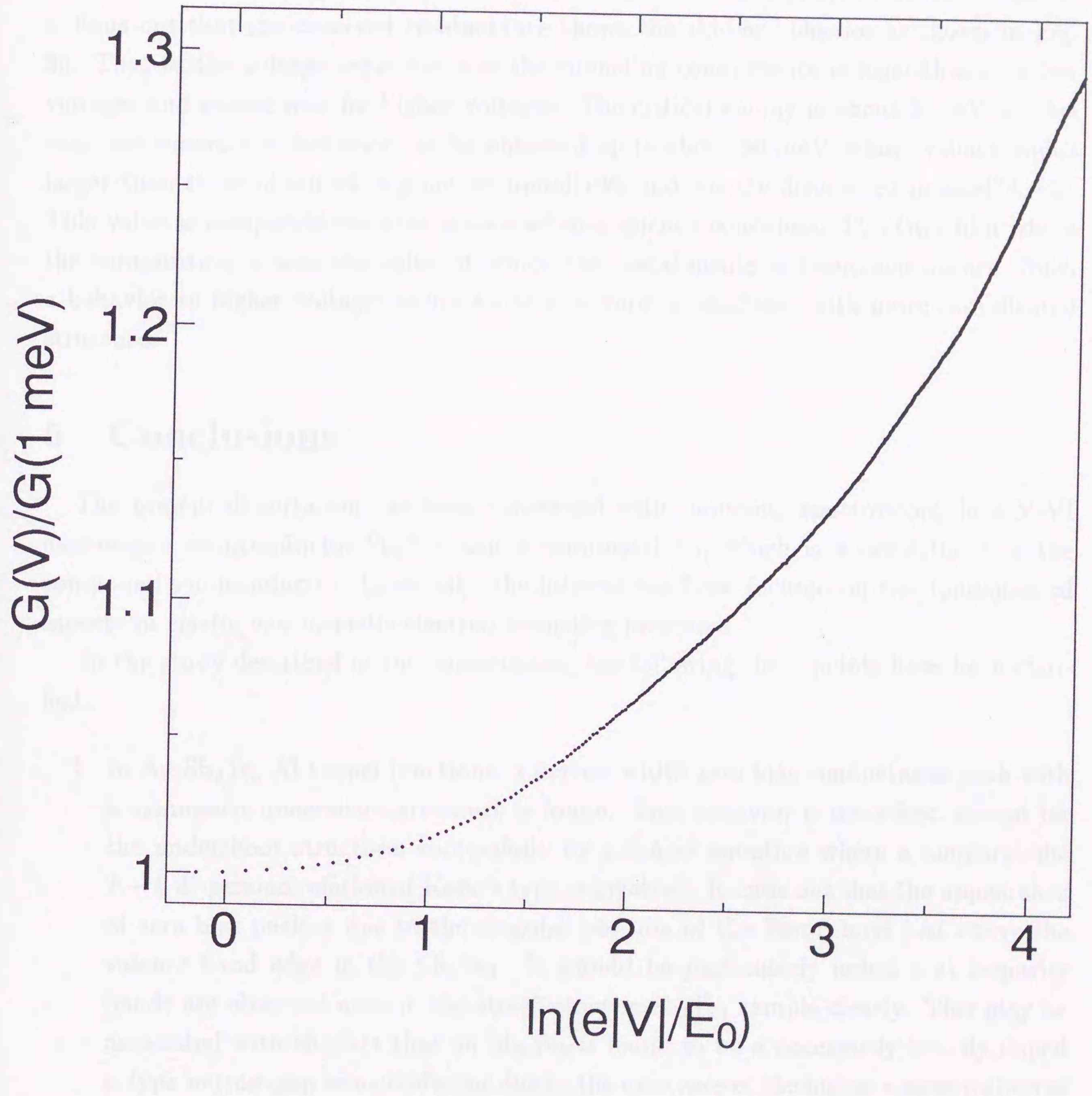

Figure 41: Normalized tunneling conductance $G(V)/G(1\text{ meV})$ vs. $\ln(e|V|/E_0)$ ($E_0 = 1$ meV) for the inhomogeneous Sb film.

interface due to disorder induced semimetal-metal transition.

Fig. 39 shows another typical tunneling conductance vs. voltage curve at 4.2 K. The tunneling conductance near zero voltage is shown as a function of $\sqrt{e|V|}$ in Fig. 40, and as a function of $\ln(e|V|/E_0)$, ($E_0 = 1$ meV) in Fig. 41, respectively. From these figures, it finds out that the observed conductance shows the similar behavior as shown in Fig. 36. That is, the voltage dependence of the tunneling conductance is logarithmic for low voltages and square-root for higher voltages. The critical energy is about 5 meV. In this case, the square-root behavior can be obtained up to above 60 meV, whose value is much larger than those obtained in granular metal[198] and weakly disordered metals[74, 83]. This value is comparable to that measured in a quench-condensed $Tl_{0.7}Te_{0.3}$ film where the composition is near the value at which the metal-insulator transition occurs. Such a behavior to higher voltages seems to be a feature in junctions with more complicated structures.

5 Conclusions

The present dissertation has been concerned with tunneling spectroscopy in a V-VI narrow-gap semiconductor Sb_2Te_3 and a semimetal Sb, which is a constituent of the compound semiconductor. Especially, the interest has been focused on two fundamental aspects in *elastic and inelastic* electron tunneling processes.

In the study described in this dissertation, the following three points have been clarified.

1. In Au-Sb_2Te_3-Al tunnel junctions, a narrow width zero bias conductance peak with a symmetric undershoot structure is found. This behavior is described, except for the undershoot structure, successfully by a tunnel equation where a nonparabolic $E-k$ dispersion relation of Kane's type is involved. It finds out that the appearance of zero bias peak is due to the singular position of the Fermi level just above the valence band edge in the Sb_2Te_3. It should be particularly noted that impurity bands are observed even in the stoichiometric Sb_2Te_3 sample clearly. This may be associated with the fact that an Sb_2Te_3 is found to be a necessarily heavily doped p-type narrow-gap semiconductor due to the existence of the higher concentration of antisite defects. The observed conductance behavior demonstrates the significance of the dispersion relation in the tunneling barrier when we analyse a tunneling phenomenon through a solid with conduction- and valence bands.

2. Electron tunneling measurements have been carried out to investigate the confirmed anisotropy of Fermi surfaces and phonons in tunneling spectroscopy. Depending

upon the texturization of antimony films, the systematic change in the shape of the tunneling conductance is observed. As well as the intervalley acoustic and optical phonon peaks, the appearance of the intravalley acoustic phonon peak is found in the second derivative curve. This is the first observation of the intravalley phonon peak in tunneling spectroscopy, and of the anisotropy of Fermi surfaces and phonons in tunneling spectroscopy. The overtone phonon peak exhibits an asymmetric structure contrary to that of the Raman spectrum. This asymmetry has not been observed in point contact spectroscopy. This fact suggests that the coupling constant $\alpha_T^2(\omega)$ is different from the $\alpha_{PC}^2(\omega)$. It is important to note that the tunneling spectroscopy and the point contact spectroscopy can be distinguished from each other clearly.

3. In tunneling measurements on inhomogeneous antimony thin films, tunneling conductance shows a minimum at zero bias. This behavior can be explained by the theory of the electron-electron interaction in weakly disordered metals. At higher voltages the background tunneling conductance curve is almost parabolic with asymmetry, typical in a metal-insulator-metal tunnel junction and the band structure in the semimetal disappears completely. The formation of a metallic, degenerate electron gas in an inhomogeneous Sb film therefore seems to lead the observed behavior. The realization of the metallic, degenerate electron gas could be occurred under the existence of a higher disorder at the interface of the junction. The observed tunneling conductance behavior is of quite interest in that it is observed as the result of the *disorder induced semimetal-metal transition* in the film.

Acknowledgments

The author would like to express his most earnest words of gratitude to Prof. Kōichi Mukasa for his provision of insightful guidance and generous support during all phases of this study with which this dissertation has been successfully accomplished.

He also acknowledges Prof. Masayuki Ikeda, Prof. Akira Okada, and Prof. Takashi Fukui for their valuable suggestions.

The author is deeply indebted to Prof. R. Aoki for stimulating and helpful discussions about tunneling spectroscopy and for the considerable assistance to obtain McMillan programs through Prof. Ginsberg. He gave me remarkable insight into the tunneling spectroscopy.

Sincere thanks are due to Mr. Jiro Nagao for valuable discussions and for considerable assistance with X-ray and EPMA measurements. He is also deeply indebted to Mr. Fumikazu Kiya for supplying the Sb_2Te_3 *samples and for informative discussions.*

He extends his thanks to colleagues, students, and personnel at Nanoelectronics Laboratory for their creating a harmonious environment during his study.

The author on a personal level expresses a deferential and heartfelt appreciation to his wife, Sumie Hatta and to his parents, Seiji Hatta and Eiko Hatta, for their continuous encouragement and resilient harmony.

He would also like to sincerely thank my friend, Michael Haas for his wonderful friendship. The advice and encouragement that the author has continuously received from him have been of valuable and has greatly enjoyed the many conservations they have shared.

Appendix: The Quantum Size Effect in Tunneling to Probe the Band Structures of Materials

We consider the possibility of using the quantum size effect in tunneling to probe the features of the band structure along different directions in the Brillouin zone (i.e., the band anisotropy) clearly[210, 211, 212]. When the mean free path of the tunneling electrons becomes comparable with the distance between the boundaries of the investigated film, one has to take size effects into account. The basis of the effects described below is the quantization energy levels in thin films and interference between electron waves reflected from the film boundaries. When certain specific conditions are satisfied, the tunnel conductance exhibits a system of equidistant maxima and the separation between them (oscillation period) determines the velocity of carriers, whereas the nature of attenuation of these maxima carries information on some parts in the energy band structure of a metal and on the state of the surface of a film.

The simplest of the size effects is the formation of electron waves in a thin film of thickness d regarded as a potential box. Interference between two electron states with the momenta p_x and $-p_x$ gives rise to quantum energy levels in the spectrum of the film:

$$E = E\left(n\frac{\pi\hbar}{d}, p_y, p_z\right), \tag{69}$$

here n is an integer, $p = 2\pi\hbar/\lambda_F$, and λ_F is the de Broglie wavelength.

Observation of such quantized energy levels is possible if the irregularities of the film surface are small compared with the de Broglie wavelength. The most convenient objects for such investigations are naturally semiconductors and semimetals characterized by a low Fermi energy and a long electron wavelength. Therefore the first reliable experimental proof of the existence of the quantum size effect was reported for bismuth, which is characterized by $E_F \sim 10^{-2}$ eV and $\lambda_F \sim 10^{-5}$ cm[213]. In the case of metals, the Fermi energy is high, $E_F \sim 10$ eV, the de Broglie wavelength is of the order of one interatomic distance $a \sim 10^{-8}$ cm. This seems to be beyond the possibility of the investigations of the effects. Nevertheless, the quantum size effect in metals has been observed[210, 211].

For the purpose of understanding the quantum size effect in metals, it is important to remember that the thickness of real metals varies in discrete steps amounting to one lattice parameter a: $d = Na$ (N; an integer, a: the lattice parameter in the tunneling direction). In fact, metal films consist of many blocks of different thickness and with a perfect crystal structure. Such an experimentally unavoidable inhomogeneity of the films naturally hinders the observation of the quantum size effect, because each block or crystallite, depending on its thickness, has its own sets of energy conditions,

$$p_x^n = n\frac{\pi\hbar}{d}; \tag{70}$$

here x is the normal to the surface of the sample coinciding with the direction of the tunneling current. However, because d is discrete, there are always special points in the band structure which correspond to the so-called "commensurate" levels for which the electron wavelength is an integral multiple of the crystal lattice constant in the tunneling direction. These commensurate levels are common to a large number of different crystallites of different thicknesses in a film. For example, an electron state with the momentum projection $p_x = \pi\hbar/2a$ will be a resonance state for any block with an even value of N, because we can always find such a value of $n = N/2$ that

$$p_x^n = \frac{\pi\hbar}{a}\frac{n}{N} = \frac{\pi\hbar}{2a}. \tag{71}$$

The main contribution to the tunneling comes from electrons with energy $E_{1/2} = (\pi\hbar/2a)$ $(v_g/2)$ (v_g: the group velocity) and there is almost specular reflection of the quasiparticles [214]. The dependences of the differential tunneling conductance, $\mathrm{d}^2V/\mathrm{d}I^2$ on the voltage V for junctions are expected to show an oscillatory structure with equally spaced peaks $(\Delta E = \pi\hbar v_g/d)$ due to the combined contribution to the tunneling current of quantum levels of different crystallites in the film. We can see that an experimental investigation of the quantum size effect makes it possible to determine the values of some of the special points in the band structure of a metal and the group velocity of electrons at these points. The center of the oscillation structure is located at $U = E - E_F$. The resonance electron levels adjoining E decay rapidly away from E. The subsidiary peaks in the spectrum are damped compared to this central maximum. This damping is due to the distribution of the crystallite thicknesses. The period of the structure varies with the film thickness but its center remains fixed and corresponds to electronic states with $p_x = \pi\hbar/2a$ in the tunneling direction in the Brillouin zone. An analytic description of the oscillations of the current was obtained[215].

We consider the conditions for investigations of quantum size effect. The local deviations of a film thickness must be not greater than the Fermi wave length of the electrons. Real films under investigations are usually not as smooth as one assumes in the potential box model. The surface roughness, characterized by its amplitude, h, therefore influences the observation. Another difficulty of observing the size quantization results from the scattering of electrons at the film surface. Electrons which are inelastically (diffusely) scattered at the surface do not follow the k_x-quantization. At least a fraction p of the free electrons has to be specularly reflected from the surface. The specularity parameter p was introduced by Fuchs[216] to describe the thickness dependence of the conductivity due to a thickness dependence of the mean free path (size effect). This gives in principle the possibility to determine the electron reflectivity parameter from conductivity measurements. A third distortion of the observation of size quantized states is brought in by volume scattering of the free electrons, which determines the mean free path, l_∞, or the relaxation time τ. The mean free path l_∞ has to be larger than the film thickness d. Finally the separation δE of the energy subbands has to be larger than the thermal broadening k_BT. If we introduce the band splitting ΔE_n

$$\begin{aligned}\Delta E_n &= E_{n+1} - E_n = \frac{\pi^2\hbar^2}{2m^*d^2}(2n+1),\\ E_n &\approx \frac{\pi^2\hbar^2}{m^*d^2}s \quad \text{for} \quad n \gg 1,\end{aligned}$$

the observation of the quantum size effect is restricted to:

thermal broadening

$$k_BT < \Delta E_n \tag{1}$$

lifetime broadening

$$\hbar/\tau < \Delta E_n \tag{2}$$

(which means $l_\infty > d$)
surface roughness

$$h \leq \lambda_F \tag{3}$$

and specularity parameter

$$p \neq 0. \tag{4}$$

The restrictions (1) and (2) can be easily met by investigations of very thin films at low temperatures. The restrictions (3) and (4) usually prevent the observation of quantum size states in metal films because they demand smoothness of the surface in atomic dimensions and specular reflection of the free electrons. The growth of films evaporated onto insulator substrates usually starts nucleation into islands which leads to a rough surface after the film becomes continuous. In addition, these polycrystalline films usually show rather diffuse scattering instead of specular reflection of the electrons. Reflection (3) is the most serious one. It demands samples with a large Fermi wavelength of the free electrons, as given for instance in semimetals and degenerated semiconductors. Therefore, the quantum size effects was first investigated with these materials.

It is expected that the energy band structure of a material can be probed along other crystallographic directions by a method postulating that thin metal films exhibit a *polytexture*[217], although the conditions for the appearance of polytextures are difficult to control. In this case the voltage dependence of $\mathrm{d}^2V/\mathrm{d}I^2$ can show a complex interference pattern formed by the superposition of electron standing waves produced by tunneling into regions of the film which are textured along different crystallographic directions and it can thus been demonstrated that the wide range of energies accessible by tunneling techniques can give qualitatively new information which is not available by other experimental methods.

References

[1] D. C. Tsui, in *Handbook on Semiconductors*, edited by T. S. Moss (North-Holland, Amsterdam, New York, Oxford, 1982), Vol. 1, edited by W. Paul, Chap. 11D, pp. 661-688.

[2] L. Esaki, Rev. Mod. Phys. **43**, 237 (1974).

[3] R. Meservey and P. M. Tedrow, Phys. Rep. **238** (4), 173-243 (1994).

[4] J. Geerk, Ph. D. thesis, Universität (TH) Karlsruhe, 1975.

[5] A. I. D'yachenko, Preprint No. 17, Physicotechnical Institute, Academy of the Ukrainian SSR, Donetsk, 1981.

[6] B. W. Nedrud, *Analysis of Superconducting Tunneling Data by McMillan's Method.* Tech. Rep. 217. University of Illinois, Urbana-Champaign, Department of Physics.

[7] V. M. Svistunov, M. A. Belogolovskii, and O. I. Chernyak. Sov. Phys. Usp. **30**, 1 (1987).

[8] R. Schneider, J. Geerk, and H. Rietschel, Europhys. Lett. **4** (7), 845 (1987).

[9] W. L. McMillan and J. M. Rowell, *Superconductivity*, edited by R. D. Parks (Marcel Dekker, New York, 1969), Vol. 1, Chap. 11.

[10] J. Geerk, in *Tunneling Phenomena in High and Low T_c Superconductors*, edited by Alessandro di Chiara and Maurizio Russo, (World Scientific, Singapore, 1993).

[11] J. P. Carbotte, Rev. Mod. Phys. **62** (4), 1027 (1990).

[12] J. M. Rowell, in *Tunneling Phenomena in Solids*, edited by E. Burstein and S. Lundqvist, (Plenum Press, New York, 1969), Chap. 20.

[13] Danny P. Shum, A. Bevolo, J. L. Staudenmann, and E. L. Wolf, Phys. Rev. Lett. **57**, 2987 (1986).

[14] A. Nowack, U. Poppe, M. Weger, D. Schweitzer, and H. Schwenk, Z. Phys. B **68**, 41 (1987).

[15] G. Ernst, A. Nowack, M. Weger, and D. Schweitzer, Europhys. Lett. **25**, 303 (1994).

[16] J. M. Rowell, IEEE Trans. Magn. **MAG-23**, 380 (1987).

[17] P. K. Hansma, Phys. Rep. **30**, 145 (1977).

[18] P. K. Hansma, *Tunneling Spectroscopy: Capabilities, Applications and New Techniques*, (Plenum, New York, 1982).

[19] J. Tomlin, Prog. Surf. Sci. **31**, 131 (1989).

[20] C. J. Adkins and W. A. Phillips, J. Phys. C **18**, 1313 (1985).

[21] J. Lambe and R. C. Jaklevic, in *Tunneling Phenomena in Solids*, edited by E. Burstein and S. Lundqvist, (Plenum Press, New York, 1969), Chap. 17.

[22] R. C. Jaklevic and J. Lambe, in *Tunneling Phenomena in Solids*, edited by E. Burstein and S. Lundqvist, (Plenum Press, New York, 1969), Chap. 18 .

[23] S. Gregory, Phys. Rev. Lett. **64**, 689 (1990).

[24] L. L. Chang, L. Esaki, and R. Tsu, Appl. Phys. Lett. **24**, 593 (1974).

[25] E. L. Wolf, in *Solid State Physics*, edited by H. Eherenreich, F. Seitz and D. Turnbull (Academic, New York, 1975), Vol. 30, 1.

[26] E. L. Wolf, Rep. Prog. Phys. **41**, 1439 (1978).

[27] S. Gregory, Phys. Rev. Lett. **68**, 2070 (1992).

[28] E. L. Wolf, *Principles of Electron Tunneling Spectroscopy*, (Oxford, New York, 1985).

[29] R. Chicault and J. C. Villegier, Phys. Rev. B **36**, 5215 (1987).

[30] R. Chicault and Y. Joly, Phys. Rev. B **42**, 11655 (1990).

[31] J. P. Eisenstein, L. N. Pfeiffer, and K. W. West, Phys. Rev. Lett. **69**, 3804 (1992).

[32] H. Cao, G. Klimovitch, G. Björk, S. Pau, and Y. Yamamoto, Appl. Phys. Lett. **70**, 1986 (1997).

[33] A. Dargys and A. Natulionis, Solid State Electron. **31**, 717 (1988).

[34] A. Dargys, S. Žurauskas, and Žurauskiene, Appl. Phys. A **52**, 13 (1991).

[35] G. Fischer and H. Hoffmann, Z. Phys. B **39**, 287 (1980).

[36] P. A. Badoz, F. Arnaud d'Avitaya, and E. Rosencher, Ann. Phys. **16**, 623 (1991).

[37] F. E. Vopat, T. S. A. Lai, and W. J. Tomasch, Phys. Rev. B **35**, 3243 (1987).

[38] I. Giaever and H. R. Zeller, Phys. Rev. Lett. **20**, 1504 (1968).

[39] H. R. Zeller and I. Giaever, Phys. Rev. **181**, 789 (1969).

[40] J. Lambe and R. C. Jaklevic, Phys. Rev. Lett. **22**, 1371 (1969).

[41] J. B. Barner and S. T. Ruggiero, Phys. Rev. Lett. **59**, 807 (1987).

[42] S. T. Ruggiero and J. B. Barner, Z. Phys. B **85**, 333 (1991).

[43] J. König, H. Schoeller, and G. Schön, Phys. Rev. Lett. **76**, 1715 (1996).

[44] W. L. McMillan and J. Mochel, Phys. Rev. Lett. **46**, 556 (1981).

[45] J. G. Massey and Mark Lee, Phys. Rev. Lett. **77**, 3399 (1996).

[46] E. Hatta, M. Tonokawa, J. Nagao, and K. Mukasa, Solid State Commun. **102**, 437 (1997).

[47] A. Fournel, J. P. Sorbier, M. Konczykowski, and P. Monceau, Phys. Rev. Lett. **57**, 197 (1975).

[48] J. P. Sorbier, H. Tortel, C. Schlenker, and H. Guyot, J. Phys. I France **5**, 221 (1995).

[49] J. P. Sorbier, H. Tortel, P. Monceau, and F. Levy, Phys. Rev. Lett. **76**, 676 (1996).

[50] H. Bando, K. Kajimura, H. Anzai, T. Ishiguro, G. Saito, Mol. Cryst. Liq. Cryst. **119**, 41 (1985).

[51] S E. Brown, G. Mozurkewich, and G. Grüner, Phys. Rev. Lett. **52**, 2277 (1984).

[52] T. Ekino, T. Takabatake, H. Tanaka, and H. Fujii, Phys. Rev. Lett. **75**, 4262 (1995).

[53] S. Kunii, Sov. J. Low. Temp. Phys. **18**, 343 (1992).

[54] J. Aarts and A. P. Volodin, Physica B **206-207**, 43 (1998).

[55] G. Güntherodt, W. A. Thompson, and F. Holtzberg, Phys. Rev. Lett. **49**, 1030 (1982).

[56] S. Kunii and O. Kagaya, J. Magn. Magn. Mater. **52**, 165 (1985).

[57] J. P. Eisenstein, L. N. Pfeiffer, and K. W. West, Phys. Rev. Lett. **69**, 3804 (1992).

[58] C. T. Rogers and R. A. Buhrman, Phys. Rev. Lett. **55**, 859 (1985).

[59] Sh. Kogan, *Electronic noise and fluctuations in solids*, (Cambridge University Press, Cambridge,1996).

[60] W. Franz, in *Handbuch der Physik*, edited by S. Flugge, (Springer-Verlag, Berlin, 1956), pp. 205, Vol. 17.

[61] K. H. Gundlach, in *FESTKÖRPER PROBLEME* (*ADVANCES IN SOLID STATE PHYSICS*), edited by O. Madelung (Pergamon, 1971), Vol. 11; J. Appl. Phys. **44**, 5005 (1973).

[62] H. Wehr and K. Knorr, Z. Phys. B **33**, 21 (1979).

[63] L. Esaki, Phys. Rev. **109**, 603 (1958).

[64] L. Chang, P. J. Stiles, and L. Esaki, J. Appl. Phys. **38**, 4440 (1967).

[65] J. W. Conley and J. J. Tiemann, J. Appl. Phys. **38**, 2880 (1967).

[66] C. B. Duke, *Tunneling in Solids*, (Academic, New York, 1969), pp. 108.

[67] P. Guetin and G. Schreder, Phys. Rev. B **6**, 3816 (1972).

[68] P. W. Anderson, Phys. Rev. **109**, 1492 (1958).

[69] B. L. Altshuler and A. G. Aronov, Solid State Commun. **30**, 115 (1979).

[70] B. L. Altshuler, A. G. Aronov, and P. A. Lee, Phys. Rev. Lett. **44**, 1288 (1980).

[71] B. L. Altshuler, A. G. Aronov, and A. Yu. Zyuzin, Sov. Phys. JETP **59**, 415 (1984).

[72] in *Electron-Electron Interactions in Disordered systems, eds. A L. Efros and M. Pollak (Mod. Problems in Condensed Matter Sciences, Vol. 10), North Holland.*

[73] E. Abrahams, P. W. Anderson, D. C. Licciardello, and T. V. Ramakrishnan, Phys. Rev. Lett. **42**, 673 (1979).

[74] M. E. Gershenzon, V. N. Gubankov, and M. I. Falei, Sov. Phys. JETP **63**, 1287 (1986).

[75] Deuk Soo Pyun and Thomas R. Lemberger, Phys. Rev. Lett. **63**, 2132 (1989).

[76] M. Gijs and Y. Bruynseraede, Solid State Commun. **57**, 141 (1986).

[77] C. Van Hasendonck and Y. Bruynseraede, Phys. Rev. B **33**, 1684 (1986).

[78] V. N. Lutskii, A. S. Rylik, and A. K. Savchenko, JETP Lett. **41**, 163 (1985).

[79] W. Maj, Solid State Commun. **71**, 161 (1989); **74**, 395 (1990).

[80] Y. Imry and Z. Ovadyahu, Phys. Rev. Lett. **49**, 841 (1982).

[81] A. E. White, R. C. Dynes, and J. P. Garno, Phys. Rev. B **31**, 1174 (1985).

[82] S. Schmitz and S. Ewert, Solid State Commun. **74**, 1067 (1990).

[83] S. Schmitz and S. Ewert, Solid State Commun. **79**, 525 (1991).

[84] G. Hertel, D. J. Bishop, E. G. Spencer, J. M. Rowell, and R. C. Dynes, Phys. Rev. Lett. **50**, 743 (1983).

[85] T. Furubayashi, N. Nishida, M. Yamaguchi, K. Morigaki, and H. Ishimoto, Solid State Commun. **58**, 587 (1986).

[86] R. C. Dynes and J. P. Garno, Phys. Rev. Lett. **46**, 137 (1981).

[87] W. L. McMillan, Phys. Rev. B **24**, 2739 (1981).

[88] A. M. Finkelshtein, Sov. Phys. JETP **59**, 212 (1984).

[89] C. Castellani, C. Dicastro, P. A. Lee, and M. Ma, Phys. Rev. B **30**, 527 (1984).

[90] G. Bergmann, Phys. Rev. B **28**, 2914 (1983).

[91] G. Bergmann, Phys. Rep. **107**, 1 (1984).

[92] M. Kaveh and N. F. Mott, J. Phys. C **15**, L697; L707 (1982).

[93] S. Ewert, B. Mellis, S. Schmitz, in *Proceedings of the International Conference on High Temperature Superconductivity and Localization Phenomena*, World Scientific, Singapore, pp. 54 (1992).

[94] D. Pines, *The Many-Body Problem, A Lecture Note and Reprint Volume*, (Addison-Wesley, Reading, Massachusetts, 1994).

[95] G. Grimvall, *The Electron-Phonon Interaction in Metals*, (North-Holland, Amsterdam, 1981).

[96] J. Bardeen, Phys. Rev. Lett. **6**, 57 (1961).

[97] J. G. Adler, H. J. Kreuzer, and W. J. Wattamaniuk, Phys. Rev. Lett. **27**, 185 (1971).

[98] A. D. Brailsford and L. C. Davis, Phys. Rev. B **2**, 1708 (1970).

[99] W. J. Wattamaniuk, H. J. Kreuzer, and J. G. Adler, Phys. Lett. **37A**, 7 (1971).

[100] J. M. Ziman, *Principles of the Theory of Solids*, 2nd Ed. (Cambridge University Press, 1972), Chap. 2.

[101] H. Ibach and H. Lüth, *Festkörperphysik*, (Springer-Verlag, Berlin/Heidelberg, 1981), Kap. 5.

[102] D. J. Scalapino and P. W. Anderson, Phys. Rev. **133**, A921 (1964).

[103] B. N. Brockhouse, T. Arase, G. Caglioti, K. R. Rao, and A. D. B. Woods, Phys. Rev. Lett. **128**, 1099 (1962).

[104] R. Stedman, L. Almqvist, and G. Nilsson, Phys. Rev. **162**, 549 (1967).

[105] I. K. Yanson, Sov. Phys. JETP **33**, 951 (1971).

[106] V. M. Svistunov, M. A. Belogolovskii, O. I. Chernysh, A. I. Khachaturov, and A. P. Kvachev, Zh. Eksp. Teor. Fiz. **84**, 1781 (1983).

[107] H. Hermann and A. Shmid, Z. Phys. **211**, 313 (1968).

[108] J. M. Rowell, W. L. McMillan, and W. L. Feldman, Phys. Rev. **180**, 658 (1969).

[109] F. Burrafato, C. Faraci, G. Giaquinta and N. Mancini, J. Phys. C **5**, 2179 (1972).

[110] O. I. Chernyak, A. I. Khachaturov, and A. P. Kvachev, J. Phys. F **14**, 2359 (1984).

[111] J. A. Appelbaum and W. F. Brinkmann, Phys. Rev. **183**, 553 (1969).

[112] C. R. Leavens, Solid State Commun. **55**, 13 (1985).

[113] D. J. Scalapino, *Superconductivity*, edited by R. D. Parks (Marcel Dekker, New York, 1969), Vol. 1, pp. 449.

[114] J. J. Wnuk, Phys. Status Solidi B **146**, K91 (1988).

[115] J. J. Wnuk, J. Phys. Condens. Matter **6**, 6637 (1994).

[116] L. D. Landau and E. M. Lifshitz, *Quantum Mechanics*, (Addison-Wesley, Reading, Massachusetts, 1958).

[117] Yu. M. Ivanchenko and Yu. V. Medvedev, Zh. Eksp. Teor. Fiz. **64**, 1024 (1973).

[118] M. A. Belogolovskii, Yu. M. Ivanchenko, and Yu. V. Medvedev, Pis. Zh. Eksp. Teor. Fiz. **21**, 701 (1975).

[119] M. A. Belogolovskii, Yu. M. Ivanchenko, and Yu. V. Medvedev, Fiz. Verd. Tela. **17**, 2907 (1975).

[120] Yu. M. Ivanchenko and Yu. V. Medvedev, Fiz. Nizk. Temp. **2**, 141 (1976).

[121] K. Knorr and N. Barth, Solid State Commun. **8**, 1085 (1970).

[122] J. E. Dowman, M. L. A. MacVicar, and J. R. Waldram, Phys. Rev. **186**, 452 (1969).

[123] G. Beuermann, Z. Phys. B **44**, 29 (1981).

[124] I. K. Yanson and A. G. Batrak, JETP Lett. **27**, 197 (1978).

[125] B. L. Blackford and K. Hill, J. Low Temp. Phys. **43**, 25 (1981).

[126] G. I. Lykken, A. L. Geiger, and E. N. Mitchell, Phys. Rev. Lett. **25**, 1578 (1970).

[127] W. Zawadzki, in *Handbook on Semiconductors*, edited by T. S. Moss (North-Holland, Amsterdam, New York, Oxford, 1982), Vol 1, edited by W. Paul, Chap. 12, pp. 713-803.

[128] J. R. Schriefer, *Theory of Superconductivity*, (W. A. Benjamin, New York, 1964).

[129] E. H. Sondheimer, Proc. Phys. Soc. A, **65**, 561 (1952).

[130] H. Rauh, R. Geick, H. Köhler, N. Núcker, and N. Lehner, J. Phys. C **14**, 2705 (1981).

[131] V. Damodara Das and N. Soundararajan, J. Appl. Phys. **65**, 2332 (1989).

[132] B. Roy, B. R. Chakraborty, R. Bhattacharya, and A. K. Dutta, Solid State Commun. **25**, 617 (1978).

[133] M. M. Ibrahim, M. M. Wakkad, E. Kh. Shokr, and H. A. Abd El-Ghani, Appl. Phys. A **52**, 237 (1991).

[134] T. C. Harman, B. Paris, S. E. Miller, H. L. Goering, J. Phys. Chem. Solids **2**, 181 (1957).

[135] J. R. Drabble and C. H. L. Goodman, J. Phys. Chem. Solids **5**, 142 (1958).

[136] J. Horák, Z. Straý, and J. Klikorka, Phys. Status Solidi B **147**, 501 (1988).

[137] J. Horák, K. Cermák, and L. Koudelka, J. Phys. Chem. Solids **47**, 805 (1986).

[138] W. Zawadzki, in *Physics of Narrow Gap Semiconductors. Lecture Notes in Physics*, edited by W. Zawadzki, (Berlin, Heidelberg, New York: Springer, 1982), **152**, pp. 1.

[139] F. Koch, in *Physics of Narrow Gap Semiconductors. Lecture Notes in Physics*, edited by W. Zawadzki, (Berlin, Heidelberg, New York: Springer, 1982), **152**, pp. 92.

[140] T. C. McGill and D. A. Collins, Semicond. Sci. Technol. **8**, S1 (1993).

[141] B. M. Ashkerov, *Electron Transport Phenomena in semiconductors*, (World Scientific, Singapore, 1994), Chap. 1.

[142] W. S. Boyle and G. E. Smith, in *Progress in Semiconductors*, edited by A. F. Gibson (Wiley, New York, 1963), Vol. 7.

[143] M. S. Dresselhaus, J. Phys. Chem. Solids **32**, Suppl. No. 1, 3 (1971).

[144] V. S. Edelman, Adv. Phys. **25**, 555 (1976).

[145] J-P. Isshi, Aust. J. Phys. **32**, 585 (1979).

[146] L. R. Windmiller, Phys. Rev. **149**, 472 (1966).

[147] N. B. Brandt, N. Ya. Minina, and Chu Chen-Kang, Sov Phys. JETP **24**, 73 (1967).

[148] R. S. Blewer, N. H. Zebouni, and C. G. Grenier, Phys. Rev. **174**, 700 (1968).

[149] E. Hatta, T. Gohda, K. Mukasa, and T. Ishii, Vacuum. **46**, 1377(1995).

[150] G. Hass, Anorg. Chem. **254**, 96 (1947).

[151] R. V. Coleman, R. C. Morris, and J. E. Christopher, in *Methods of Experimental Physics*, edited by R. V. Coleman, (Academic, New York, 1974), Vol. 11, Chap. 4.

[152] Barone and G. Paterno, *Physics and Applications of the Josephson Effect*, (Wiley-Interscience, New York, 1982).

[153] R. Stratton, J. Phys. Chem. Solids **23**, 1177 (1962).

[154] S. Basavaiah and J. H. Greiner, J. Appl. Phys. **48**, 4630 (1977).

[155] D. P. Oxley, A. J. Bowles, C. C. Horley, A. J. Langley, R. G. Pritchard, and D. L. Tunnicliffe, Surface and Interface Analysis. **2**, 31 (1980).

[156] B. L. Blackford, Rev. Sci. Instr. **42**, 1198 (1971).

[157] R. J. Jennings and J. R. Merrill, J. Phys. Chem. Solids **33**, 1261 (1972).

[158] R. G. Keil, T P. Graham, and K. P. Roenker, Appl. Spectrosc. **30**, 1 (1976).

[159] I. Giaever, H. R. Hart, and K. Megerle, Phys. Rev. **126**, 941 (1962).

[160] D. E. Thomas and J. M. Rowell, Rev. Sci. Instr. **36**, 1301 (1965).

[161] J. S. Rogers, Rev. Sci. Instr. **41**, 1184 (1970).

[162] J. M. Rowell and L. Kopf, Phys. Rev. **137**, 907 (1965).

[163] W. Zawadzki, Adv. Phys. **23**, 435 (1974).

[164] T. Ando, A. B. Fowler, and F. Stern, Rev. Mod. Phys. **54**, 437 (1982).

[165] E. O. Kane, J. Phys. Chem. Solids **1**, 24 (1957).

[166] W. Zawadzki and P. Pfeffer, Semicond. Sci. Technol. **5**, 179 (1990).

[167] V. Ariel Altschul, A. Fraenkel, E. Finkman, J. Appl. Phys. **71**, 4382 (1992).

[168] R. Stratton, G. Lewicki, C. A. Mead, J. Phys. Chem. Solids **27**, 1599 (1966).

[169] S. L. Kurtin, T. C. McGill, and C. A. Mead, Phys. Rev. B **3**, 3368 (1971).

[170] H. Kroger, IEEE Trans. Electron Devices **ED-27**, 2016 (1980).

[171] J. Horák, L. Tichý, A. Vaśko, M. Frumer, Phys. Status Solidi A **14**, 2891 (1972).

[172] E. Hatta, J. Nagao, and K. Mukasa, Z. Phys. B **98**, 33 (1995).

[173] E. Hatta, J. Nagao, and K. Mukasa, J. Appl. Phys. **79**, 1511 (1996).

[174] W. Pauli, *Pauli Lectures on Physics: Volume 5. Wave Mechanics*, edited by C. P. Enz (MIT Press, Cambridge, MA, 1973), pp. 128.

[175] A. B. Migdal and V. Krainov, *Approximation Methods in Quantum Mechanics*, (W. A. Benjamin, Inc., New York, 1969).

[176] W. Richter, A. Krost, U. Nowak, and E. Anastassakis, Z. Phys. B **49**, 191 (1982).

[177] W. B. Joyce, IEEE J. Quantum Electron. **QE-9**, 1625 (1983).

[178] B. König, Phys. Lett. **39A**, 117 (1972).

[179] H. Flietner, Phys. Status Solidi **54**, 201 (1972).

[180] E. Hatta and K. Mukasa, Solid State Commun. **98**, 293 (1996).

[181] J. J. Hauser and L. R. Testardi, Phys. Rev. Lett. **20**, 12 (1968).

[182] W. A. Harrison, Phys. Rev. **123**, 85 (1961).

[183] J. S. Lannin, L. M. Calleja, and M. Cardona, Phys. Rev. B **12**, 585 (1975).

[184] R. I. Sharp and E. Warming, J. Phys. F **1**, 570 (1971).

[185] J. Salgado, F. Gompf, and W. Reichardt, *German Physical Society Mtg., Freudenstadt, Germany, 1974, and Inst. für Angewandte Kernphysik, Kernforschungszentrum, Karlsruhe, Federal Republic of Germany, Progress Report*, 1974 (unpublished).

[186] V. S. Oskotskii, Sov. Phys. Solid State **9**, 2 (1967).

[187] J. Sosnowski, A. Czochar, and E. Maliszewski, in *Fifth IAEA Symposium on Inelastic Neutron Scattering*, (IAEA, Vienna, 1972), pp. 61.

[188] N. A. Red'ko, M. S. Bresler, and S. S. Shalyt, Sov. Phys. Solid State **11**, 2435 (1970).

[189] L. M. Falicov and P. J. Lin, Phys. Rev. **141**, 562 (1966).

[190] A. Leger and J. Klein, Phys. Letters. **28A**, 751 (1969).

[191] T. T. Chen and J. G. Adler, Solid State Commun. **8**, 1965 (1970).

[192] I. K. Yanson, N. N. Gribov, and O. I. Shklyarevskii, JETP Lett. **42**, 195 (1985).

[193] A. G. M. Jansen, A. P. van Gelder, and P. Wyder, J. Phys. C **13**, 6073 (1980).

[194] A. V. Khotkevich and I. K. Yanson, *Atlas of Point Contact Spectra of Electron-Phonon Interactions in Metals*, (Kluwer Academic Publishers, Dordrecht, 1995).

[195] S. Kunii, J. Magn. Magn. Magn. **63-64**, 673 (1987).

[196] N. F. Mott, *Metal-Insulator Transitions*, 2nd ed. (Taylor and Francis, London, 1990).

[197] P. Przysiupski and J. Raułuszkiewicz, Solid State Commun. **50**, 789 (1984).

[198] B. R. Sood, Phys. Rev. B **25**, 6064 (1982).

[199] J. G. Massey and Mark Lee, Phys. Rev. Lett. **77**, 3399 (1996).

[200] O. I. Barkalov, I. T. Belash, V. F. Gantmakher, and V. M. Teplinskii, Solid State Commun. **75**, 345 (1990).

[201] V. F. Gantmakher, S. E. Éspov, and V. M. Teplinskii, Sov. Phys. JETP **70**, 211 (1990).

[202] A. Götzberger, Z. Phys. **142**, 182 (1955).

[203] E. Cremer and E. Rudel, Z. Phys. **151**, 487 (1958).

[204] E. Hatta and K. Mukasa, Solid State Commun. **103**, 235 (1997).

[205] F. Brinkman, R. C. Dynes, and J. M. Rowell, J. Appl. Phys. **41**, 1915 (1970).

[206] J. S. Moodera and R. Meservey, Phys. Rev B **42**, 179 (1990).

[207] C. Reale, Phys. Lett. **74A**, 438 (1979).

[208] W. Buckel, *Supraleitung*, -4., überarb. u. erg. Aufl. (VCH, Weinheim, 1990).

[209] O. I. Shklyarevskii, I. K. Yanson, and N. N. Gribov, Sov. J. Low. Temp. Phys. **14**, 263 (1988).

[210] R. C. Jaklevic, J. Lambe, M. Mikkor, and W. C. Vassell, Phys. Rev. Lett. **26**, 88 (1971).

[211] R. C. Jaklevic and J. Lambe, Phys. Rev. B **12**, 4146 (1975).

[212] B. A. Tavger and V. Ya. Demikhovskii, Sov. Phys. Uspekhi **11**, 644 (1969).

[213] V. N. Lutskii, D. N. Korneev, and M. I. Elinson, JETP Lett. **4**, 179 (1966).

[214] G. A. Gogadze and I. O. Kulik, Sov. Phys. Solid State **7**, 345 (1965).

[215] A. A. Galkin, V. M. Svistunov, A. I. D'yachenko, and V. Yu. Tarenkov, JETP Lett. **21**, 118 (1975).

[216] K. Fuchs, Proc. Cambridge Philos. Soc. **34**, 100 (1938).

[217] V. M. Svistunov, V. Yu. Tarenkov, and V. T. Vitchinkin, Sov. Phys. Solid State **21**, 1929 (1979).

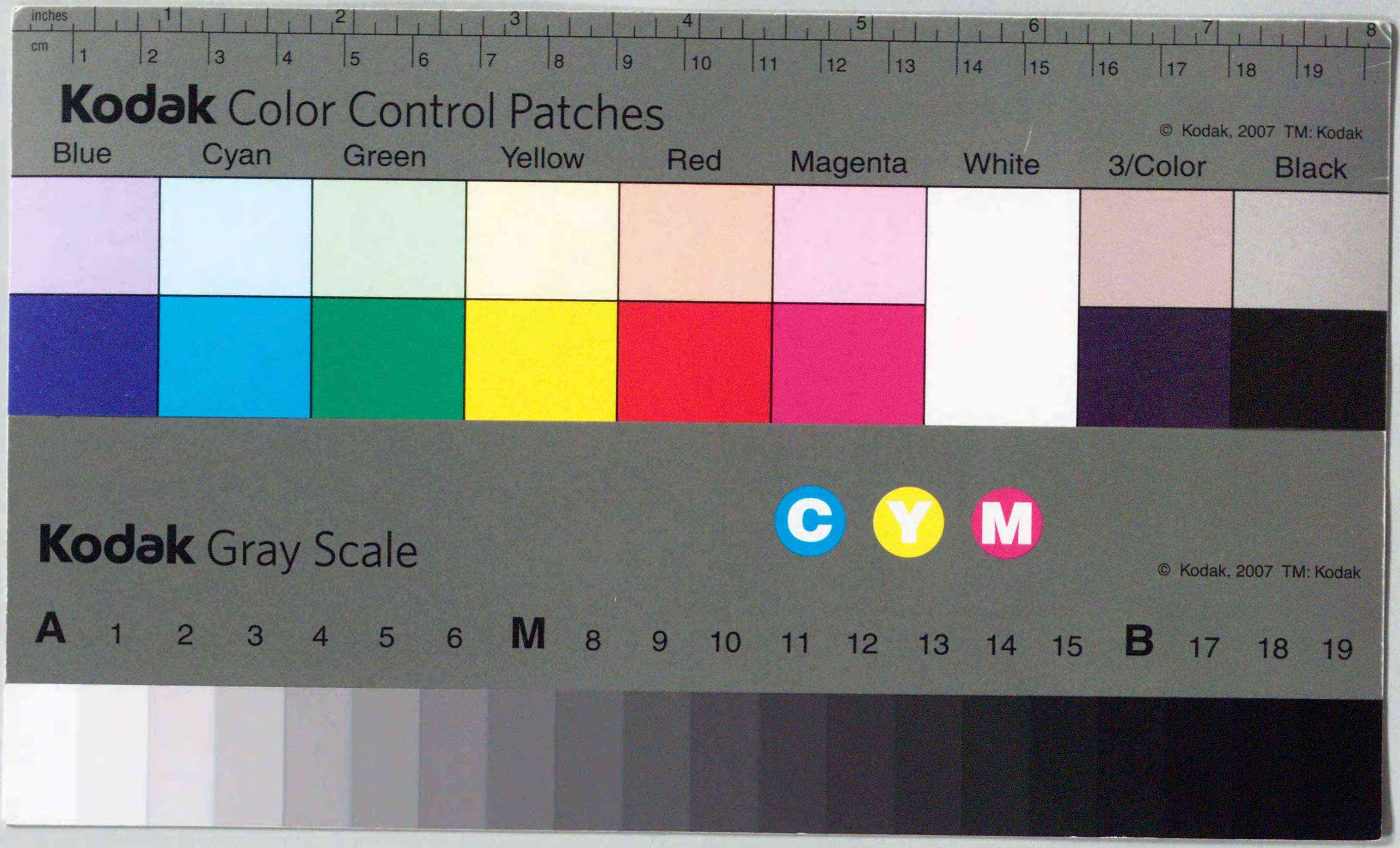
inches 1 2 3 4 5 6 7 8
cm 1 2 3 4 5 6 7 8 9 10 11 12 13 14 15 16 17 18 19
Kodak Color Control Patches
© Kodak, 2007 TM: Kodak
Blue
Cyan
Green
Yellow
Red
Magenta
White
3/Color
Black
C
Y
M
Kodak Gray Scale
© Kodak, 2007 TM: Kodak
A 1 2 3 4 5 6 M 8 9 10 11 12 13 14 15 B 17 18 19